Numerical modelling of coupled adiabatic shear banding and micro-voiding assisted dynamic ductile failure

Hannah Lois Dorothy

▶ To cite this version:

Hannah Lois Dorothy. Numerical modelling of coupled adiabatic shear banding and micro-voiding assisted dynamic ductile failure. Mechanics of materials [physics.class-ph]. Université Paul Sabatier - Toulouse III, 2018. English. NNT : 2018TOU30176 . tel-02307383

HAL Id: tel-02307383
https://theses.hal.science/tel-02307383

Submitted on 7 Oct 2019

THÈSE

En vue de l'obtention du

DOCTORAT DE L'UNIVERSITÉ DE TOULOUSE

Délivré par l'Université Toulouse 3 - Paul Sabatier

Présentée et soutenue par

Hannah Lois DOROTHY

Le 15 octobre 2018

Modélisation numérique de la rupture ductile dynamique par cisaillement adiabatique et micro-endommagement couplés

Numerical modelling of coupled adiabatic shear banding and micro-voiding assisted dynamic ductile failure

---

Ecole doctorale : **MEGEP - Mécanique, Energétique, Génie civil, Procédés**

Spécialité : **Génie mécanique, mécanique des matériaux**

Unité de recherche :
ICA - Institut Clément Ader

Thèse dirigée par
Patrice LONGERE

Jury
Mme Patricia VERLEYSEN, Présidente
M. Sébastien MERCIER, Rapporteur
M. Laurent STAINIER, Rapporteur
M. André DRAGON, Examinateur
M. Xavier SOLDANI, Examinateur
M. Patrice LONGERE, Directeur de thèse

THÈSE

En vue de l'obtention du

DOCTORAT DE L'UNIVERSITÉ DE TOULOUSE

Délivré par l'Université Toulouse 3 - Paul Sabatier

Présentée et soutenue par

Hannah Lois DOROTHY

Le 15 octobre 2018

Modélisation numérique de la rupture ductile dynamique par cisaillement adiabatique et micro-endommagement couplés

Numerical modelling of coupled adiabatic shear banding and micro-voiding assisted dynamic ductile failure

Ecole doctorale : **MEGEP - Mécanique, Energétique, Génie civil, Procédés**

Spécialité : **Génie mécanique, mécanique des matériaux**

Unité de recherche :
ICA - Institut Clément Ader, CNRS UMR 5312

Thèse dirigée par
Patrice LONGERE

JURY

Patricia VERLEYSEN	Professeur, Universiteit Gent	Présidente
Sébastien MERCIER	Professeur, Université de Lorraine	Rapporteur
Laurent STAINIER	Professeur, École Centrale de Nantes	Rapporteur
André DRAGON	Directeur de Recherche Émérite, Institut Pprime	Examinateur
Xavier SOLDANI	Professeur Assistant, Universidad Carlos III	Examinateur
Patrice LONGERE	Professeur, ISAE-SUPAERO	Directeur de thèse

Abstract

High strength metallic materials, notably steel and light-weight titanium and aluminium alloys, are widely used in aeronautical and other structures. In case of accidental overload involving high strain rates and quasi adiabatic conditions, these materials are often susceptible to adiabatic shear banding. The adiabatic shear bands (ASB) are intense shear localisation zones resulting from thermomechanical instability and provoking premature material failure. At an advanced stage of the localisation process, the ASBs have been shown to contain micro-voids (MV) which may coalesce to form cracks and ultimately lead to the fracture of the structure. Thus the coupled mechanisms of ASB+MV act as a precursor to catastrophic failure and it is consequently crucial to numerically model their formation and effects when dealing with structures submitted to high loading rates. The ASBs are also observed in industrial applications such as high speed machining where their formation favours the chip serration.

A large scale postulate is used herein to obtain a global insight into the structural material response. The shear band cluster is indeed contained/ embedded within the representative volume element (RVE), and not the opposite as usually considered. The objective here is to enrich a model describing the ASB effects by taking into account the consequences of the micro-voiding within the progressive failure process. The effects of ASB and MV initiation and evolution on the RVE (material point) response are double: kinematic, namely a progressive deviation of the plastic flow in the band plane described via specific ASB and MV induced velocity gradients; and material, namely a progressive anisotropic degradation of the elastic and plastic moduli described via ASB and MV induced second order tensor deterioration variables. The ASB onset criterion is derived from the linear perturbation analysis and the MV is activated using a critical value for the local energy release rate. The interest of this advanced constitutive model is emphasised by comparison with an application oriented (1-*D*) model where *D* is a scalar damage variable.

The enlarged ASB+MV model is implemented as user material into the engineering finite element (FE) computation code LS-DYNA in the context of standard FE kinematic formulation. The dynamic shear compression loading of a hat shaped structure is simulated; the contributions of the ASB on the one hand and MV on the other hand could be clearly identified and in agreement with experimental results. Moreover, the limitation of the current numerical approaches to simulate the high speed machining is evidenced.

Résumé

Les matériaux à haute résistance, notamment les aciers et les alliages à base d'aluminium et de titane, sont largement utilisés dans l'aéronautique comme matériaux structuraux et de protection. Dans le cas de surcharges accidentelles impliquant des vitesses de chargement élevées et des conditions quasi adiabatiques, ces matériaux sont souvent sensibles au cisaillement adiabatique par bande. Les bandes de cisaillement adiabatique (BCA) sont des zones étroites de cisaillement intense qui résultent d'une instabilité thermomécanique et qui conduisent à une rupture prématurée du matériau. À un stade avancé du processus de localisation, des micro-cavités (MCs) ont été observées dans les BCAs. Ces MCs peuvent coalescer pour former des fissures et mener à la rupture de la structure. Ainsi, les mécanismes couplés d'ASB+MC agissent comme un précurseur à la rupture catastrophique et il est par conséquent important de modéliser numériquement leurs effets dans des structures soumises à des sollicitations à haute vitesse. Les BCAs apparaissent aussi dans certaines applications industrielles, telles que l'usinage à grande vitesse, où elles favorisent le festonnement du copeau.

Un postulat de grande échelle est appliqué ici où la longueur caractéristique du volume élémentaire représentatif (VER) est plus grande que la largeur de bande, et non l'inverse comme fait communément. L'objectif du travail présenté est d'enrichir un modèle décrivant les effets des BCAs en prenant en compte les conséquences de l'endommagement par MC dans le processus progressif de la rupture. Les effets des BCAs et des MCs sur la réponse du VER sont doubles : cinématique, à savoir une déviation progressif de l'écoulement plastique dans le plan de la bande décrite via des gradients de vitesse induits par les BCAs et par les MCs; et matériel, à savoir une dégradation anisotrope des modules élastiques et plastiques décrite via des variables tensorielles d'ordre deux de détérioration induite par les BCAs et par les MCs. L'amorçage des BCAs est déterminé à partir d'une analyse linéaire de stabilité et celui des MCs par une valeur critique du taux de restitution d'énergie local. L'intérêt de ce modèle avancé est démontré par comparaison avec un modèle orienté application du type (1-*D*) où *D* est une variable de détérioration isotrope.

Le modèle enrichi ASB+MC est implémenté comme matériau utilisateur dans le code de calculs commercial par éléments finis LS-DYNA. La simulation du chargement dynamique de cisaillement par compression d'une éprouvette chapeau a été conduite ; les contributions des BCAs d'une part et des MCs d'autre part dans la détérioration de la structure sont clairement identifiées et en accord avec les résultats expérimentaux. De plus, la limitation des approches numériques actuelles pour simuler l'usinage à grande vitesse est mise en évidence.

Acknowledgements

Above all, I thank my Lord Jesus Christ for His saving grace, everlasting mercies and bountiful blessings in my life. I thank Him for bestowing upon me His grace and wisdom, enabling me to successfully complete my PhD.

Firstly, I would like to express my sincere gratitude to my PhD supervisor Prof. Patrice Longère for his diligent guidance, patience, motivation and support throughout the course of the PhD. The regular review meetings and discussions proved extremely helpful in the progress of the research work. I wholeheartedly thank him for the meticulous correction of all the written articles and the present thesis. I am thankful to him for giving me the opportunities to present our research work in several conferences and to teach master's student. I am indeed blessed to have had such an excellent PhD supervisor and a mentor. I would always remain grateful to him.

I thank Dr. Xavier Soldani of Universidad Carlos III for the collaboration on the simulation of high speed machining.

I sincerely thank each of the jury members for having examined this work.

I truly appreciate each of my fellow PhD students at Insitut Clément Ader for providing a warm and friendly environment and for the moments of sharing and fun. I am pleased to thank my former officemate Dr. Johannes Wolf for all his advice and help when I first started my PhD. It was absolutely amazing to share my office with Miguel Ruiz De Sotto, having lots of insightful discussions, fun and small talk. I express my heartfelt thanks to Gunasilan Manar and Norazrina Binti Mat Jali for their company and aid in times of need.

Last but not least, I would like to thank my parents and my sister for their love and support. Words cannot express how grateful I am to my mother, who has always been a pillar of strength, for all her prayers, selfless love and encouragements throughout my PhD and all along.

Scientific Communications

International peer reviewed article

[ACL1] **H.L. Dorothy** and P. Longère. Modelling of high strain rate Adiabatic Shear Banding induced failure: a comparison of two approaches. ***Int. J. Impact Engineering***. 110, 219-227. **2017** doi.org/10.1016/j.ijimpeng.2017.02.024

[ACL2] **H.L. Dorothy**, X. Soldani and P. Longère. Adiabatic Shear Band assisted chip serration in High Speed Machining: Some Modelling Issues. Submitted to ***J. Adv Mat. Process. Tech.***

Journal article without peer-review

[ASCL1] **H.L. Dorothy**, P. Longère and A. Dragon. Coupled ASB-and-microvoiding-assisted Dynamic Ductile Failure. ***Procedia Engineering***. 197, 60-68. **2017** doi.org/10.1016/j.proeng.2017.08.082

[ASCL2] **H.L. Dorothy**, P. Longère and A. Dragon. Modelling of high strain rate failure under ASB and microvoiding. ***Procedia Engineering***. 173, 593-600. **2017** doi.org/10.1016/j.proeng.2016.12.107

National or International conference proceedings

[ACT1] **H.L. Dorothy** and P. Longère. Dynamic failure of viscoplastic materials under ASB and micro-voiding. Accepted in **EPJ web of conference**. ***12th International DYMAT Conference**, 9-14 September* **2018**.

[ACT2] **H.L. Dorothy** and P. Longère. Modélisation isotrope vs. anisotrope du processus de dégradation dynamique par cisaillement adiabatique. Proceedings of *CSMA2017, **13ème Colloque National en Calcul des Structures**, Giens (France), 15-19 mai* **2017**

[ACT3] P. Longère, A. Dragon and **H.L. Dorothy**. Modelling of shear failure caused by adiabatic shear banding and subsequent microvoiding. Proceedings of *ICTAM 2016, **24th International Congress of Theoretical and Applied Mechanics**, Montréal (Canada), 21-26 August* **2016**

International or national conference without proceedings

[COM1] **H.L. Dorothy**, P. Longère and A. Dragon. Description of dynamic shear localization and failure in viscoplastic structures. *ESMC 2018, **The 10th European Solid Mechanics Conference**, Bologna (Italy), 2-6 July* **2018**

[COM2] **H.L. Dorothy** and P. Longère. Description of dynamic shear localization-controlled failure in structural materials. *ECCM 6, **6th European Conference on Computational Mechanics**, Glasgow (UK), 11-15 June* **2018**

[COM3] **H.L. Dorothy**, X. Soldani and P. Longère. Adiabatic shear band induced chip serration in high speed machining. *AMPT2017, **International Conference on Advances in Materials & Processing Technologies**, Chennai (India), 11-14 December* **2017**

[COM4] **H.L. Dorothy**, P. Longère and A. Dragon. Coupled ASB- and microvoiding-assisted dynamic ductile failure. ***23rd DYMAT Technical Meeting**, Dynamic fracture of ductile materials, Trondheim (Norway), 12-14 September* **2017**

[COM5] **H.L. Dorothy** and P. Longère. Modelling of Adiabatic Shear Band and Microvoid induced Material Degradation . *COMPLAS 2017, **XIV International Conference on Computational Plasticity**. Fundamentals and Applications, Barcelona (Spain), 5-7 September* **2017**

[COM6] **H.L. Dorothy** and P. Longère. Numerical modelling of structural degradation under adiabatic shear banding and micro-voiding. *CFRAC2017, **5th International Conference on Computational Modeling of Fracture and Failure of Materials and Structures**, Nantes (France), 14-16 June* **2017**

[COM7] **H.L. Dorothy**, P. Longère, A. Hor and A. Dragon. Modeling of high strain rate failure under ASB and microvoiding. *IMPLAST 2016, **11th International Symposium on Plasticity and Impact Mechanics**, New Delhi (India), 11-14 December* **2016**

[COM8] **H.L. Dorothy**, P. Longère, A. Hor and A. Dragon. Description of ASB-dynamic localisation as a degradation mechanism. *MTDM2016 - **The 10th International Conference on the Mechanics of Time Dependent Materials**, Paris (France), 17-20 May* **2016**

[COM9] P. Longère and **H.L. Dorothy**. Strain localisation described as a damage-like mechanism: (1-D) vs. D type modeling. ***MécaDymat** - Comportement et rupture des matériaux sous sollicitations dynamiques, Strasbourg (France), 30-31 Mars* **2016**

Table of Contents

1 INTRODUCTION

1.1 GENERAL CONTEXT

We are here interested in the response of structures submitted to severe conditions in terms of large deformation, high strain rate and high temperature rise, as notably encountered during accidental events (ship collision, bird/debris strike against aircraft parts, ballistics, etc.) or metal forming (deep drawing, high speed machining, etc.). In the context of the design of engineering structures of large dimensions, the aim is to assess numerically their current and residual resistance. Failure of structures is known to be strongly dependent on a large number of parameters, including but not restricted to amount of strain, strain rate, temperature and loading path, and to result from various mechanisms operating at different scales, viz cleavage vs. microvoiding or shear localization. The present work more specifically focuses on the failure of structures under adiabatic shear banding and further micro-voiding which occurs under high strain rate loading and low stress triaxiality.

In this context, the present study aims at modelling the adiabatic shear banding and the consecutive micro-voiding induced material deterioration. High strength and light-weight materials such as steels, titanium and aluminium alloys are predominantly used as constitutive materials of aeronautical and other structures. Although these alloys exhibit excellent mechanical properties in terms of strength, toughness and weight, they possess a severe weakness in terms of susceptibility to adiabatic shear banding which is a form of shear localization that acts as a precursor to catastrophic failure.

The adiabatic shear bands (ASB) are intense shear localization zones as seen in Fig. 1.1 which are generated in thermo-viscoplastic materials when they are submitted to high strain rate loading. The high strain rate does not allow sufficient time for the heat generated from the plastic work to diffuse away from the deforming zone in the relatively low heat conductivity materials and by that creating a quasi-adiabatic condition. The heat causes thermal softening, and when the thermal softening overcomes the strain/strain rate hardening, conditions are favourable for the localized shear bands to be formed.

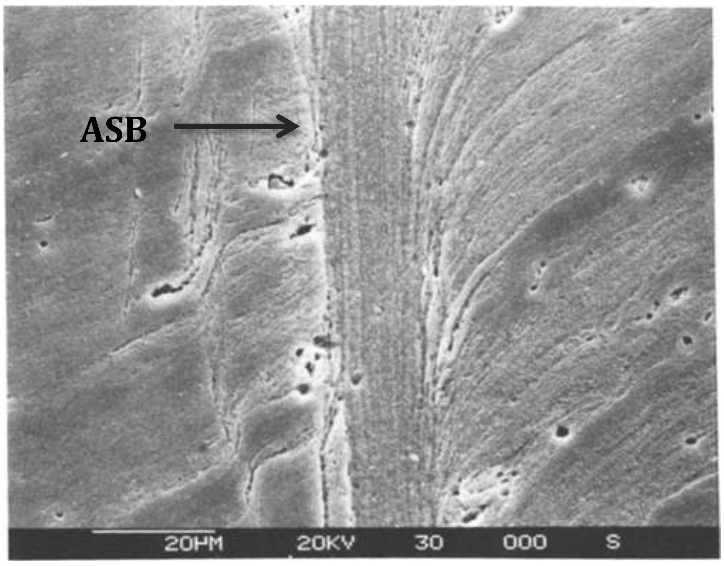

Fig. 1.1 Adiabatic Shear Band seen in 7039 Aluminium alloy. After [1].

The ASB are not only formed in metal alloys but also in glassy polymers. PMMA cuboid specimens subjected to dynamic impact in a split Hopkinson bar also show crossed shear bands as shown in Fig. 1.2 (Courtesy of Binti Mat Jali and Longère).

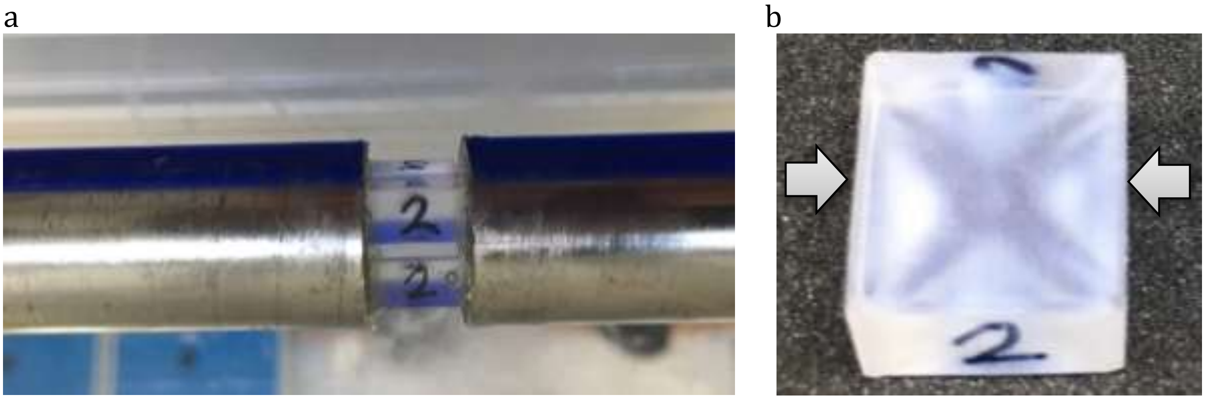

Fig. 1.2 a) High strain rate compression of cuboid polymer specimens in a split Hopkinsor pressure bar setup. b) ASB observed in impacted PMMA polymer material. Courtesy of Binti Mat Jali and Longère (2018).

Once the ASB is formed, the softer material within the band serves as a site for the nucleation and growth of micro-voids (MV) as shown in Fig. 1.3, see Xue et al. [2]. These micro-voids additionally contribute to softening mechanism and accelerate the post-critical drop in strength of the material. The micro-voids coalesce and lead to the formation of cracks which ultimately fracture the material. The consecutive phenomena of shear bands and micro-voids are henceforth termed as ASB+MV.

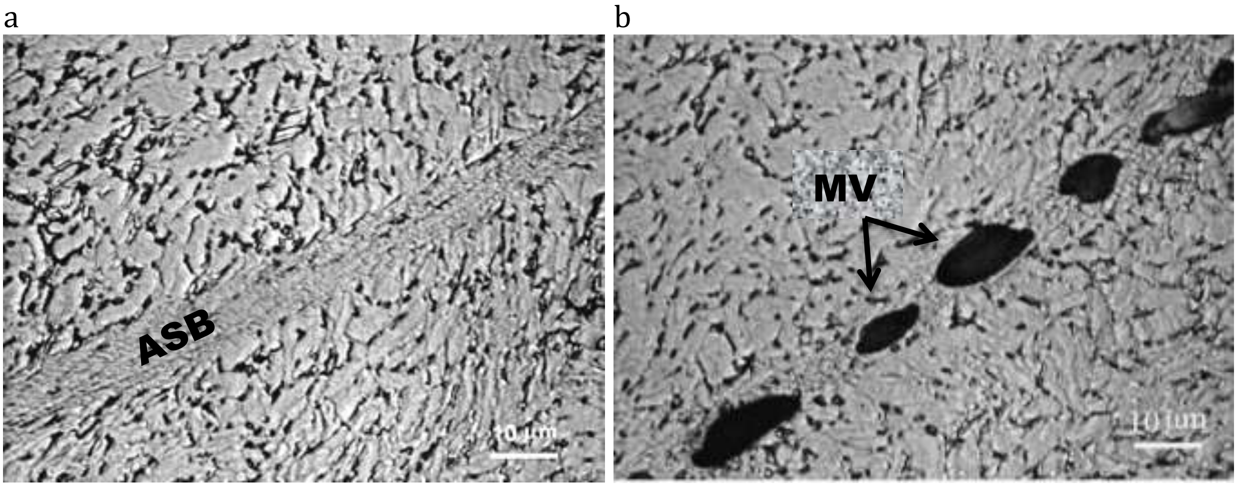

Fig. 1.3 a) Shear bands observed in Ti-6Al-4V alloy. b) Growth of micro-voids within the shear bands. After [2].

The ASB+MV are found to appear in the context of various structural and industrial applications.

The combined action of ASB+MV, on the one hand, is undesirable when it leads to premature failure for example of aircraft structural parts subjected to impact loading. In military applications, the failure of the protective armour plates made of very hard steel under ballistic impacts may also be due to the ASB+MV as shown in Fig. 1.4.

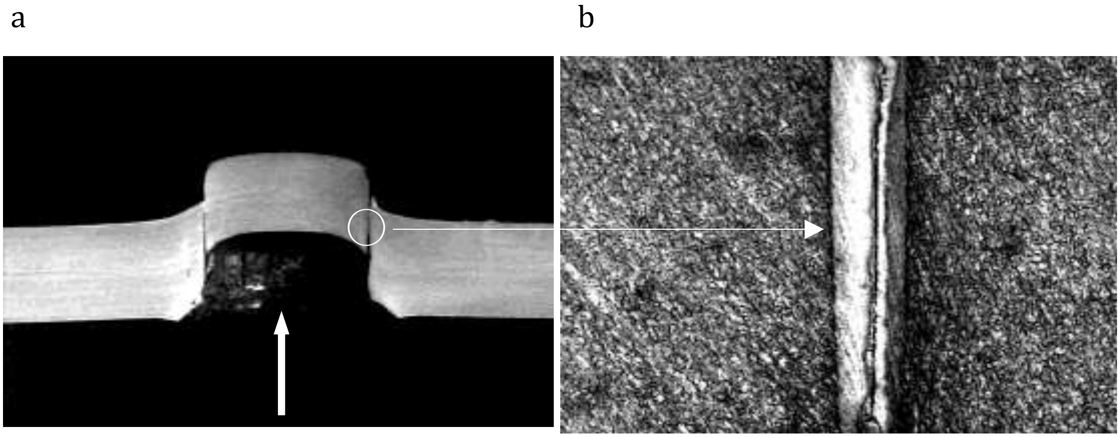

Fig. 1.4 a) Impacted amour steel plate b) Adiabatic shear band containing ultimate crack. After [3].

The US army research laboratory considered the use of titanium alloy instead of steels in the defence structures due to its high strength to weight ratio. The impact tests on Ti-6Al-4V alloy plates using a tungsten fragment simulating projectile (FSP) showed failure by adiabatic shear plugging. Fig. 1.5 shows the deep penetration of the tungsten FSP into the titanium plate, see [4].

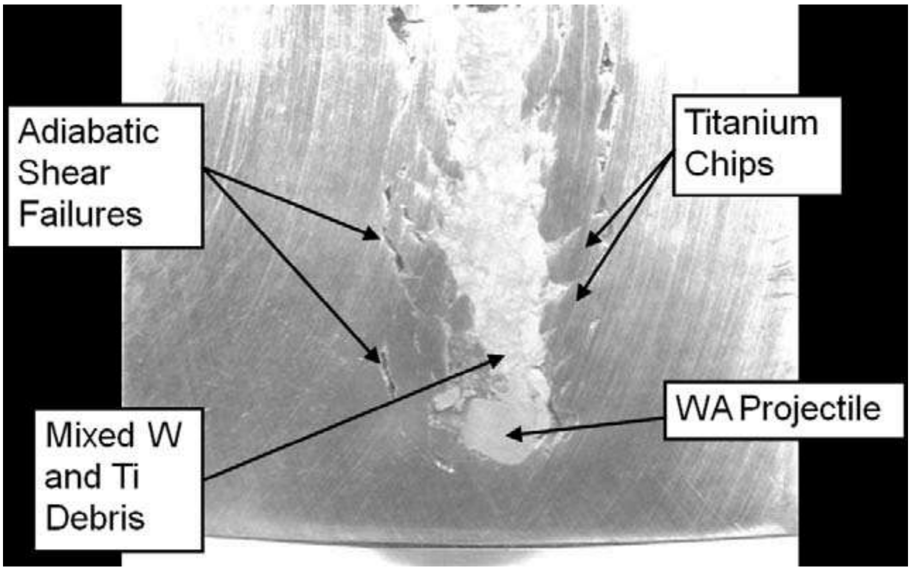

Fig. 1.5 ASB formed in titanium alloy plate allows the deep penetration of tungsten penetrator. After [4].

The ASB+MV are also found to occur in industrial application such as high speed machining (HSM). Contrary to conventional machining, HSM implies high strain rate which triggers the ASBs leading to the formation of serrated chips, see Fig. 1.6. The ASBs appearing on the chip might be a boon in terms of reducing the level of force on the cutting tool and improving chip evacuation [5]. However, the ASBs might also be considered a bane in the high speed cutting process when the serrated chips lead to the fluctuation of the cutting force, decreased tool life, rough surface finish and less accuracy in the machined parts [6].

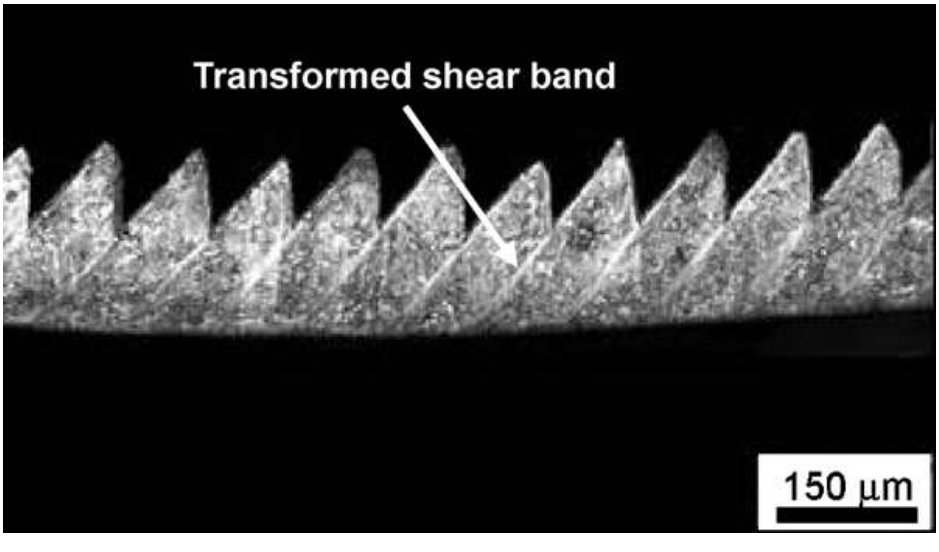

Fig. 1.6 Shear bands causing serrated chips observed in AISI 1045 steel machined at a cutting velocity of 432.6 m/min. After [7].

In either case, it is essential to model the ASB+MV phenomena in the numerical simulation of HSM in order to optimize the process.

On the other hand the ASB+MV prove to be useful in certain military applications such as in a kinetic energy (KE) penetrator. A KE penetrator (Fig. 1.8a) also known as a KE weapon uses kinetic energy to penetrate and destroy the targets (Fig. 1.8b).

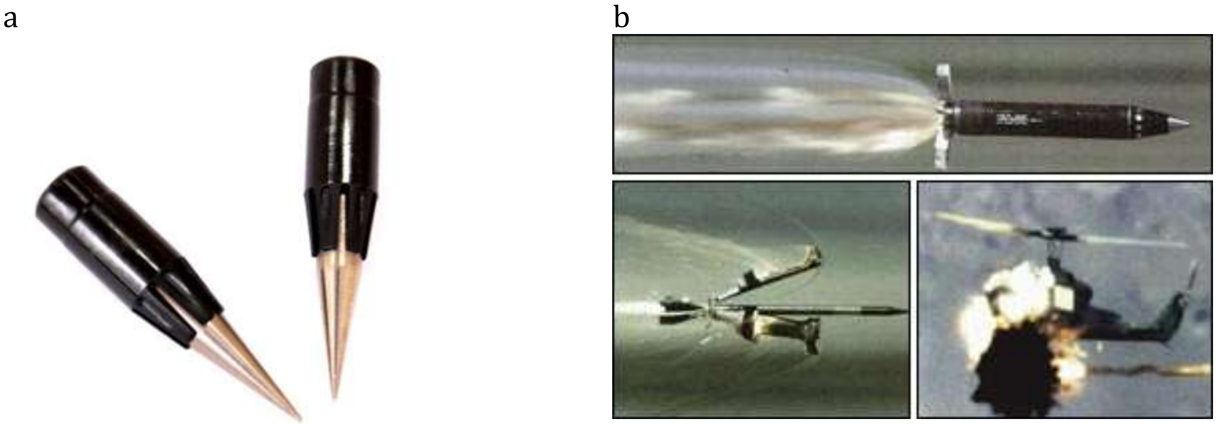

Fig. 1.7 a) Tungsten KE penetrator design. b) Deployment of Kinetic Energy (KE) penetrator to destroy targets. After [8].

In KE penetrators made up of ASB susceptible materials such as depleted uranium alloys, on impact, ASBs appear on the planes of maximum shear and fail, causing the outer penetrator material to exit the zone of interaction with the target. The ASBs thus helps in 'self-sharpening' and thereby improving the ballistic penetration performance of the penetrator, as seen in Fig. 1.8a, refer [9]. If the KE penetrator is made up of a material resistant to ASB such as tungsten alloy, on impact, the tip of the penetrator will be mushroomed by strain hardening and blunted causing less efficient penetration on target as shown in Fig. 1.8b, refer [9],[10].

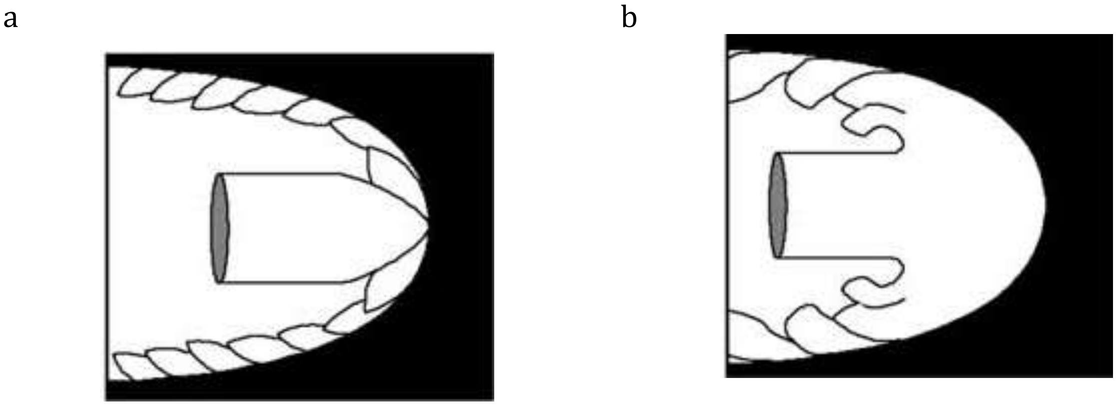

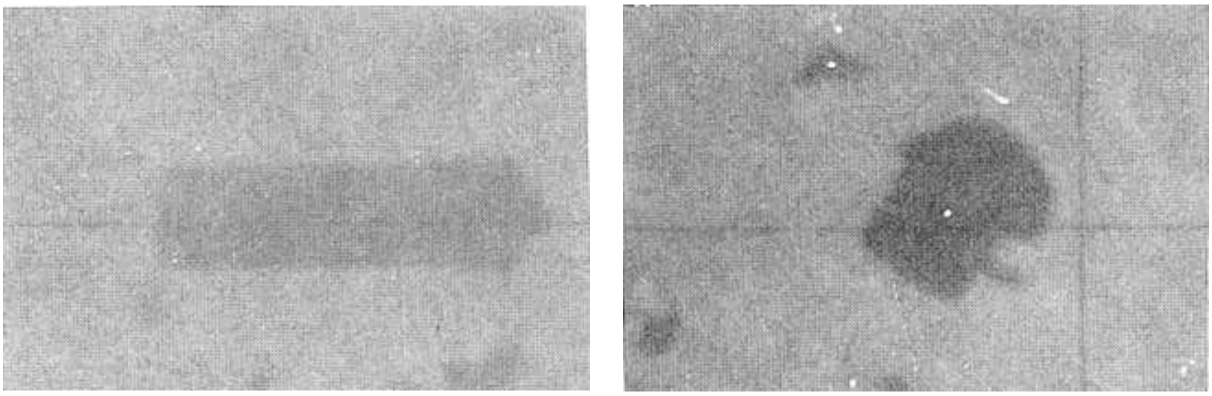

Fig. 1.8 Illustration of penetration cases and radiographic images of residual penetrators after perforating armour steel a) U-3/4Ti alloy penetrator: adiabatic shear failure resulting in chiselled nose. b) Tungsten heavy alloy penetrator: mushroomed head. After [11], [9].

The ASB+MV are thus encountered in numerous applications, and it is therefore indispensable to model the combined phenomenon for the design, optimization or ensuring of structural integrity by prediction of the behaviour of the concerned application.

1.2 CONTEXT OF THE STUDY

The goal here is to represent in a unified model the effects of ASB+MV on the representative volume element (RVE). The two global objectives of the present work can be stated as follows:

1. ***To enrich and improve the embedded-band based constitutive model characterizing ASB induced failure in order to include the effects of micro-voiding in the post-critical regime.***
2. ***Numerically implement the enriched model as user material in a finite element code and evaluate its performance on initial boundary value problems of increasing complexity.***

1.2.1 Experiments

The widely referred experimental work producing ASB is the one performed by Marchand and Duffy [12] in which they produced ASB by subjecting HY-100 steel tube to high strain rate torsion. The average stress and strains and the deformation pattern from the applied grid lines obtained are shown in Fig. 1.9. The stages of deformation distinguished from the inclination of the grid lines in the different frames in Fig. 1.9 a,b are as follows:

(Stage1) Frame 1 : Homogenous strain distribution
(Stage2) By Frame 4 : Weakly heterogeneous deformation
(Stage3) Frame 5 : Strongly heterogeneous deformation when the ASB initiates and propagates and causes a progressive drop in strength.
(Stage4) Frame 6 : Crack appearance within the shear band

This experiment demonstrates the significant consequence in the material of the presence of ASB and the subsequent crack supposedly formed by the coalescence of MVs.

The present work does not involve any experimental campaigns. The results of Marchand and Duffy's experiment are used herein as a reference for numerically calibrating the material constants.

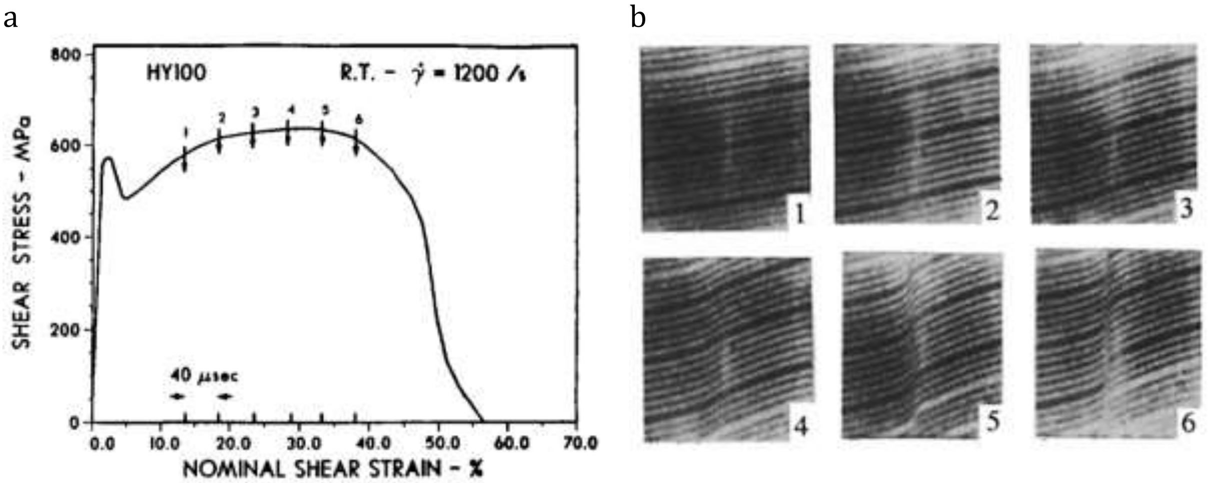

Fig. 1.9 a) Stress-Strain behaviour of HY-100 steel in dynamic shear. b) Photographs of the grid lines showing deformation pattern at instants of the numbered arrows in (a). After [13].

There are various other experiments evidencing that the premature material failure caused by the ASB is preceded by the formation, growth and coalescence of micro-voids. For example, the microscopic observation by Liu et al. [14] in Fig. 1.10 of the crushed Ti-6Al-4V bars showed ASBs containing voids and coalesced voids (cracks).

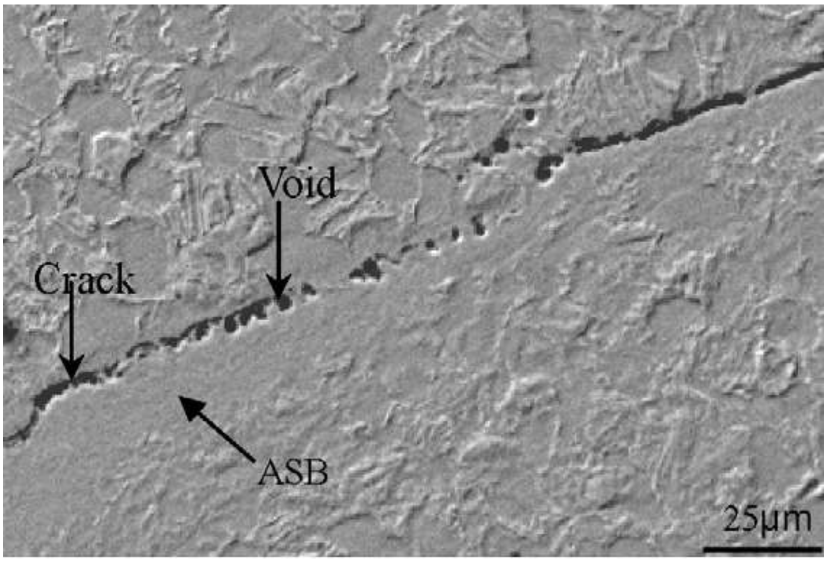

Fig. 1.10 Micro-voids and coalesced voids (cracks) seen in the wake of ASB in Ti-6Al-4V alloy. After [14].

1.2.2 Modelling

A large scale postulate is adopted herein contrary to the many approaches in the literature describing the ASB. In the present approach, the RVE has a length scale greater than the ASB width; in other words, the shear band is embedded within the RVE.

A physics motivated phenomenological constitutive model was initially developed by Longère et al. [3] in an irreversible thermodynamics framework which described the material degradation induced predominantly by the ASB. The aim here is to use an enriched version of the aforementioned model based on the model developed by Longère and Dragon [15] in order to explicitly reproduce the consequences of micro-voiding in the band wake with a view to clearly distinguish in the post-critical regime the respective contributions to the material softening coming from the two mechanisms namely adiabatic shear banding on one hand and micro-voiding on the other hand.

It is important to distinguish the two consecutive mechanisms for the following reasons. The ASB in itself is a weak discontinuity, causing shape change, as there is cohesion of matter within the band, whereas the MV is a strong discontinuity with the absence of matter within, creating irreversible damage in the material and imposing volume change and related hydrostatic components to the induced strain rate because of the void growth. Depending on the loading, the ASB does not necessarily lead to micro-voiding and further failure; and in certain cases, upon unloading, the ASB is quenched by the cooler surrounding material, undergoes phase transformation and finally becomes harder at room temperature than the surrounding matrix material. Therefore considering a unique variable accounting indistinctly for ASB and MV does not allow for distinguishing the zones in the structure where ASB takes place, with potential initial properties recovering after unloading and cooling as explained above, and where irreversible void-growth induced irreversible damage as a precursor to crack formation takes place.

The effects of ASB+MV initiation and evolution on the RVE (material point) response are double: **material**, namely a progressive anisotropic degradation of the elastic and plastic moduli**;** and **kinematic**, namely a progressive deviation of the plastic flow in the band plane. The material effects of ASB and MV are described by anisotropic second order tensor variables. The variables describing the state within the shear bands such as the temperature, strain, strain rate etc. termed as ‘singular’ variables are implicitly embodied within the deterioration variables. The kinematic consequences of ASB and MV are described by supplementary induced inelastic strain rates. As large strains and rotations are involved, objective derivatives are used.

The model also describes the ASB incipience criteria based on a linear perturbation method taking into consideration the role of softening mechanisms namely thermal softening and dynamic recrystallization induced softening. The MV incipience is tentatively treated using a critical value of the local energy release rate.

1.2.3 Numerical simulation

The enriched ASB+MV model is then coded as a user subroutine in Fortran and implemented into the engineering finite element (FE) computation code LS-DYNA. The interest of using this advanced model describing the ASB+MV induced deterioration instead of a simpler engineering oriented model is demonstrated through a comparative study.

For a model to be considered predictive, it has to satisfy a complete Verification and Validation (V&V) procedure. In the V&V procedure, models are tested on initial boundary value problems (IBVP) of increasing complexity against the corresponding experimental results. To begin with, the model is implemented on an RVE scale i.e. on a single FE and the material constants are identified at this scale from the given experiments. Using the constants identified, the model is then implemented on an IBVP with an a priori known path of the ASB+MV. The model’s performance is assessed against experiments and if need be it is recalibrated in a loop with the previous step. The ultimate test of the model’s predictability would be on a complex IBVP where the ASB+MV trajectory is unknown.

In the present work, due to the lack of quantitative experimental results concerning the MV, instead of the V&V, the feasibility and robustness of the enriched model is demonstrated on the RVE and structural scale. The implementation of the model on the complex IBVP namely simulation of high speed machining is a work in progress.

1.3 CHALLENGES

The present study poses various challenges in terms of modelling, numerical simulation and conducting experiments which are categorized below as scientific and industrial challenges.

1.3.1 Scientific challenges

It is required to depict as accurately as possible the physics of ASB+MV phenomenon using an advanced three-dimensional model distinguishing the distinct and consecutive mechanisms of adiabatic shear banding and micro-voiding. The post localization micro-voiding needs to be inserted into the basic model of Longère et al., which describes the coupling between plasticity and strain localization, preferably in a ‘unified approach’ without distorting much its formal structure, rather than developing another constitutive model reproducing the coupling between plasticity and ductile damage. Alternative two-dimensional approaches based on variational methods or finite element kinematics enrichment can be found in Longère [16].

Dealing numerically with the local softening phenomenon, resulting from a competition between material hardening and softening mechanisms and which has severe irreversible consequences at the structural level, would be a challenging task. The model has to prove itself to be robust enough to control the evolution of this material instability all along its progress and accordingly overcome the numerical instability the finite element computation code is subject to in the softening regime and subsequent meshing dependence of the numerical results.

The ultimate challenge lies in demonstrating the developed model to satisfy the V&V procedure and thereby proving it to be predictive. The material constants identification in the V&V procedure consequently creates the need for the availability of experimental results. As the deterioration mechanisms of shear banding and micro-voiding are distinguished in the present study, it is required to identify separately the constants pertaining to each of the specific mechanisms. The difficulty in the experimental work lies in identifying the instant of MV incipience during the high strain rate tests.

Numerically implementing the model on the complex IBVP of high speed machining in the software LS-DYNA comes with its own set of challenges. It is first required to be able to successfully simulate the machining process using a conventional model after having defined proper boundary and contact conditions. Then the advanced model needs to be implemented overcoming the numerical instability and it has to be able to accurately reproduce the morphology of the chip as examined from experimental results.

1.3.2 Industrial challenges

As stated previously, ASB+MV appear in various industrial and military applications as a boon or a bane.

Titanium is extensively being researched for use in the military platforms for its high ballistic performance when used as an armour and its light-weight to increase mobility or to meet tactical requirements. For example, in Fig. 1.11, by replacing the conventional materials with titanium in the four shown areas on the US military tank, over 1500lbs of combat weight was reduced without the loss of function or protection. The use of titanium as a standalone armour material poses the disadvantage of ASB induced failure.

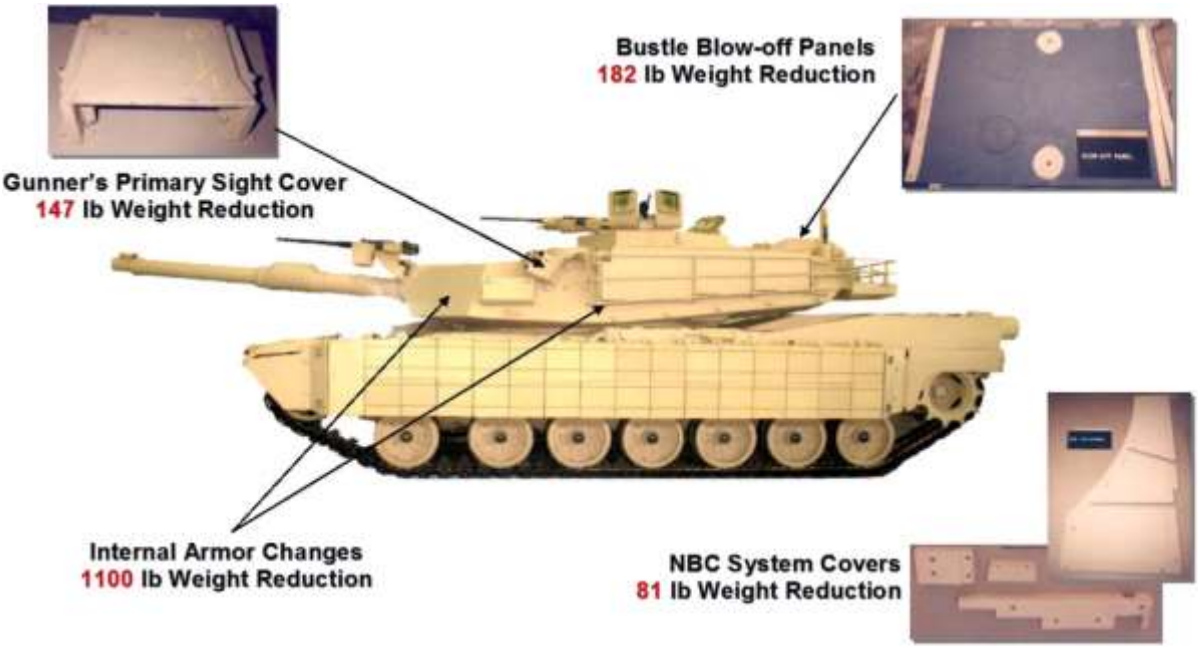

Fig. 1.11 Titanium weight reduction program for US army battle tank. After [4].

On the other hand, it is desirable to manufacture KE penetrators with materials which fail under shear localization to improve the ballistic penetration. Depleted uranium produces toxic, radioactive dust and debris when it burns through targets and in the interest of post conflict management, the United Nations has passed a resolution banning the manufacture of DU weapons. Therefore, research has to be conducted to replace DU with other materials for efficient KE penetrators.

The study of ASB+MV is essential in the context of high speed machining. HSM experiments at varying cutting velocities in metal alloys susceptible to ASB+MV needs to be carried out to study the effect of ASB+MV on the process so as to obtain the desired accuracy in machining, surface finish and tool life. In order to optimize the HSM process, it is in turn imperative to numerically model the ASB+MV phenomena.

In all the above applications, there is a requisite for accurate numerical simulation of the ASB+MV process, which in turn requires a user defined, physics motivated constitutive model describing initiation and consequences of ASB and MV in the material. From an engineering point of view, the developed model should be feasible to implement on the scale of actual large structures.

In the process of implementing the model on numerical simulation, the industry is also required to carry out experimental campaigns for the purpose of material characterization. An ultimate failure criterion needs to be defined which may vary with each engineering application on which the model is implemented and would also depend on the level of conservativeness imposed on the design. For instance, the presence of ASB may be acceptable whereas the appearance of MV may not be desirable.

The developed ASB+MV model is therefore required to be highly reliable and predictive to ensure the integrity of the structures and to augment the performances of weapons and industrial processes.

1.4 ORGANISATION

The chapters are organized in the following manner. Chapter 2 details the physical and mechanical aspects of ASB and MV, the development of the constitutive model and the numerical feasibility and the qualitative analysis of the model on an RVE scale. Chapter 3 presents the numerical implementation of the model on initial boundary value problems. Firstly, the motivation for using the current advanced model describing the ASB induced material deterioration is demonstrated by a comparative study. Then the numerical implementation of the enlarged ASB+MV model on a HSS is assessed followed by the motivations to implement the model on a complex IBVP viz. high speed machining. The conclusions are drawn in Chapter 4 and the prospective work is suggested.

1.5 REFERENCES

[1] P. W. Leech, "Observations of Adiabatic Shear Band Formation in 7039 Aluminum Alloy," *October*, vol. 16A, no. October, pp. 1900–1903, 1985.

[2] Q. Xue, M. A. Meyers, and V. F. Nesterenko, "Self-organization of shear bands in titanium and Ti-6Al-4V alloy," *Acta Mater.*, vol. 50, no. 3, pp. 575–596, 2002.

[3] P. Longère, A. Dragon, H. Trumel, T. De Resseguier, X. Deprince, and E. Petitpas, "Modelling adiabatic shear banding via damage mechanics approach," *Arch. Mech.*, vol. 55, no. 1, pp. 3–38, 2003.

[4] W. A. Gooch, "The Design and Application of Titanium Alloys to U . S . Army Platforms -2010," *TITANIUM 2010 nternational Titanium Association*, no. October. 2010.

[5] A. Molinari, C. Musquar, and G. Sutter, "Adiabatic shear banding in high speed machining of Ti – 6Al – 4V : experiments and modeling," *Int. J. Plast.*, vol. 18, pp. 443–459, 2002.

[6] S. L. Cai and L. H. Dai, "Suppression of repeated adiabatic shear banding by dynamic large strain extrusion machining," *J. Mech. Phys. Solids*, vol. 73, pp. 84–102, 2014.

[7] C. Z. Duan and L. C. Zhang, "Adiabatic shear banding in AISI 1045 steel during high speed machining: Mechanisms of microstructural evolution," *Mater. Sci. Eng. A*, vol. 532, pp. 111–119, 2012.

[8] "Tungsten Alloy Military." [Online]. Available: http://directory-tungsten.blogspot.com/2012/08/tungsten-kinetic-energy-penetrator.html.

[9] L. S. Magness Jr., "High strain rate deformation behaviors of kinetic energy penetrator materials during ballistic impact," *Mech. Mater.*, vol. 17, pp. 147–156, 1994.

[10] J. Liu, L. Shukui, Z. Xiaoqing, Z. Zhaohui, Z. Haiyun, and W. Yingchun, "Adiabatic shear banding in a tungsten heavy alloy processed by hot-hydrostatic extrusion and hot torsion," *Scr. Mater.*, vol. 59, no. 12, pp. 1271–1274, 2008.

[11] W. S. Andrews, "Depleted Uranium on the battlefield," *Can. Mil. J.*, pp. 41–46, 2003.

[12] A. Marchand and J. Duffy, "An experimental study of the formation process of adiabatic shear bands in a structural steel," *J. Mech. Phys. Solids*, vol. 36, no. 3, pp. 251–283, 1988.

[13] K. Cho, S. Lee, S. R. Nutt, and J. Duffy, “Adiabatic Shear Band Formation during Dynamic Torsional Deformation of an HY-100 Steel,” *Acta Metall. Mater.*, vol. 41, no. 3, pp. 923–932, 1993.

[14] X. Liu, C. Tan, J. Zhang, Y. Hu, H. Ma, F. Wang and H. Cai , “Influence of microstructure and strain rate on adiabatic shearing behavior in Ti-6Al-4V alloys,” *Mater. Sci. Eng. A*, vol. 501, no. 1–2, pp. 30–36, 2009.

[15] P. Longere and A. Dragon, “Enlarged finite strain modelling incorporating adiabatic shear banding and post-localization microvoiding as shear failure mechanisms,” *Int. J. Damage Mech.*, pp. 1–28, 2016.

[16] P. Longère, “Adiabatic shear banding assisted dynamic failure: Some modeling issues,” *Mech. Mater.*, vol. 116, pp. 49–66, 2018.

2 THE PHYSICS MOTIVATED APPROACH

ABSTRACT

Adiabatic shear banding (ASB) is a dynamic localization phenomenon resulting from thermomechanical instability under high strain rate involving quasi adiabatic conditions and low stress triaxiality loading conditions. High strength steels and lightweight alloys of titanium and aluminium are highly susceptible to this phenomenon which leads to premature material failure. At an advanced stage of the localization process, the adiabatic shear bands have been shown to contain micro-voids which coalesce to form cracks and ultimately lead to the fracture of the structure. A physics-motivated, three dimensional unified constitutive model accounting for the coupled effects of ASB and micro-voiding has been developed in the context of large deformation, high strain rate and high temperature rise. The influence of the softening mechanisms such as thermal softening and DRX induced softening on the ASB onset is also considered here. The enlarged model is herein implemented as user material into the engineering finite element (FE) computation code LS-DYNA in the context of standard FE kinematic formulation and its performances are assessed.

CONTENTS

2.1 INTRODUCTION

Adiabatic shear banding is a distinct deformation mechanism which occurs in viscoplastic solids during high strain rate and impact loading acting as a precursor to failure such as plugging failure, ductile fracture, explosive failure, etc., see [1],[2],[3]. The Adiabatic Shear Bands (ASB) are seen typically in high strength metals and alloys such as steels and titanium and aluminium alloys (as well as in some glassy polymers) which are often used as component materials for aircraft and other structures. The ASBs are undesirable when they cause catastrophic failures of structures such as protection plates for ballistic applications [4] involving military or civil threats (missile, bird strike, etc). On the other hand, they are desirable in military application such as kinetic energy penetrators in which the formation of ASBs on the side ends of the penetrator helps in a self-sharpening-like mechanism ([5],[6],[7]). They also find application in high speed machining in which they have mitigated effect in the sense that they help to reduce the cutting force but at the expense of cutting force oscillation and rougher surface finish [8],[9]. In the context of engineering design, it is thus crucial to be able to numerically reproduce the consequences of this phenomenon.

The ASBs are narrow regions of intense plastic shear deformation and strength softening resulting from thermo-mechanical instability induced by a competition between hardening and softening mechanisms in the regions of low stress triaxiality during high strain rate loading. The mechanisms causing the softening which triggers the ASB formation are mostly plastic dissipation-induced temperature rise and possibly dynamic recrystallization (DRX) in certain materials. The ASBs appear, for example, in AA7075 aluminium alloy cylinders under compression loading (Fig. 2.1a) when loaded at a strain rate of 2500/s in the form of an ‘X’ in the cross section of the specimen (Fig. 2.1b) (Courtesy Manar and Longère). The shear bands are distinctly oriented causing local degradation of the material properties and a form of induced anisotropy at the scale of the specimen.

As stated by Bai and Dodd [10], a metal alloy exhibiting excellent mechanical properties in terms of strength, toughness and weight may possess a severe weakness in terms of its susceptibility to the adiabatic shear banding. The latter is a complex mechanism requiring a careful consideration of the variables playing a role in the formation and propagation of the shear bands. The consequence of the presence of ASB is shown, for example, in the experiment performed by Marchand and Duffy [11]. A thin-walled tubular steel specimen (Fig. 2.2 a) was subjected to high strain rate torsion by means of torsional Kolsky bar. The deformation pattern (Fig. 2.2 b), the average stress and strain (Fig. 2.2 c) were inferred. By combining (Fig. 2.2 b) and (Fig. 2.2 c), three stages of deformation were distinguished: the 1st stage showed homogenous strain distribution, the 2nd stage is a weakly heterogeneous deformation and the 3rd stage is a strongly heterogeneous deformation when the ASB initiates and propagates and causes a progressive drop in strength of the material leading to premature structural failure.

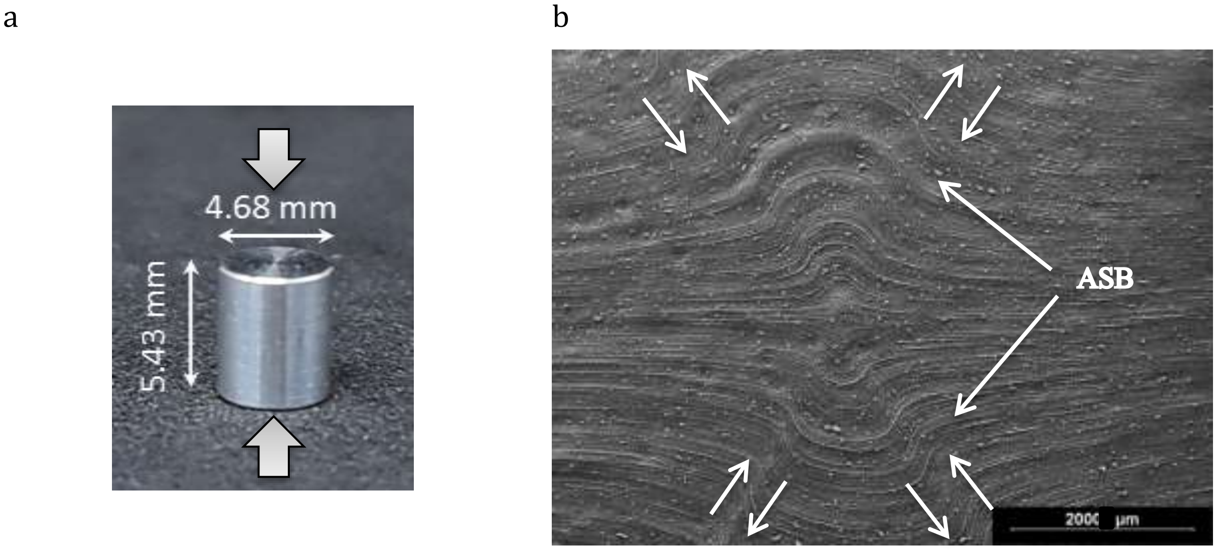

Fig. 2.1 AA7175 aluminium alloy a) Undeformed cylindrical specimen b) Cross-section of the specimen after high strain rate compression loading under microscope showing ASB. Courtesy of Manar and Longère (2018).

In the literature, many approaches describing the ASB degradation have been proposed at a scale lower than the bandwidth implying the use of a very fine meshing, where the mesh size is smaller than the band width, during finite element analysis; see e.g. Peirs et al. [12], Bonnet-Lebouvier et al. [13]and Teng et al. [14]. Yet, knowing that the ASB width is of the order of some tens or hundreds of micrometers, such an approach is not suitable for structures of large dimensions (an aircraft and even a part of an aircraft) requiring coarse meshing, and on the other hand the material within the band is generally different from the one outside as the former may have undergone significant transformations even though material in the band remains in a solid state. With the aim of reproducing the ASB-induced failure in large structures, Longère et al. [15] developed a three-dimensional phenomenological model in a large scale postulate approach in which the representative volume element (RVE) has a length scale greater than the width of the ASB amounting to a global insight into the material response, see Fig. 2.3. The effects of ASB initiation and evolution on the RVE (material point) response are double: kinematic, namely a progressive deviation of the plastic flow in the band plane, and material, namely a progressive anisotropic degradation of the elastic and plastic moduli. The performances of the ASB-model have been assessed considering the dynamic shearing of a hat-shaped structure, see [16] then a ballistic problem, see [4]. Large scale approaches based on variational methods and enriched finite elements can be found in [17] and [18],[19] and a review of ASB-oriented modelling approaches in [20].

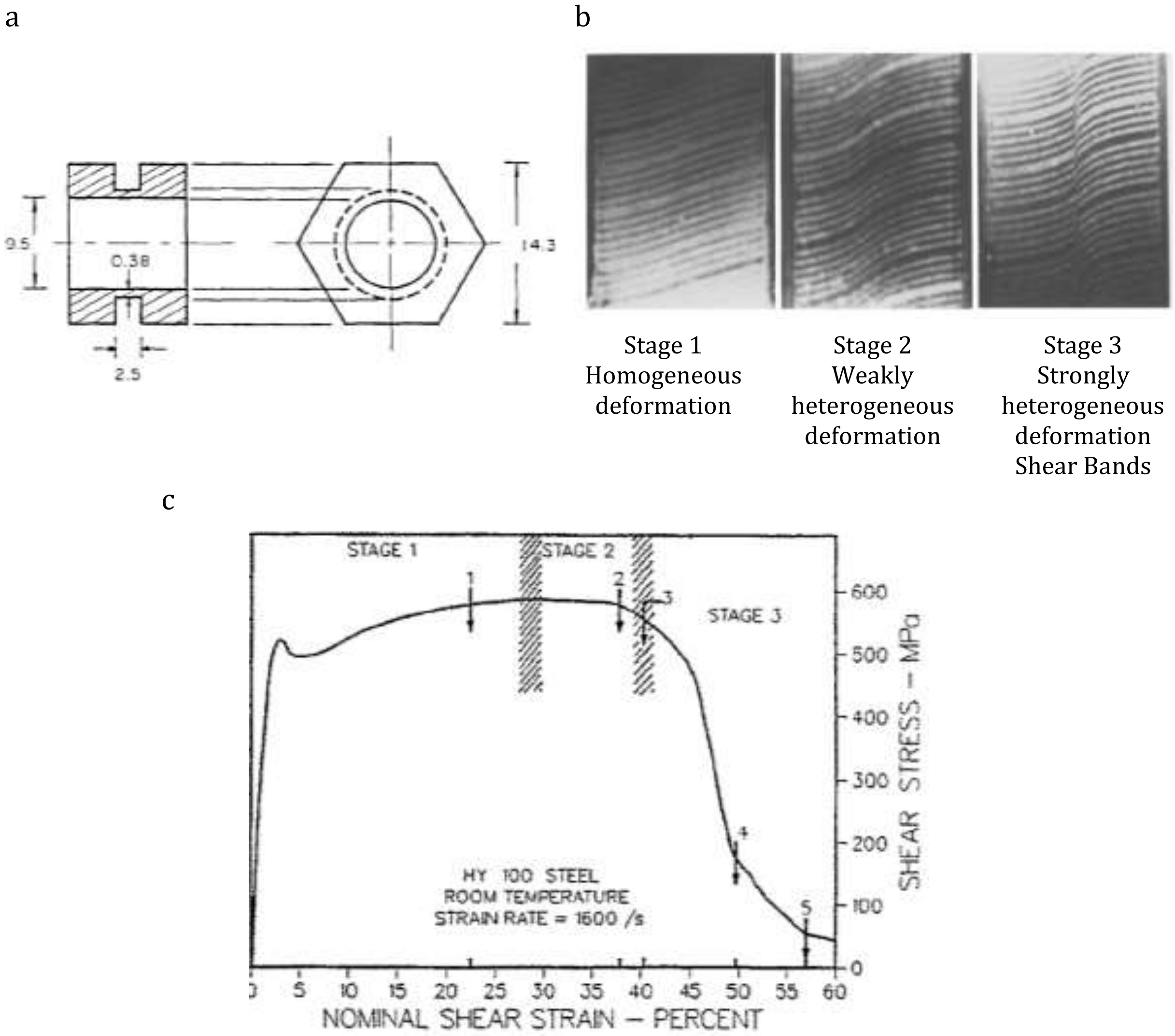

Stage 1
Homogeneous
deformation

Stage 2
Weakly
heterogeneous
deformation

Stage 3
Strongly
heterogeneous
deformation
Shear Bands

Fig. 2.2 After [11] a) Torsional specimen b) Deformation stages observed by means of grid lines c) Shear stress-shear strain curve obtained during experiment.

Once the ASB is formed, the softer material within the band serves as a site for the nucleation and growth of micro-voids. These micro-voids additionally contribute to softening mechanism and accelerate the post-localization drop in strength of the RVE in the large scale postulate framework. The micro-voids coalesce and lead to the formation of cracks which ultimately fracture the material. The evidence of the presence of micro-voids within the ASB was shown by various experimental observations ([21],[2],[22]).

Longère and Dragon [23] , for example, carried out experiments on shear compression specimens (SCS) (see Fig. 2.4a) dimensioned to allow for generating a local shear loading under a global compression loading. The observation of the fractured surface of the SCS (see Fig. 2.4 b, c) showed elongated dimples as the result of micro-voiding in the wake of the ASB. It is clearly seen that the fracture occurred due to two successive mechanisms: adiabatic shear banding and then micro-voiding.

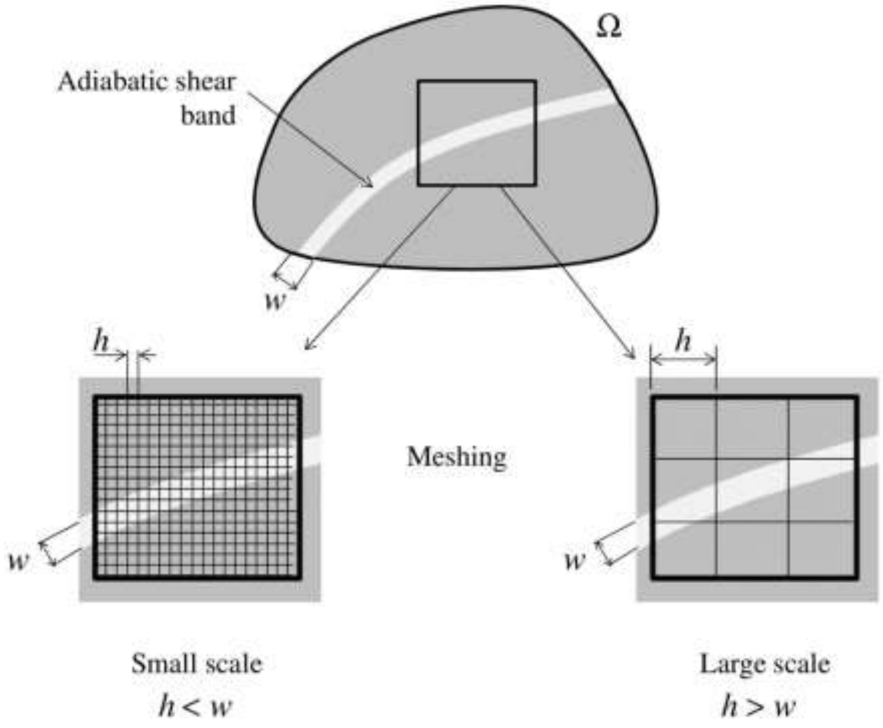

Fig. 2.3 Scale postulate concept. After [20]. Up: Body crossed by a shear band. Bottom left: small scale postulate: the RVE length scale *h* is lower than the bandwidth *w*. Bottom right: large scale postulate: the RVE length scale *h* is greater than the bandwidth *w*.

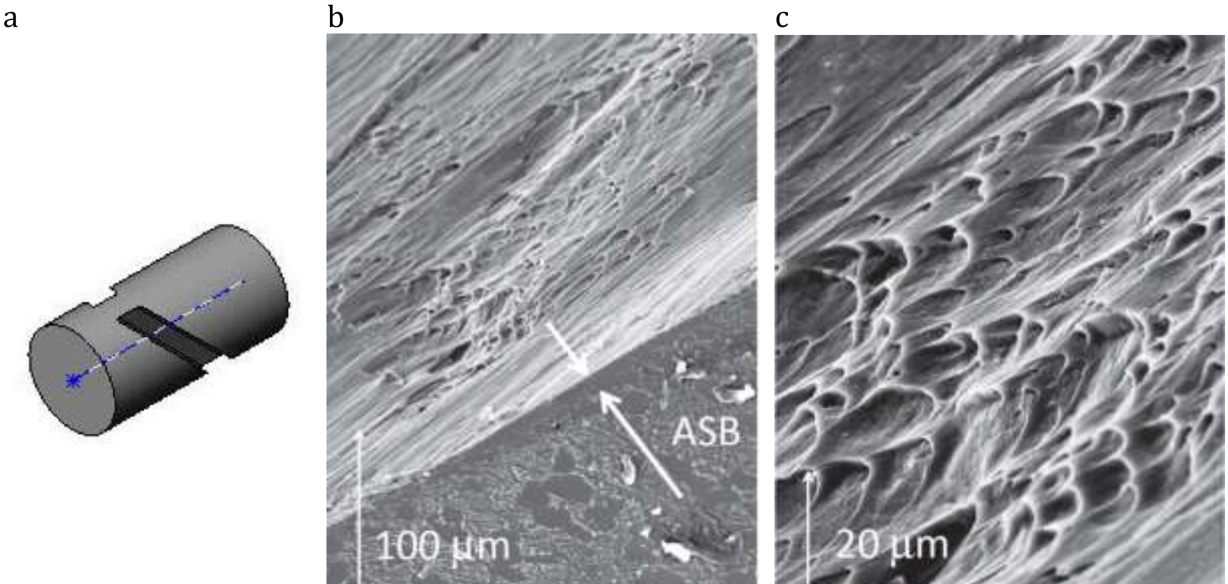

Fig. 2.4 After [23] (a) Shear compression specimen; Microscopic observation of fractured surface (b) 3D view showing ASB; (c) Detailed 3D view showing elongated dimples in the band plane

The constitutive model developed by Longère et al. [15] reproduced the material degradation induced predominantly by the ASB. The aim here is to enrich the aforementioned ASB-model in the post-localization regime in order to reproduce explicitly the consequences of micro-voiding (MV) in the band wake and thereby to be able to clearly distinguish in the post-critical regime the respective contributions to the material softening coming from the two mechanisms namely adiabatic shear banding on one hand and micro-voiding on the other hand. Indeed the ASB does not necessarily lead to micro-voiding and further failure, and in this case, when unloaded, the ASB-containing material may recover properties close to its initial ones. On the other hand, considering a unique variable accounting indistinctly for ASB and MV does not allow for distinguishing the zones in the structure where ASB takes place, with potential initial properties recovering after unloading and cooling as explained above, and where irreversible void-growth induced damage as a precursor to crack formation takes place.

An initial enriched model including MV is proposed in [24]. The original enlarged (ASB+MV)-model is revisited herein, see also [25], and modified in order to represent some operating physical mechanisms. The modified model is then implemented as user material into the engineering finite element (FE) computation code LS-DYNA in the context of standard FE kinematic formulation. The numerical feasibility on a simple finite element and a parametric study of the model are conducted here.

In Section 2.2, the physics and the mechanical aspects of the phenomena of adiabatic shear banding and micro-voiding and their consequences are discussed. A general framework of modelling these mechanisms is also laid out. The more specific constitutive model is detailed in Section 2.3 along with deterioration incipience criteria in Section 2.4. The numerical issues encountered in the finite element implementation and performance of enriched ASB+MV model by numerical implementation on RVE scale are shown in Section 2.5. Finally the conclusions are drawn in Section 2.6.

2.2 PHYSICAL AND MECHANICAL ASPECTS

Considering the various stages leading up to the rupture, the materials accommodate the deformation in different ways. Some possible deformation accommodation paths are illustrated in Fig. 2.5. A material exhibits elasticity during initial loading after which it may either pass into elasto-plasticity or directly into damage stage leading to rupture depending on whether it is ductile or brittle. For ductile materials, further loading may lead either to diffused damage or localised elasto-plasticity. The diffused damage and the localised elasto-plasticity bring about the ultimate rupture of the material.

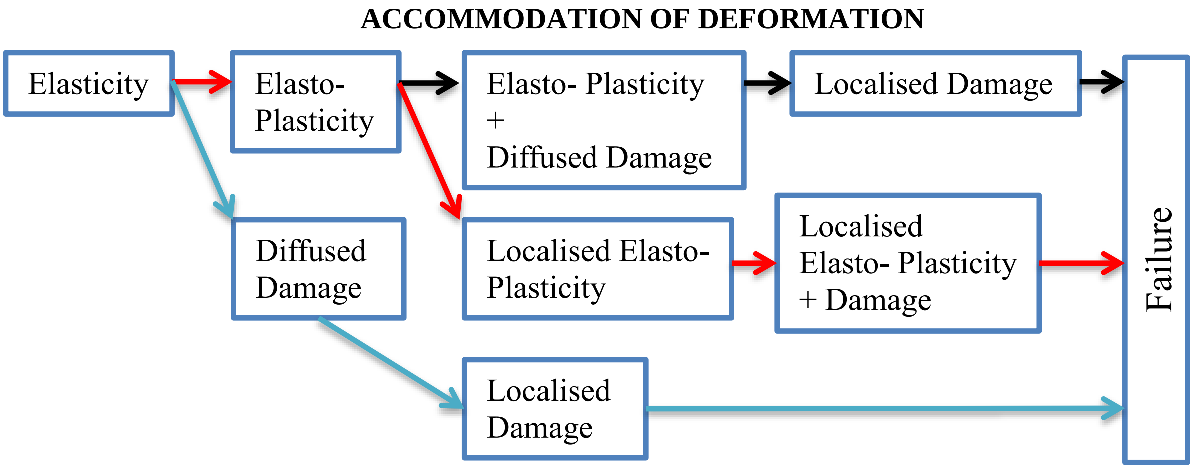

Fig. 2.5 Typical ways for a material to accommodate the deformation

Standard ductile materials follow the black arrow path as shown in Fig. 2.5 in which the diffused and localised damage is preceded by elasto-plasticity. Geomaterials (concrete, ceramics, etc) for example, generally follow the blue arrow deformation path. When loaded well below the glass transition temperature T_g, polymers show also a (quasi) brittle behaviour. When loaded around T_g, the polymers exhibit a viscoelastic behaviour. The formation of ASB takes place following the steps of the red arrows. The high strength metals and alloys under high strain rate loading first exhibit elasto-plasticity. During this stage, the self-heating caused by plastic dissipation and/or softening due to dynamic recrystallization lead to the formation of a localized shear deformation (ASB) which causes material strength deterioration and alters the kinematics of the plastic flow. Further, damage is encountered within the shear bands causing the material failure.

The scenario for ASB- and MV-assisted failure (path following red arrow in Fig. 2.5) is depicted in Fig. 2.6. The regular mechanism of polycrystalline plasticity is in action during the initial stage of hardening. Then the formation of the ASB reduces the material strength. The drop in the material strength in the post critical stage is potentially accelerated by the formation of micro-voids in the wake of the ASB. The micro-voids coalesce and ultimately rupture the material.

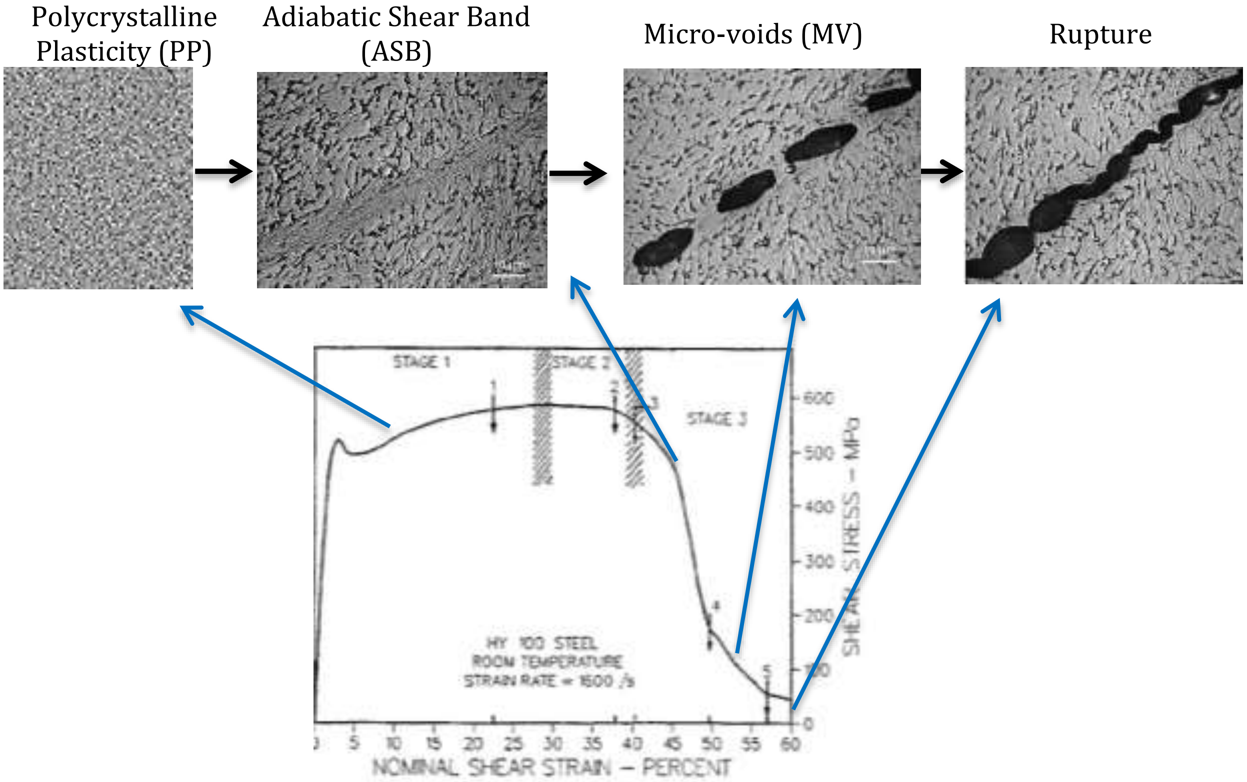

Fig. 2.6 After [11],[2]. Successive mechanisms acting during ASB induced deterioration.

In the following subsections, the salient physical and mechanical features involved are presented.

2.2.1 Physical considerations

The physical features and the formation process of the adiabatic shear bands and micro-voids are presented in this section.

2.2.1.1 Adiabatic shear banding

As mentioned above, the ASBs are distinctly oriented shear localizations resulting from a thermo-mechanical instability phenomenon. The heat produced from the plastic deformation during high strain rate loading, when not having enough time to be conducted away leads to local increase in temperature giving rise to a ‘quasi-adiabatic’ condition. This causes a local thermal softening of the material. Thermo-mechanical instability comes into play as a competition arises between the thermal softening and strain or/and strain-rate hardening. When the rate of this thermal softening surpasses the strain/strain rate hardening, the material deformation becomes unstable and concentrates in narrow softened bands which are termed as ASBs. This widely accepted mechanism of ASB inception and growth was first proposed by Zener and Hollomon [26].

In some cases, for example in steel, the ASBs exhibit phase transformation due to high temperature within the band (>1200K) and appear as distinct white bands after being quenched once unloaded as seen in Fig. 2.7. The shear band width usually ranges between 10-100μm as stated in [10].

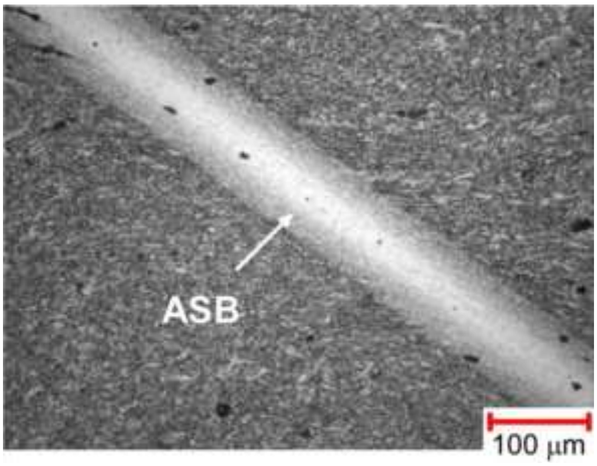

Fig. 2.7 Evidence of phase transformed ASB in steel. After [22].

2.2.1.2 Micro-voiding in the ASB wake

Although the ASBs occur in conditions of negative or nil stress triaxiality, micro-voids have been observed to form and grow within the bands. The micro-voiding could be initiated in the band wake by the hydrostatic tension when there is a change in the loading path. Or as stated in [20], when the loading is interrupted after the formation of the ASB, the quenching of the hot band by the surrounding bulk material may lead to phase transformation involving possible volume increase (as for martensitic transformation) and strain incompatibility-induced crack formation at the band/matrix interface. However, the ASB induced failure is generally observed under monotonic loading. For example, a thick wall cylinder implosion technique was carried out by Xue et al. [2] to produce shear bands on Ti-6Al-4V alloys. The microscopic observation of the ASB showed spherical void nucleation (Fig. 2.8a). The spherical voids were later seen to elongate to ellipse shape rotate along the direction of the shear momentum (Fig. 2.8b). Impact tests on hat shaped specimen by Peirs et al. [1] showed micro-cracks in the wake of the ASB oriented along the highly deformed grains which is different from the ASB orientation Fig. 2.8c.

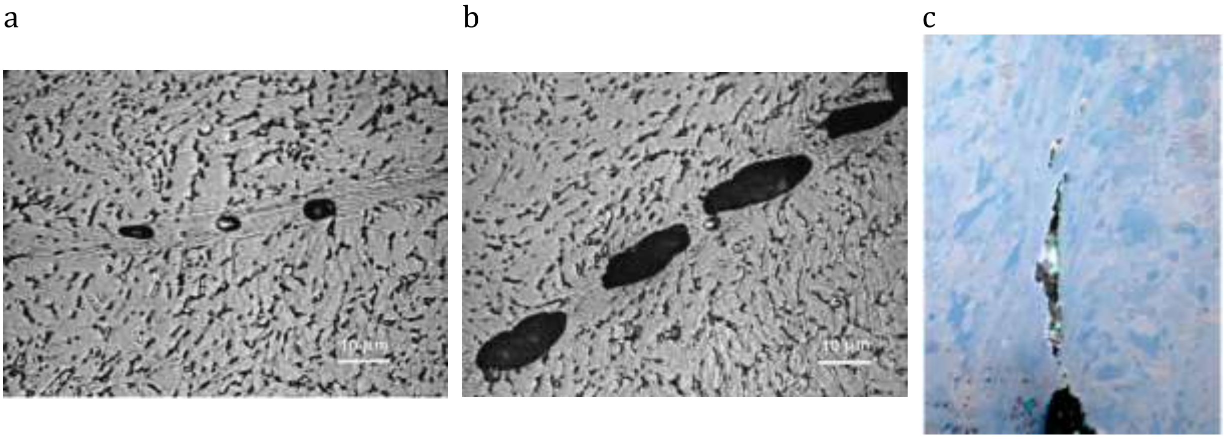

Fig. 2.8 Microscopic observation of ASB showing a) Spherical void nucleation. b) Elongated micro-voids at a later stage. After [2]. c) Micro-cracks observed within the ASB. After [1]

Various perspectives on the stress triaxiality condition for the formation of micro-voids have been proposed which is discussed in section 2.5.1.4. Under a global shear pressure loading, Longère et al. [27] demonstrated that micro-voids can initiate and grow around inclusions in the material. Another theory cited by Odeshi et al. [22] is that the opening of the voids could be because of the high singular temperatures within the ASB causing atomic mobility or creating a lower flow stress in the ASB than the surrounding regular material thereby generating a local tensile stress.

2.2.1.3 Ultimate rupture

The ASB by itself is not a failure mode i.e. a strong discontinuity but it acts as a precursor to premature material failure. It can be seen clearly in the Kalthoff -Winkler (KW) impact test performed by Roux et al. [28] on armour steel that the ASB serves as a path for the crack propagation as shown in Fig. 2.9.

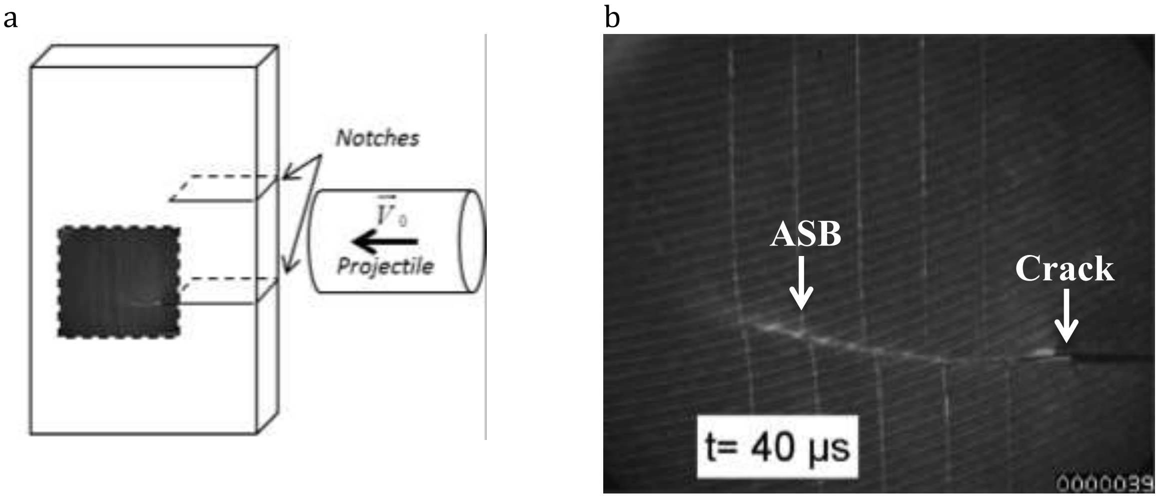

Fig. 2.9 After [28]. a) KW-type impact test configuration. b) Observation of ASB as a precursor to crack.

The micro-voids which germinate within the ASB coalesce to the formation of cracks leading to the ultimate rupture of the material. Liu et al. [29] performed dynamic compression on Ti6Al4V alloy cylinders leading to ASB induced failure. The microscopic observation of the crushed specimens showed ASBs containing voids and coalesced voids (cracks) as shown in Fig. 2.10a. Likewise the observation of the fractures surface of Rittel-Lee-Ravichandran-type shear compression specimens (SCS-RLR) by Longère and Dragon [23], showed the evidence of micro-voids in the ASB wake, see Fig. 2.10b.

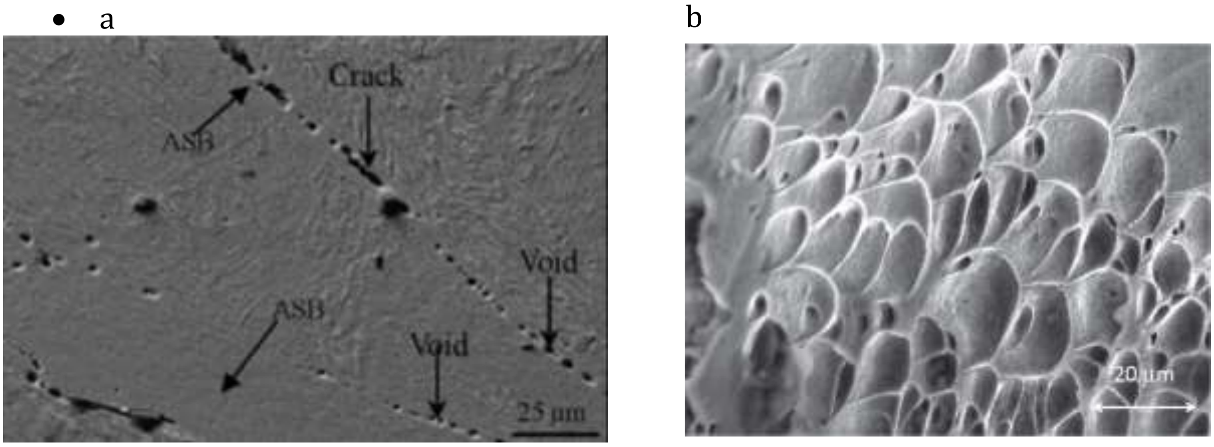

Fig. 2.10 Micro-voids observed in the ASB wake after dynamic compression loading on a) Ti6Al4V cylinders (After [29]) b) SCS-RLR (After [23])

2.2.2 Mechanical consequences

While modelling of ASB can be widely found in the literature, the subsequent mechanism of micro-voiding and its modelling as a distinct contribution to the failure process is largely overlooked. The present work aims to model in a unified approach the ASB and subsequent MV induced degradation.

2.2.2.1 Preliminaries

According to the large scale postulate, see Fig. 2.3 and Fig. 2.11, the shear band or the shear band cluster is considered as an entity embedded within the RVE. The vector $\mathbf{g}$ is collinear to the slip direction in the band plane and $\mathbf{n}$ represents the normal to the band plane. Accordingly, the structural tensors used in the following are defined in (2.1) where $()^{S}$ represents the symmetric and $()^{AS}$ the skew-symmetric parts of the tensor. According to experimental evidences, the ASBs develop along the planes of maximum shear stress within the RVE and thus their orientations are calculated.

$$\begin{aligned}\mathbf{N} &= \mathbf{n}\otimes\mathbf{n}\\ \mathbf{M} &= (\mathbf{g}\otimes\mathbf{n})^{S}\\ \mathbf{T} &= (\mathbf{g}\otimes\mathbf{n})^{AS}\end{aligned} \tag{2.1}$$

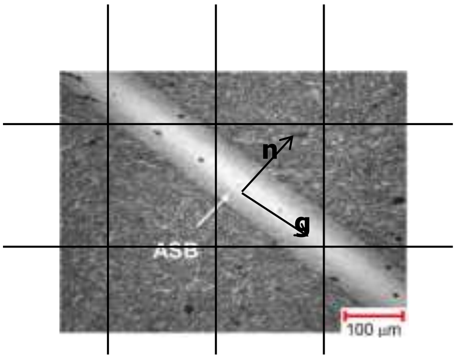

Fig. 2.11 ASB orientation vectors

2.2.2.2 Adiabatic shear banding

ASBs are not a type of crack or a conventional 'damage' as there is cohesion of matter within the bands and without any surface separation. Neither are they slip bands which occur under quasi static conditions as the physics of the phenomenon is different. What is observed is a large gradient of the shear strain between the matrix and the band. It is considered here as a 'degradation' mechanism as it degrades the mechanical properties of the overall material/structure in which it is present.

ASBs are therefore classified as 'weak' discontinuity which involves a discontinuity of the gradient of the displacement/velocity i.e. of the strain/strain rate field. A 'strong' discontinuity such as a crack on the other hand involves a discontinuity of the displacement/velocity field. The concept of discontinuity is illustrated in Fig. 2.12.

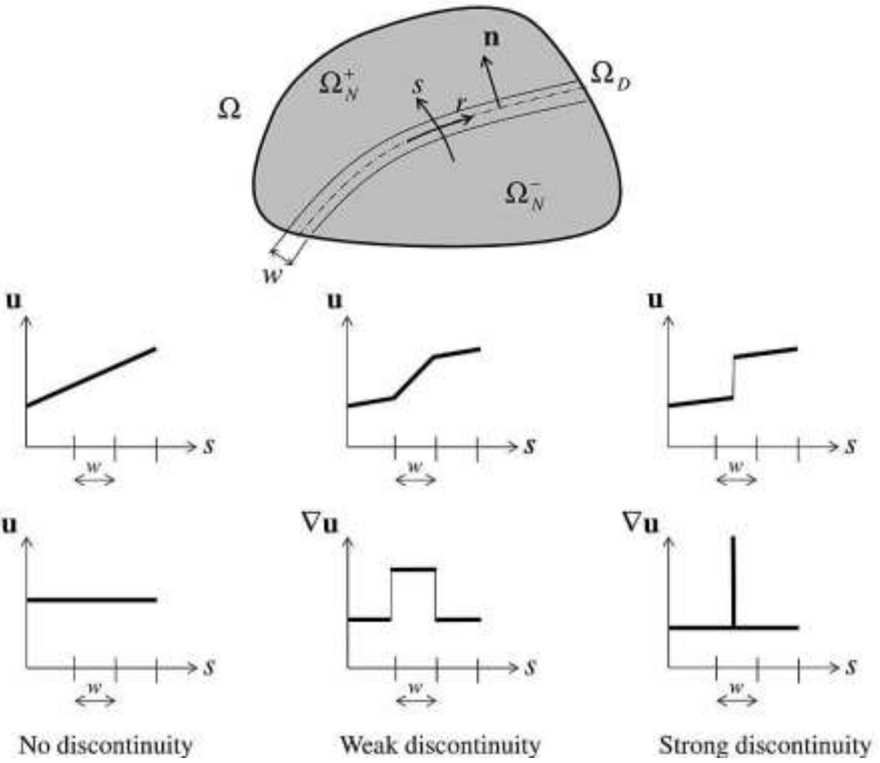

Fig. 2.12 Displacement and strain fields in different cases of discontinuity. After [20]

- Material consequences

As the shear band is strongly oriented in space, it anisotropically degrades the elastic and plastic material properties of the RVE containing the band based on its orientation. The degradation induced by the ASB may therefore be defined by a 2nd order tensor variable $\mathbf{D}$ defined in (2.2). The components of $\mathbf{D}$ are: the scalar degradation intensity denoted by $\mathcal{D}$ and the orientation tensor $\mathbf{N}$ of the ASB.

$$D_{ij} = \mathcal{D}\, N_{ij} \tag{2.2}$$

Consider the illustration in Fig. 2.13, the normal to the ASB is in direction 2, in which case, the deterioration tensor is calculated below:

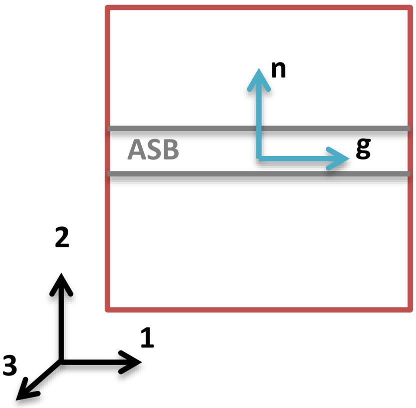

Fig. 2.13 Illustration ASB orientation normal to the 2 direction.

$$\mathbf{n}=\begin{pmatrix}0\\1\\0\end{pmatrix}\rightarrow\mathbf{N}=\begin{bmatrix}0&0&0\\&1&0\\sym&&0\end{bmatrix}\rightarrow\mathbf{D}=\mathcal{D}\begin{bmatrix}0&0&0\\&1&0\\sym&&0\end{bmatrix}\tag{2.3}$$

According to Fig. 2.13, the RVE can be viewed as a 3-layer material or sandwich material with 1 thin soft layer inserted between 2 thick hard layers, inducing a form of orthotropy. The resulting elastic shear modulus μ_{12} and elastic axial (Young's) modulus E_{22} are accordingly expected to progressively vanish while the other elastic moduli are not or less affected.

$$\begin{cases}\tau_{12}=2\mu_{12}\left(\mathcal{D}_{ASB}\right)e^e_{12}\\ \tau_{22}=E_{22}\left(\mathcal{D}_{ASB}\right)e^e_{22}\end{cases}\text{with}\begin{cases}\underset{\mathcal{D}_{ASB}\to\mathcal{D}_{ASBc}}{\mu_{12}\left(\mathcal{D}_{ASB}\right)\to\mu_c}\ll\mu_0\\ \underset{\mathcal{D}_{ASB}\to\mathcal{D}_{ASBc}}{E_{22}\left(\mathcal{D}_{ASB}\right)\to E_c}\ll E_0\end{cases}\rightarrow\begin{cases}\underset{\mathcal{D}_{ASB}\to\mathcal{D}_{ASBc}}{\tau_{12}\left(\mathcal{D}_{ASB}\right)\to\tau_{12c}}\\ \underset{\mathcal{D}_{ASB}\to\mathcal{D}_{ASBc}}{\tau_{22}\left(\mathcal{D}_{ASB}\right)\to\tau_{22c}}\end{cases}\tag{2.4}$$

where $\boldsymbol{\tau}$ is the elastic Kirchhoff stress tensor, $\left(\mu_0,E_0\right)$ and $\left(\mu_c,E_c\right)$ are the initial and critical, elastic shear and axial (Young's) moduli. Note that $\left(\mu_c,E_c\right)$ have non zero values since ASB preserves matter cohesion. If we want to make an analogy with the (1-D)-approach [30], D evolving between 0 (sound) and 1 (failed), we should have

$$\begin{cases}\mu_{12}\left(\mathcal{D}_{ASB}\right)=\left(1-\bar{b}\mathcal{D}_{ASB}\right)\mu_0\\ E_{22}\left(\mathcal{D}_{ASB}\right)=\left(1-\bar{a}\mathcal{D}_{ASB}\right)E_0\end{cases}\tag{2.5}$$

with $\mathcal{D}_{ASB}$ being authorized to have (i) different instantaneous effects on μ_{12} and E_{22} through the constants $\left(\bar{a},\bar{b}\right)$ and (ii) a critical value lower than 1.

- Kinematic consequences

The kinematic consequences of the presence of the shear band are viewed as those of a 'macro-dislocation' considering an RVE as illustrated in Fig. 2.14.

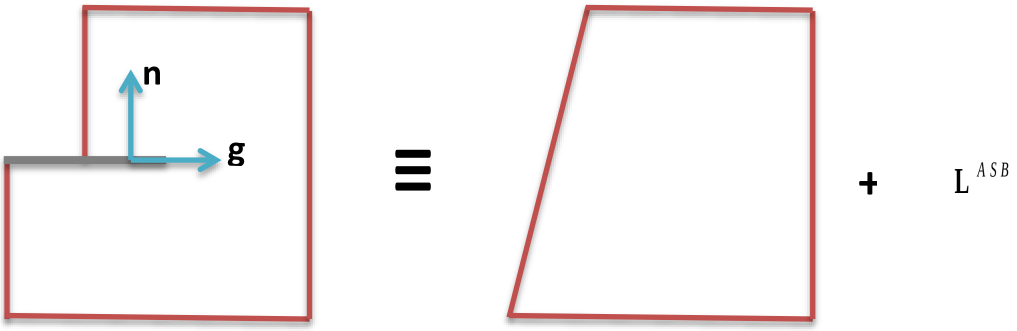

Fig. 2.14 ASB viewed as a super dislocation and the equivalent RVE with kinematic consequences.

The velocity gradient created by the regular plastic deformation outside the band is designated as $\mathbf{L}^{p}$. The ASB induces a supplementary velocity gradient $\mathbf{L}^{ASB}$ as a result of glide velocity $\dot{\gamma}^{ASB}$ in the direction of the unit vector $\mathbf{g}$.

$$\begin{aligned} &\mathbf{L}^{in} = \mathbf{L}^{p} + \mathbf{L}^{ASB} \\ &\mathbf{L}^{ASB} \propto \dot{\gamma}^{ASB}\mathbf{g}\otimes\mathbf{n} \end{aligned} \tag{2.6}$$

The deterioration-induced velocity gradient $\mathbf{L}^{ASB}$ for a given band pattern α is partitioned into symmetric and skew-symmetric parts leading to the corresponding strain rate $\mathbf{d}^{ASB}$ and spin $\boldsymbol{\omega}^{ASB}$ respectively as given below.

$$L_{ij}^{ASB} \propto \sum_{\alpha} \dot{\gamma}^{ASB,\alpha} g_i^{\alpha} n_j^{\alpha} \quad ; \quad \begin{cases} d_{ij}^{ASB} \propto \sum_{\alpha} \dot{\gamma}^{ASB,\alpha} M_{ij}^{\alpha} \\ \omega_{ij}^{ASB} \propto \sum_{\alpha} \dot{\gamma}^{ASB,\alpha} T_{ij}^{\alpha} \end{cases} \tag{2.7}$$

The introduction of $\mathbf{L}^{ASB}$ facilitates the smoothening of the boundary discontinuity caused by ASB as it is done in crystalline plasticity, see Fig. 2.14. The kinematic consequence of the presence of ASB is thus shown by the total inelastic strain rate $\mathbf{d}^{in}$ resulting from the superposition of regular plastic strain rate $\mathbf{d}^{in(PP)}$ by the singular strain rate induced by ASB $\mathbf{d}^{in(ASB)}$.

$$d_{ij}^{in} = d_{ij}^{in(PP)} + d_{ij}^{in(ASB)} \tag{2.8}$$

Table 2.1 Summary of kinematic and material consequences of ASB

Kinematic consequence	Material consequence
$L_{ij}^{ASB} \propto \sum_{\alpha} \dot{\gamma}^{ASB,\alpha} g_i^{\alpha} n_j^{\alpha} \quad ; \quad \begin{cases} d_{ij}^{ASB} \propto \sum_{\alpha} \dot{\gamma}^{ASB,\alpha} M_{ij}^{\alpha} \\ \omega_{ij}^{ASB} \propto \sum_{\alpha} \dot{\gamma}^{ASB,\alpha} T_{ij}^{\alpha} \end{cases}$ $d_{ij}^{in} = d_{ij}^{in(PP)} + d_{ij}^{in(ASB)}$	$\begin{cases} \underset{\mathcal{D}_{ASB} \to \mathcal{D}_{ASBc}}{\mu_{12}\left(\mathcal{D}_{ASB}\right)} \to \mu_c \ll \mu_0 \\ \underset{\mathcal{D}_{ASB} \to \mathcal{D}_{ASBc}}{E_{22}\left(\mathcal{D}_{ASB}\right)} \to E_c \ll E_0 \end{cases} \rightarrow \begin{cases} \underset{\mathcal{D}_{ASB} \to \mathcal{D}_{ASBc}}{\tau_{12}\left(\mathcal{D}_{ASB}\right)} \to \tau_{12c} \\ \underset{\mathcal{D}_{ASB} \to \mathcal{D}_{ASBc}}{\tau_{22}\left(\mathcal{D}_{ASB}\right)} \to \tau_{22c} \end{cases}$

2.2.2.3 Micro-voiding

The weak discontinuity (ASB) serves as the path for the initiation of micro-voids which coalesce to form a strong discontinuity (crack) and the material fails. Like the ASB, the micro-voids formed in the wake of the ASB also have an effect on the deterioration and kinematic response of the material. In the current study, the contributions to the material effect and kinematics coming from the mechanisms of ASB and MV are clearly distinguished. The presence of the MV induces the following consequences on the material.

- Material consequence

From Fig. 2.8, different configurations of micro-defects developing in the ASB wake can be distinguished. Accordingly, Fig. 2.15 shows an illustration of the possible micro-void shape and orientation.

a) The first simple configuration assumes ideal spherical voids in Fig. 2.15a. In this case, the spherical MV contributes to isotropic degradation ($Tr\dot{\mathbf{D}}$) and hydrostatic plastic strain rate ($\mathbf{d}_v^p$) accounting for volume change.

b) Then the second configuration considered shows elliptical voids which possess an orientation ($\mathbf{n}^*, \mathbf{g}^*$) which may or may not be the same as that of the ASB (Fig. 2.15b). These types of elliptical voids contribute to anisotropic degradation rate ($\dot{\mathbf{D}} = \dot{\mathcal{D}}_{MV}\mathbf{N^*}$; $\mathbf{N^*} = \mathbf{n}^* \otimes \mathbf{n}^*$) and hydrostatic and deviatoric ($\mathbf{d}_s^p$) strain rates (with the corresponding tensor $\mathbf{M^*} = (\mathbf{g}^* \otimes \mathbf{n}^*)^S$) accounting for volume and shape changes respectively.

c) The third configuration in Fig. 2.15c presents micro-cracks with orientation $\mathbf{n}^*$, $\mathbf{g}^*$ and which influence the anisotropic degradation rate ($\dot{\mathcal{D}}_{MV}, \mathbf{N^*}$). When crack opening is not taken into account, there is no MV related strain rate.

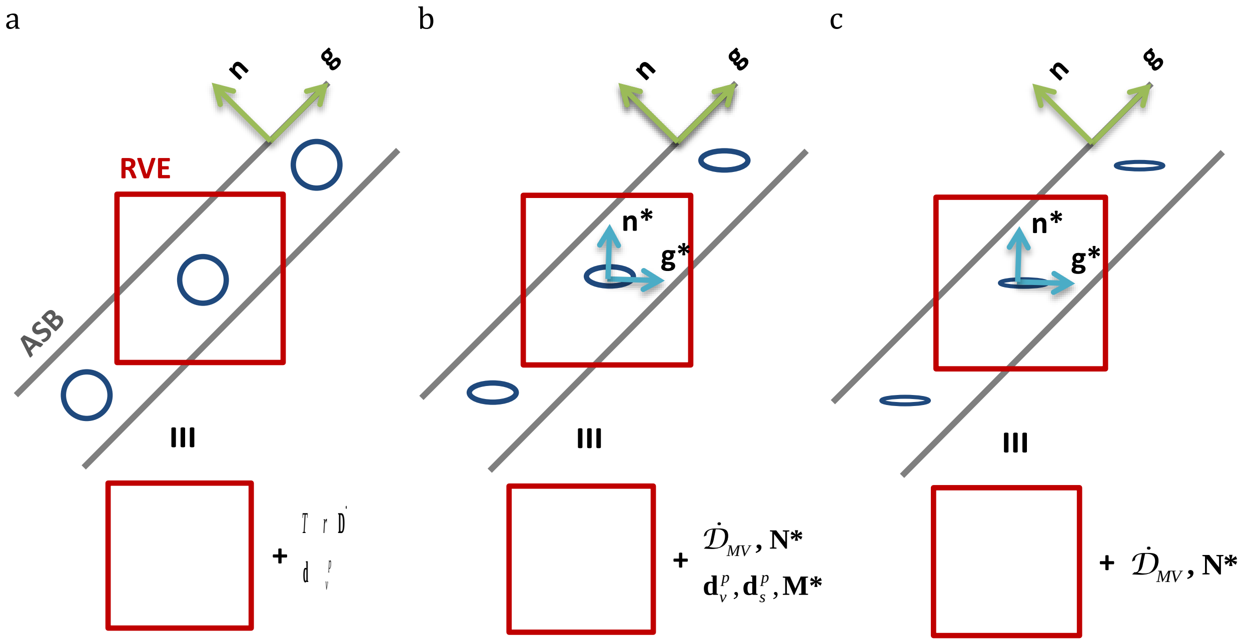

Fig. 2.15 Illustration of micro-void configurations. a) Spherical void configuration b) Ellipsoidal void configuration c) Micro-crack configuration.

During the damage process leading to the crack formation, one has for the configuration in Fig. 2.13 assuming collinearity of the ASB and MV orientations:

$$\begin{cases} \mu_{12}\left(\mathcal{D}_{MV}\right) \underset{\mathcal{D}_{MV}\to\mathcal{D}_{MVc}}{\to} 0 \\ E_{22}\left(\mathcal{D}_{MV}\right) \underset{\mathcal{D}_{MV}\to\mathcal{D}_{MVc}}{\to} 0 \end{cases} \rightarrow \begin{cases} \tau_{12}\left(\mathcal{D}_{MV}\right) \underset{\mathcal{D}_{MV}\to\mathcal{D}_{MVc}}{\to} 0 \\ \tau_{22}\left(\mathcal{D}_{MV}\right) \underset{\mathcal{D}_{MV}\to\mathcal{D}_{MVc}}{\to} 0 \end{cases} \tag{2.9}$$

- Kinematic consequence

Similar to the ASB, the MV induces an additional velocity gradient $\mathbf{L}^{MV}$ as a result of glide velocity $\dot{\gamma}^{MV}$ in the direction of $\mathbf{g}^*$.

$$\begin{aligned} &\mathbf{L}^{in} = \mathbf{L}^{p} + \mathbf{L}^{MV} \\ &\mathbf{L}^{MV} \propto \dot{\gamma}^{MV} \mathbf{g}^* \otimes \mathbf{n}^* + \frac{\dot{\varepsilon}_m^{MV}}{3}\mathbf{I} \end{aligned} \tag{2.10}$$

The MV induced velocity gradient $\mathbf{L}^{MV}$ partitioned into symmetric and antisymmetric parts leading to obtain the strain rate $\mathbf{d}^{MV}$ and spin $\boldsymbol{\omega}^{MV}$ respectively as given below with $\mathbf{T}^* = (\mathbf{g}^* \otimes \mathbf{n}^*)^{AS}$. In case of MV configurations accounting for the void expansion, an additional hydrostatic term appears in the strain rate, where $\mathbf{I}$ is the identity tensor and $\dot{\varepsilon}_m^{MV}$ is the mean strain rate.

$$L_{ij}^{MV} \propto \sum_{\alpha} \dot{\gamma}^{MV,\alpha} g_i^{*\alpha} n_j^{*\alpha} \quad ; \quad \begin{cases} d_{ij}^{MV} \propto \sum_{\alpha} \dot{\gamma}^{MV,\alpha} M_{ij}^{*\alpha} + \dfrac{\dot{\varepsilon}_m^{MV}}{3} I_{ij} \\ \omega_{ij}^{MV} \propto \sum_{\alpha} \dot{\gamma}^{MV,\alpha} T_{ij}^{*\alpha} \end{cases} \tag{2.11}$$

Thus the total inelastic strain rate $\mathbf{d}^{in}$ has now contributions from plasticity and micro-voiding as:

$$d_{ij}^{in} = d_{ij}^{in(PP)} + d_{ij}^{in(MV)} \tag{2.12}$$

Table 2.2 Summary of kinematic and material consequences of MV

Kinematic consequence	Material consequence
$L_{ij}^{MV} \propto \sum_{\alpha} \dot{\gamma}^{MV,\alpha} g_i^{*\alpha} n_j^{*\alpha} + \frac{\dot{\varepsilon}_m^{MV}}{3} I_{ij}$ $\begin{cases} d_{ij}^{MV} \propto \sum_{\alpha} \dot{\gamma}^{MV,\alpha} M_{ij}^{*\alpha} + \frac{\dot{\varepsilon}_m^{MV}}{3} I_{ij} \\ \omega_{ij}^{MV} \propto \sum_{\alpha} \dot{\gamma}^{MV,\alpha} T_{ij}^{*\alpha} \end{cases}$ $d_{ij}^{in} = d_{ij}^{in(PP)} + d_{ij}^{in(MV)}$	$\begin{cases} \underset{\mathcal{D}_{MV} \to \mathcal{D}_{MVc}}{\mu_{12}(\mathcal{D}_{MV}) \to 0} \\ \underset{\mathcal{D}_{MV} \to \mathcal{D}_{MVc}}{E_{22}(\mathcal{D}_{MV}) \to 0} \end{cases} \to \begin{cases} \underset{\mathcal{D}_{MV} \to \mathcal{D}_{MVc}}{\tau_{12}(\mathcal{D}_{MV}) \to 0} \\ \underset{\mathcal{D}_{MV} \to \mathcal{D}_{MVc}}{\tau_{22}(\mathcal{D}_{MV}) \to 0} \end{cases}$

2.2.2.4 Combined effects of ASB and Micro-voiding

The combined effects of the ASB and MV can be modelled in a unified approach.

- Material consequence

The deterioration induced by the ASB and the subsequent MV can be embodied in a single deterioration tensor as follows:

$$D_{ij} = \mathcal{D}_{ASB} N_{ij} + \mathcal{D}_{MV} N_{ij}^{*} \tag{2.13}$$

The effect of the combined deterioration of ASB and MV can be seen on the strain hardening force $r(\kappa)$ as presented in Fig. 2.16. The black curve represents the strain hardening solely as a function of the isotropic hardening variable κ. The blue curve carries an additional influence of the temperature i.e. thermal softening. The purple curve is subjected to the ASB and MV induced deterioration and hence the reduction in hardening or conversely softening behaviour.

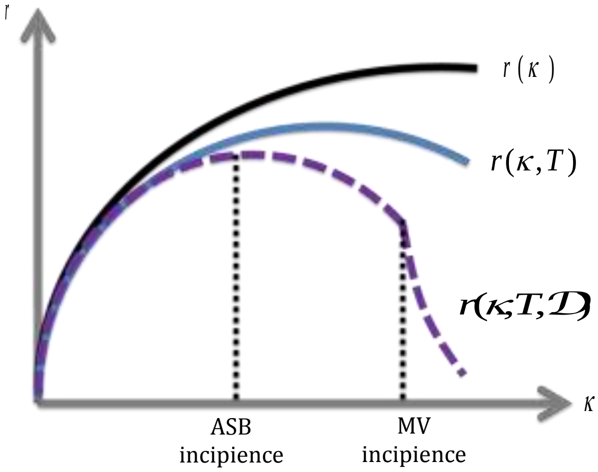

Fig. 2.16 Strain hardening force influenced by thermal softening and ASB+MV induced deterioration

- Kinematic consequence

The ASB and MV induced supplementary kinematics are incorporated in the total inelastic strain rate.

$$d_{ij}^{in} = d_{ij}^{in(PP)} + d_{ij}^{in(ASB)} + d_{ij}^{in(MV)} \tag{2.14}$$

A schematic representation of the kinematics is shown in Fig. 2.17 where F in all the three cases represents the plastic potential in absence of the deterioration mechanisms. Fig. 2.17a shows the case of regular plasticity before the appearance of ASB during which the total inelastic strain rate reduces to $\mathbf{d}^{in} = \mathbf{d}^{in(PP)} = \Gamma^{PP}\mathbf{m}$ where Γ^{PP} is the regular plastic yield intensity and $\mathbf{m}=(3/2)\,\mathrm{x}\left(\mathbf{s}/\sigma_{eq}\right)$ the yield direction. The ASB formation in Fig. 2.17b superposes an additional strain rate $\mathbf{d}^{in(ASB)} = \Gamma^{ASB}\mathbf{M}$, causing progressive deviation of the yield direction. Finally, the micro-voiding in Fig. 2.17c further contributes to the yield intensity Γ^{MV} (assuming collinearity of ASB and MV) and keeps on deviating the yield direction, provoking in particular a plastic expansion termed as $\mathrm{MV}_{\mathrm{hydrostatic}}$.

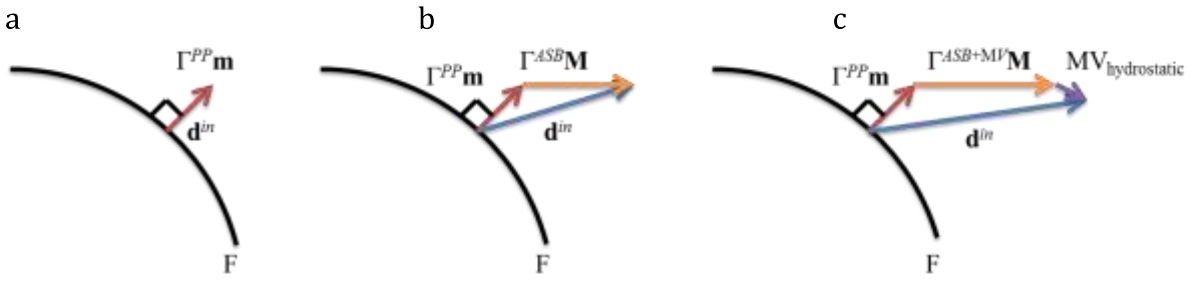

Fig. 2.17 Schematic representation of the evolution of yield direction (a) before ASB initiation (b) during ASB formation (c) in the presence of micro-voids (MV) in the wake of ASB. F is the regular plastic potential in the absence of deterioration mechanisms.

Table 2.3 Summary of kinematic and material consequences of ASB and MV combined

Kinematic consequence	Material consequence
$d_{ij}^{in} = d_{ij}^{in(PP)} + d_{ij}^{in(ASB)} + d_{ij}^{in(MV)}$	$D_{ij} = \mathcal{D}_{ASB} N_{ij} + \mathcal{D}_{MV} N_{ij}^{*}$ $\begin{cases} \underset{\mathcal{D}\to\mathcal{D}_c}{\mu_{12}(\mathcal{D})\to 0} \\ \underset{\mathcal{D}\to\mathcal{D}_c}{E_{22}(\mathcal{D})\to 0} \end{cases} \rightarrow \begin{cases} \underset{\mathcal{D}\to\mathcal{D}_c}{\tau_{12}(\mathcal{D})\to 0} \\ \underset{\mathcal{D}\to\mathcal{D}_c}{\tau_{22}(\mathcal{D})\to 0} \end{cases}$

2.3 CONSTITUTIVE MODELLING

This section deals with the more specific form of the unified constitutive model describing the ASB and the consequent MV induced deterioration. The phenomenological model describing ASB induced failure originally developed by Longère et al [15] has been conceptually improved by Longère and Dragon [24] to incorporate the effects of micro-voiding (MV) in the post critical stage. The model used in the present work is mostly based on the enlarged model in [24] while making some simplifications/modifications. The role of dynamic recrystallization on the onset of ASB in the materials susceptible to this mechanism has also been considered here. The aim of the enriched model is to clearly distinguish the contributions to the degradation coming from the ASB on the one hand and the MV on the other hand. The constitutive model presenting the dynamic recrystallization in the context of the model under consideration can be found in [31].

The constitutive model developed here is a phenomenological one wherein the consequences of the presence of the ASB at the global RVE scale on the regular properties are described. The salient physical features described by the model are:

- SOFTENING INFLUENCING ASB ONSET:
    - **Plastic dissipation** induced thermo-mechanical softening
    - **Dynamic recrystallization** induced softening
- CONSEQUENCES:
    - **Material degradation:** Anisotropic material degradation due to ASB+MV
    - **Kinematics:** Degradation (ASB+MV) induced specific finite strain kinematics

The scale postulate adopted influences the choice of the state variables. From the numerical perspective, the representative volume element (RVE) corresponds to the finite element (FE) integration point. When a reduced integration with a single Gauss point is considered, the FE represents the RVE. Fig. 2.3 illustrates the difference between what is considered a 'small' and 'large' scale postulate. In the large scale postulate, the RVE and the FE contain the shear bands whereas in the small scale postulate the meshing is done on a smaller scale within the bands.

The material within the band is weakened as it is characterized by very high values of shear strain and temperature. Locally within the bands the shear strains may range between 5 and 100, shear strain rates between 10^4 to 10^6/s and the local temperature reaching several hundred degrees (see [32],[33],[11]). As the ASBs are distinctly oriented in space, they induce a form of anisotropy in the mechanical properties of the overall material/structure. In the following, the properties associated with the material inside the ASB are termed as 'singular' and the properties associated with the material outside the band are referred to as 'regular'.

2.3.1 Large anisotropic strain framework

As very large strains and rotations are encountered during the ASB process, a finite elastic-plastic deformation framework is adopted. The following are the simplifying assumptions considered here:

- Moderate elastic deformation
- Strain hardening limited to the isotropic one
- Absence of the strain rate memory

The deformation gradient $\mathbf{F}$ is decomposed as the product $\mathbf{F}=\mathbf{V}^e\mathbf{Q}\mathbf{F}^{dp}$ (see Fig. 2.18), where $\mathbf{V}^e$ denotes the pure elastic stretching, $\mathbf{Q}$ the rotation of anisotropy axes and $\mathbf{F}^{dp}$ the inelastic deformation including plasticity and deterioration.

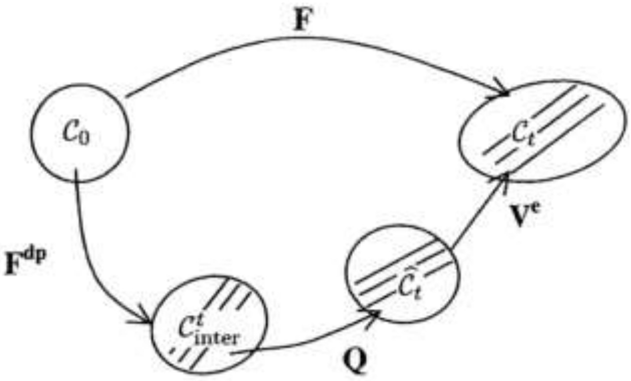

Fig. 2.18 Decomposition of the deformation gradient **F** in the presence of anisotropy. After [15]

This allows for decomposing the total rate of strain rate tensor $\mathbf{d}$ and the spin tensor $\boldsymbol{\omega}$ as follows:

$$\begin{array}{ll}\mathbf{d}=\mathbf{d}^e+\mathbf{d}^{in} & ; \quad \boldsymbol{\omega}=\mathbf{W}+\boldsymbol{\omega}^e+\boldsymbol{\omega}^{in} \\ \mathbf{d}^{in}=\mathbf{d}^{in(PP)}+\mathbf{d}^{in(ASB)}+\mathbf{d}^{in(MV)} & ; \quad \boldsymbol{\omega}^{in}=\boldsymbol{\omega}^{in(PP)}+\boldsymbol{\omega}^{in(ASB)}+\boldsymbol{\omega}^{in(MV)}\end{array} \tag{2.15}$$

where $\mathbf{d}^e$ and $\boldsymbol{\omega}^e$ represent respectively the elastic rate of strain and spin, $\mathbf{W}=\dot{\mathbf{Q}}\mathbf{Q}^T$ the rotation rate of anisotropy axes relative to ASB orientation. The inelastic spin rate $\boldsymbol{\omega}^{in}$ is composed of plastic spin rate $\boldsymbol{\omega}^{in(PP)}$ and the spin rates $\boldsymbol{\omega}^{in(ASB)}$ and $\boldsymbol{\omega}^{in(MV)}$ induced by ASB and MV respectively.

The objective corotational derivative $\overset{\nabla}{\mathbf{A}}$ of a 2nd order tensor **A** is given by

$$\overset{\nabla}{\mathbf{A}}=\dot{\mathbf{A}}-\mathbf{W}\mathbf{A}+\mathbf{A}\mathbf{W} \tag{2.16}$$

Taking into account the negligible elastic rotation $\boldsymbol{\omega}^e$ and relative small regular plastic spin $\boldsymbol{\omega}^{in(PP)}$, the rotation rate $\mathbf{W}$ is reduced to:

$$\mathbf{W}=\boldsymbol{\omega}-\left(\boldsymbol{\omega}^{in(ASB)}+\boldsymbol{\omega}^{in(MV)}\right) \tag{2.17}$$

In the following, the tensors $\mathbf{X}$ defined in the intermediate configuration C_{inter}^t are transported to the current one C_t denoted by a tilde $\tilde{\mathbf{X}}$ via $\tilde{\mathbf{X}}=\mathbf{Q}\mathbf{X}\mathbf{Q}^{\mathbf{T}}$.

2.3.2 Thermodynamic framework

In the framework of irreversible thermodynamics, the (regular) state variables to account for accordingly are: the elastic strain tensor $\mathbf{e^e} = \ln \mathbf{V^e}$, the absolute temperature T, the isotropic hardening variable κ. The singular temperature and other singular state variables are not explicitly calculated in the model, but their effects on the material degradation are embodied in the degradation tensor $\tilde{\mathbf{D}}$.

Helmholtz free energy $\psi\left(\mathbf{e}^e, T, \kappa; \tilde{\mathbf{D}}\right)$ is assumed as the state potential comprising of a reversible part $\psi^e\left(\mathbf{e}^e, T; \tilde{\mathbf{D}}\right)$, a stored energy part $\psi^p\left(T, \kappa; \tilde{\mathbf{D}}\right)$ and a purely thermal part $\psi^T\left(T\right)$ as shown in (2.18). The presence of ASB affects both the elastic and plastic properties.

$$\psi\left(\mathbf{e}^e, T, \kappa; \tilde{\mathbf{D}}\right) = \psi^e\left(\mathbf{e}^e, T; \tilde{\mathbf{D}}\right) + \psi^p\left(T, \kappa; \tilde{\mathbf{D}}\right) + \psi^T\left(T\right) \tag{2.18}$$

Constitutive state laws derived from the state potential in (2.18) allow for expressing the elastic Kirchhoff stress tensor $\boldsymbol{\tau}$, strain hardening force r, deterioration driving force $\tilde{\mathbf{G}}$ and entropy s, as follows:

$$\begin{aligned}
&\tau_{ij} = \rho_0 \frac{\partial \psi}{\partial e^e_{ij}} = \rho_0 \frac{\partial \psi^e}{\partial e^e_{ij}} \;\; ; \; r = \rho_0 \frac{\partial \psi}{\partial \kappa} = \rho_0 \frac{\partial \psi^p}{\partial \kappa} \\
&\tilde{G}_{ij} = -\rho_0 \frac{\partial \psi}{\partial \tilde{D}_{ij}} = -\left(\rho_0 \frac{\partial \psi^e}{\partial \tilde{D}_{ij}} + \rho_0 \frac{\partial \psi^p}{\partial \tilde{D}_{ij}} \right) \\
&\rho_0 s = -\rho_0 \frac{\partial \psi}{\partial T} = -\left(\rho_0 \frac{\partial \psi^e}{\partial T} + \rho_0 \frac{\partial \psi^p}{\partial T} + \rho_0 \frac{d\psi^T}{dT} \right)
\end{aligned} \tag{2.19}$$

The model should satisfy the Clausius-Duhem inequality in order to be consistent with the irreversible thermodynamics. Therefore the intrinsic dissipation $\mathfrak{D}_{\text{int}}$ is expressed as:

$$\mathfrak{D}_{\text{int}} = \tau_{ij} d_{ji} - \rho_0 (\dot{\psi} + s\dot{T}) \geq 0 \tag{2.20}$$

$\mathfrak{D}_{\text{int}}$ is decomposed into regular plasticity related term $\mathfrak{D}_{\text{reg}}$ and singular ASB+MV induced term $\mathfrak{D}_{\text{sing}}$. Using the Gibbs relation $\rho_0 \dot{\psi} = \tau_{ij} d^e_{ij} + r\dot{\kappa} - \tilde{G}_{ij} \dot{\tilde{D}}_{ij} - \rho_0 s\dot{T}$ the dissipation components are written as:

$$\begin{aligned}&\mathfrak{D}_{\text{int}} = \mathfrak{D}_{\text{reg}} + \mathfrak{D}_{\text{sing}} \geq 0\\&\mathfrak{D}_{\text{reg}} = \tau_{ij} : d^{p}_{ji} - r\dot{\kappa} \geq 0 \text{ ; } \mathfrak{D}_{\text{sing}} = \tau_{ij} : d^{d}_{ji} + \tilde{G}_{ij} : \overset{\nabla}{\tilde{D}}_{ji} \geq 0\end{aligned} \tag{2.21}$$

The normality rule is preserved during phases of ASB and MV such that a collinearity exists between the regular plastic strain rate $d_{ij}^{in(PP)}$ and the deviatoric part of the Kirchhoff stress tensor $\mathbf{s}$, the singular strain rates ($d_{ij}^{in(ASB)}, d_{ij}^{in(MV)}$) and the orientation tensor ($\tilde{\mathbf{M}}, \tilde{\mathbf{M}}^*$) and finally the degradation rate tensor ($\overset{\nabla}{\tilde{\mathbf{D}}}^{ASB}, \overset{\nabla}{\tilde{\mathbf{D}}}^{MV}$) and the tensor ($\tilde{\mathbf{N}}$, $\tilde{\mathbf{N}}^*$). The evolution laws are correspondingly derived from dissipation potentials namely the viscoplastic potential ϕ_p and viscous-degradation potential $\phi_d = \phi_{ASB} + \phi_{MV}$ as:

$$\begin{aligned}&d_{ij}^{in} = \frac{\partial \phi_p}{\partial \tau_{ij}} = d_{ij}^{in(PP)} + d_{ij}^{in(ASB)} + d_{ij}^{in(MV)}\\&-\dot{\kappa} = \frac{\partial \varphi_p}{\partial r}\\&\overset{\nabla}{\tilde{D}}_{ij} = \frac{\partial \phi_d}{\partial G_{ij}} = \overset{\nabla}{\tilde{D}}{}_{ij}^{ASB} + \overset{\nabla}{\tilde{D}}{}_{ij}^{MV}\end{aligned} \tag{2.22}$$

The evolution laws in turn require the definition of a plastic potential H and/or a yield function F depending on whether non-associated ($\mathrm{H} \neq \mathrm{F}$) or associated flow rule ($\mathrm{H} = \mathrm{F}$) is followed.

2.3.3 Constitutive equations

A more precise form of the constitutive equations adopted in the current study is presented in this section. In the following sections, for simplification, elliptical void shape is assumed with the orientation along the direction of the ASB as represented in Fig. 2.19. Hence the structural tensors corresponding to the ASB and MV are considered to be the same ($\mathbf{N}, \mathbf{M}$).

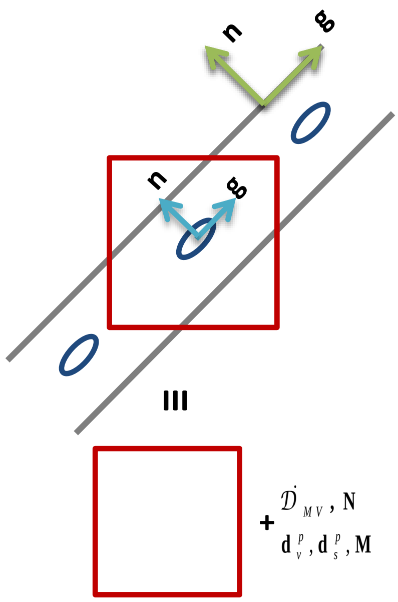

Fig. 2.19 Elongated micro-voids oriented in the direction of ASB

2.3.3.1 Preliminary considerations

- *Elastic stress tensor*

Following the work of Halm and Dragon [34], see also Longère and Dragon[15], the elastic stress tensor in presence of induced anisotropic degradation is assumed of the form:

$$\tau_{ij} = \rho_0 \frac{\partial \psi}{\partial e^e_{ij}} = \rho_0 \frac{\partial \psi^e}{\partial e^e_{ij}} = \lambda e^e_{kk} I_{ij} + 2\mu e^e_{ij} - \bar{\alpha} K \Delta T\, I_{ij} - a\left(e^e_{mn}\tilde{D}_{nm} I_{ij} + e^e_{kk}\tilde{D}_{ij}\right) - 2b\left(e^e_{ik}\tilde{D}_{kj} + \tilde{D}_{ik} e^e_{kj}\right) \tag{2.23}$$

The form given to the stress tensor in (2.23) is such that it takes into account material degradation based on the orientation of the shear bands. λ and μ represent the Lamé elasticity constants and $K = (3\lambda + 2\mu)/3$ the bulk modulus. a and b are ASB+MV related constants inducing orthotropic elastic energy degradation – they may have different values for ASB and MV in a future work. In the thermal part, $\bar{\alpha}$ represents the thermal expansion coefficient, T_0 the initial temperature and $\Delta T = T - T_0$ the rise in temperature.

Consider now the illustration in Fig. 2.20 (copy of Fig. 2.13), the normal to the ASB is in direction 2, in which case, the deterioration tensor is calculated below:

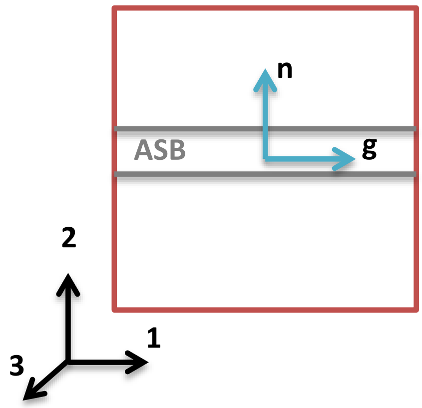

Fig. 2.20 Illustration of a case of ASB orientation

$$\mathbf{n}=\begin{pmatrix}0\\1\\0\end{pmatrix}\rightarrow\mathbf{D}=\mathcal{D}\begin{bmatrix}0 & 0 & 0\\ & 1 & 0\\ sym & & 0\end{bmatrix} \tag{2.24}$$

By neglecting the thermal dilatation, the components of $\boldsymbol{\tau}$ for the above case (Fig. 2.20) deduced from (2.23) are:

$$\begin{cases}\tau_{11}=\lambda e^e_{kk}+2\mu e^e_{11}-ae^e_{22}\tilde{D}_{22}\\ \quad =\left(\lambda+2\mu\right)e^e_{11}+\left(\lambda-a\tilde{D}_{22}\right)e^e_{22}+\lambda e^e_{33}\\ \tau_{22}=\lambda e^e_{kk}+2\mu e^e_{22}-a\left[e^e_{22}\tilde{D}_{22}+e^e_{kk}\tilde{D}_{22}\right]-2b\left(e^e_{22}\tilde{D}_{22}+\tilde{D}_{22}e^e_{22}\right)\\ \quad =\lambda\left(e^e_{11}+e^e_{22}+e^e_{33}\right)+2\mu e^e_{22}-a\left[e^e_{22}\tilde{D}_{22}+\left(e^e_{11}+e^e_{22}+e^e_{33}\right)\tilde{D}_{22}\right]-4b\tilde{D}_{22}e^e_{22}\\ \quad =\left(\lambda-a\tilde{D}_{22}\right)\left(e^e_{11}+e^e_{33}\right)+\left[\left(\lambda-2a\tilde{D}_{22}\right)+2\left(\mu-2b\tilde{D}_{22}\right)\right]e^e_{22}\\ \tau_{33}=\lambda e^e_{kk}+2\mu e^e_{33}-ae^e_{22}\tilde{D}_{22}\\ \quad =\left(\lambda+2\mu\right)e^e_{33}+\left(\lambda-a\tilde{D}_{22}\right)e^e_{22}+\lambda e^e_{11}\end{cases} \tag{2.25}$$

$$\begin{cases}\tau_{12}=2\mu e^e_{12}-2be^e_{12}\tilde{D}_{22}=2\left(\mu-b\tilde{D}_{22}\right)e^e_{12}\\ \tau_{13}=2\mu e^e_{13}\\ \tau_{23}=2\mu e^e_{23}-2b\tilde{D}_{22}e^e_{23}=2\left(\mu-b\tilde{D}_{22}\right)e^e_{23}\end{cases}$$

The resulting (symmetric) stiffness matrix $\mathbf{C}$, $\boldsymbol{\tau}=\mathbf{C}:\mathbf{e}^e$, reads

$$[C]=\begin{bmatrix} \lambda+2\mu & (\lambda-a\mathcal{D}) & \lambda & 0 & 0 & 0 \\ & (\lambda-2a\mathcal{D})+2(\mu-2b\mathcal{D}) & (\lambda-a\mathcal{D}) & 0 & 0 & 0 \\ & & \lambda+2\mu & 0 & 0 & 0 \\ & & & 2(\mu-b\mathcal{D}) & 0 & 0 \\ & & & & 2\mu & 0 \\ sym & & & & & 2(\mu-b\mathcal{D}) \end{bmatrix} \tag{2.26}$$

Failure under shear loading yields an upper bound for deterioration intensity $\mathcal{D}_c$ as shown below:

$$\tau_{12}=2(\mu-b\mathcal{D}_c)e^{e}_{12}=0 \quad \rightarrow \quad \mathcal{D}_c=\frac{\mu}{b}\rightarrow\mathcal{D}_c(b=\mu)=1 \tag{2.27}$$

A reduction in the material strength is seen in the direction normal to the ASB (τ_{22}) and in the corresponding shear direction (τ_{12}). It is seen that the constants $a<0$ and $b>0$ contribute to the reduction in Young's modulus E_{22} whereas only b acts in the reduction of the shear modulus μ_{12}.

- *Strain hardening force*

Experimental observations have shown that in absence of ASB and MV the coupling between strain hardening and thermal softening may be described in a product form allowing for using the method of separation of variables

$$r(\kappa,T)=\rho_0\frac{\partial\psi}{\partial\kappa}=\rho_0\frac{\partial\psi^{p}}{\partial\kappa}=h'(\kappa)g(T) \tag{2.28}$$

The form of the thermal softening corresponding to steel is shown in (2.29) where υ is the material specific thermal softening constant

$$g(T)=\exp(-\upsilon T) \tag{2.29}$$

For materials such as titanium alloys, in accordance with experimental observations, the function in (2.30) satisfies the thermal softening characteristics with T_{ref} being a reference temperature such that $g(T_{ref})=0$. $\langle . \rangle$ are Macauley brackets defined as $\langle x\rangle=\max(x,0)$.

$$g(T) = \left\langle 1 - \left(\frac{T}{T_{ref}} \right)^{t} \right\rangle \tag{2.30}$$

The strain hardening function is expressed in (2.31) where R_∞ is related to the saturation of isotropic hardening (Voce law).

$$h'(\kappa) = R_\infty \left[1 - \exp\left(-k\kappa \right) \right]; h(\kappa) = R_\infty \left[\kappa + \frac{1}{k} \exp\left(-k\kappa \right) \right] \tag{2.31}$$

We are here assuming that this product form can be extended for ASB and MV

$$r\left(\kappa, T; \tilde{\mathrm{D}} \right) = \rho_0 \frac{\partial \psi}{\partial \kappa} = \rho_0 \frac{\partial \psi^p}{\partial \kappa} = h'\left(\kappa \right) g\left(T \right) w\left(\tilde{\mathrm{D}} \right) \tag{2.32}$$

In the following equations the thermal softening function in (2.29) is used. The deterioration function $w(\tilde{\mathbf{D}})$ is expressed below where χ_1 and χ_2 are ASB+MV related deterioration constants. The form of the deterioration function $w(\tilde{\mathbf{D}})$ is adopted of the same exponential form as the thermal softening function in (2.29) as the singular temperature rise within the shear band is the main contributor to the material deterioration. The expression of $w(\tilde{\mathbf{D}})$ in (2.33) is tentatively retained for other materials such as Ti alloys even though the form of their thermal softening function is different.

$$w(D_{ij}) = \exp\left(-\chi_1 \tilde{D}_{ii} - \frac{\chi_2}{2} \tilde{D}_{ij} \tilde{D}_{ji} \right) \tag{2.33}$$

2.3.3.2 State potential

According to the preliminary considerations above, the state potential reads after integration of the constitutive state laws in (2.23) and (2.32) with respect to their different arguments:

$$\psi\left(\mathbf{e}^e, T, \kappa; \tilde{\mathbf{D}} \right) = \psi^e\left(\mathbf{e}^e, T; \tilde{\mathbf{D}} \right) + \psi^p\left(T, \kappa; \tilde{\mathbf{D}} \right) + \psi^T\left(T \right)$$

$$\begin{cases} \rho_0 \psi^e\left(\mathbf{e}^e, T; \tilde{\mathbf{D}} \right) = \frac{1}{2} \mathbf{e}^e : \mathbf{C}(\tilde{\mathbf{D}}) : \mathbf{e}^e - \bar{\alpha} K . Tr(\mathbf{e}^e) . \Delta T \\ \rho_0 \psi^p\left(T, \kappa; \tilde{\mathbf{D}} \right) = h(\kappa) g(T) w(\tilde{\mathbf{D}}) \\ \rho_0 \psi^T\left(T \right) = -\rho_0 \frac{C}{2T_0} \Delta T^2 \end{cases} \tag{2.34}$$

2.3.3.3 Constitutive state laws

The complete expressions of the conjugate forces associated to the state variables, considering steel oriented thermal softening function, are shown below:

$$\begin{cases} \tau_{ij} = \lambda e^e_{kk} I_{ij} + 2\mu e^e_{ij} - \bar{\alpha} K \Delta T\, I_{ij} - a\left(e^e_{mn}\tilde{D}_{nm} I_{ij} + e^e_{kk}\tilde{D}_{ij}\right) - 2b\left(e^e_{ik}\tilde{D}_{kj} + \tilde{D}_{ik} e^e_{kj}\right) \\ r = R_\infty\left[1-\exp(-k\kappa)\right]\exp(-\upsilon T)\exp\left(-\chi_1\tilde{D}_{kk} - \frac{\chi_2}{2}\tilde{D}_{kl}\tilde{D}_{lk}\right) \\ \tilde{G}_{ij} = a e^e_{kk} e^e_{ij} + 2b e^e_{ik} e^e_{kj} + R_\infty\left[\kappa + \frac{1}{k}\exp(-k\kappa)\right] \\ \qquad .\exp(-\upsilon T)\exp\left(-\chi_1\tilde{D}_{kk} - \frac{\chi_2}{2}\tilde{D}_{kl}\tilde{D}_{lk}\right)\left[\chi_1 I_{ij} + \chi_2 \tilde{D}_{ij}\right] \end{cases} \tag{2.35}$$

The expression of the entropy is not detailed here. The diminution of the stress $\boldsymbol{\tau}$ is caused by the isotropic heating and ASB+MV induced anisotropic degradation. The competition between hardening and softening is embodied in the isotropic hardening conjugate force r: the strain hardening capability $\partial r / \partial \kappa$ is decreased by the thermal softening function $g(T)$. In addition, as the deterioration $\mathbf{D}$ evolves, the deterioration related function $w(\tilde{\mathbf{D}})$ magnifies the loss of the strain hardening capability as illustrated in Fig. 2.16. In isothermal conditions and in the absence of deterioration, r reaches a saturation stress $R_\infty\left[1-\exp(-k\kappa)\right]\exp(-\upsilon T_0)$ relative to isotropic hardening. The deterioration conjugate force $\tilde{\mathbf{G}}$ has contributions from the reversible part ψ^e and stored energy part ψ^p of the free energy which correspondingly represent the elastic and stored energy release rate. $\tilde{\mathbf{G}}$ in the following is contained in ΔG_{ASB} and ΔG_{MV} through the scalar quantity G obtained by the projection of $\tilde{\mathbf{G}}$ onto the band plane. In particular, the values of G at the ASB and MV onset are considered namely G_{ASB} and G_{MV} respectively and the quantities ΔG_{ASB} and ΔG_{MV} which are defined as:

$$\begin{aligned} G &= \tilde{G}_{ij} N_{ji} \\ \Delta G_{ASB} &= G - G_{ASB} \\ \Delta G_{MV} &= G - G_{MV} \end{aligned} \tag{2.36}$$

It is to be noted that the deterioration conjugate force exists and evolves even before the deterioration onset. A finite supply of local energy release rate (G_{ASB}, G_{MV}) is required to activate the deterioration (ASB, MV). The deterioration onset criteria and calculation of G_{ASB} and G_{MV} are defined in section 2.4.

2.3.3.4 Yield function

Various void induced damage models exist in the literature. Lemaitre [35] modelled ductile damage considering non-dilatant effect of void growth. The dilatant void growth models of Rousselier [36] and GTN (Gurson-Tvergaard-Needleman) ([37],[38]) are widely used damage plasticity models to describe ductile damage. The ASB induced degradation, in the present study, was initially described using a thermo/elastic-viscoplastic-deterioration (TEVPD) model. Now, in order to describe the post critical micro-voiding, rather than using another plasticity–ductile damage coupled model, a 'unified approach' is adopted wherein the MV induced consequences are merged within the TEVPD framework without distorting much its formal structure. The unified enlarged model has some analogies with Rousselier model [36] for its dependence on hydrostatic stress via an exponential function that allows for reproducing void growth under shear loading.

The yield function F_{total} when both the ASB and MV mechanisms are in operation reads:

$$\mathrm{F}_{total} = \sigma_{eq} + 3\xi\,\Delta G_{MV}^{2} \exp\left(\frac{\sigma_m}{\bar{\sigma}}\right) - \left(R_0 + r\right) = \sigma_v \geq 0 \tag{2.37}$$

where σ_{eq} is the transformed equivalent stress, $\left(R_0 + r\right)$ the rate independent yield stress with r the strain hardening force, σ_v the strain rate induced overstress, $\sigma_m = \tau_{kk}/3$ the mean stress and $\bar{\sigma}$ a reference stress. R_0 is expressed in (2.38) with R_{int} being the internal stress (thermal softening function related to steel).

$$R_0 = R_{\mathrm{int}} \exp(-\upsilon T) \exp\left(-\chi_1 \tilde{D}_{kk} - \frac{\chi_2}{2} \tilde{D}_{kl} \tilde{D}_{lk}\right) \tag{2.38}$$

The second term of the expression of F_{total} containing σ_m corresponds to the expansion of micro-voids with ξ being the related material constant. The ΔG_{MV} in this term has been modified to ΔG_{MV}^{2} contrary to the previous work ([24],[39],[25]) in order to be consistent with the MV incipience while deriving the deterioration rate expressed in $(2.46)_2$ below.

2.3.3.5 Equivalent stress

A transformed equivalent stress σ_{eq} is used here which incorporates the regular plasticity and the anisotropy induced in the plastic flow provoked by the formation (onset and evolution) of the strongly oriented deterioration mechanisms at stake (ASB+MV) through a 4th order tensor $\mathbf{P}$ as shown below:

$$\sigma_{eq} = \sqrt{\frac{3}{2}\mathbf{s}:\mathbf{P}\left(\Delta G_{ASB}, \Delta G_{MV}\right):\mathbf{s}} \equiv \sqrt{\sigma_{VM}{}^{2} + \sigma_{ASB}{}^{2} + \sigma_{MV}{}^{2}} \tag{2.39}$$

where $\mathbf{s}$ is the deviatoric part of the stress tensor. σ_{eq} therefore has contributions from the regular and singular mechanisms and is composed of the regular plastic von Mises equivalent stress σ_{VM} and the singular stresses induced by ASB - σ_{ASB} and then by MV- σ_{MV}.

The components of σ_{eq} are expressed in (2.40) with η_{ASB} and η_{MV} being material constants relative to the corresponding mechanisms, $\tau_{res} = \mathbf{s}:\mathbf{M}$ and $\sigma_{N} = \boldsymbol{\tau}:\mathbf{N}$ the shear stress resolved along the band plane and stress normal to the band plane, respectively.

$$\begin{aligned} \sigma_{VM} &= \sqrt{\frac{3}{2}\mathbf{s}:\mathbf{s}} \\ \sigma_{ASB} &= \sqrt{\eta_{ASB}\Delta G_{ASB}^{2}(3\tau_{res}^{2} + 3\langle\sigma_{N}\rangle^{2})} \\ \sigma_{MV} &= \sqrt{\eta_{MV}\Delta G_{MV}^{2}(3\tau_{res}^{2} + 3\langle\sigma_{N}\rangle^{2})} \end{aligned} \tag{2.40}$$

A power of 2 is used for ΔG_{ASB} and ΔG_{MV} terms in the above expression in order to ensure the concomitance of the deterioration induced rates while deriving their expressions later in (2.44) and (2.46) below.

One can note that, in the absence of MV ($\Delta G_{MV} = 0$), F_{total} reduces to F_{PP+ASB} i.e. yield function in the presence of ASB only. Further in the absence of ASB ($\Delta G_{ASB} = 0$), Von Mises yield criterion F_{PP} is followed. The different possible cases of the yield function in the presence or absence of ASB and MV are shown in Table 2.4.

Table 2.4 Form of yield function in the presence or absence of ASB and MV

Operating Mechanisms	ΔG	$\sigma_{eq}{}^{2}$	$\mathrm{F} = \sigma_{v} \geq 0$
$PP + ASB + MV$	$\Delta G_{ASB} \neq 0$ $\Delta G_{MV} \neq 0$	$\sigma_{VM}{}^{2} + \sigma_{ASB}{}^{2} + \sigma_{MV}{}^{2}$	$\mathrm{F}_{total} = \sigma_{eq} + 3\xi\,\Delta G_{MV}^{2}\exp\left(\frac{\sigma_{m}}{\bar{\sigma}}\right) - \left(R_{0} + r\right)$
$PP + ASB$	$\Delta G_{ASB} \neq 0$ $\Delta G_{MV} = 0$	$\sigma_{VM}{}^{2} + \sigma_{ASB}{}^{2}$	$\mathrm{F}_{PP+ASB} = \sigma_{eq} - \left(R_{0} + r\right)$
PP	$\Delta G_{ASB} = 0$ $\Delta G_{MV} = 0$	$\sigma_{VM}{}^{2}$	$\mathrm{F}_{PP} = \sigma_{eq} - \left(R_{0} + r\right)$

The expressions for the singular contributions to the equivalent stress are modified here from the earlier versions in order to take into account the loss of strength of the material due to ASB and the subsequent MV in the direction normal to the band during tension loading by adding the stress term $\sigma_N = \boldsymbol{\tau} : \mathbf{N}$ in the expression of the transformed equivalent stress. The scalar function preceding $\mathbf{M} \otimes \mathbf{M}$ in the original expression of $\mathbf{P}$ (see equation (36) in [24]) has been limited here to a single term. In a certain way, the a posteriori addition of σ_N in the transformed equivalent stress allows for palliating the aforementioned truncation. During tension loading in the direction normal to the shear band, presumably the entire load is carried by the shear bands. During normal compression loading, when $\tau_{res} = 0$ and $\langle \sigma_N \rangle = 0$, the RVE is supposed to contain no shear bands and the entire load is carried by the regular matrix material.

A scenario in which such a complex loading sequence is encountered is a projectile impact on Kalthoff and Winkler (KW)-type double notched specimen as shown in Fig. 2.21 [23]. When the projectile impacts, a compression wave travels collinearly to the impact axis through the impacted part which is translated to local shearing in the notch tip leading to the formation of ASB. The expansion of the impacted part due to Poisson's effect causes another compression wave to travel in a direction perpendicular to the impacted axis. This wave is reflected as a tension wave creating a tension loading in the shear localized region.

It is to be remarked that ASB induced deterioration is in operation during the loading duration when the shear band is still soft. With longer duration or during interrupted loading, the material within the ASB would possibly undergo phase transformation due to quenching by the surrounding regular material and become harder. In this case, the material regains its near original strength except for the irreversible MV deterioration. This remark is to be taken into account in the prospective work.

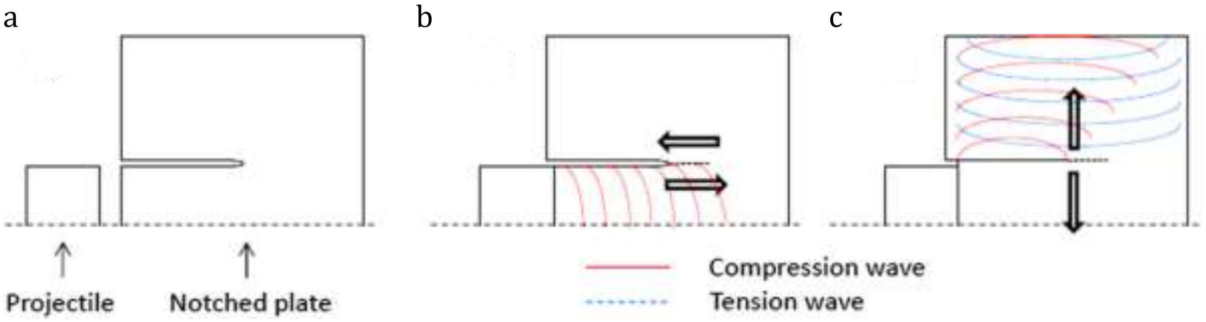

Fig. 2.21 After [23]. Schematic representation of possible wave propagation during KW impact test. (a) Configuration before impact accounting for plane symmetry. (b) Shear wave in the impact direction propagation. (c) Tension wave in the perpendicular direction

2.3.3.6 Viscoplastic and viscous-damage potential

The existence of viscoplastic potential ϕ_p and viscous-deterioration potential ϕ_{ASB}, ϕ_{MV} of Norton-Perzyna's type is assumed in the form of power law:

$$\varphi_p = \frac{Y}{n+1}\left\langle \frac{\mathrm{H}}{Y} \right\rangle^{n+1} \; ; \; \varphi_{ASB} = \frac{Z}{m+1}\left\langle \frac{\mathrm{H}}{Z} \right\rangle^{m+1} \; ; \; \varphi_{MV} = \frac{W}{q+1}\left\langle \frac{\mathrm{H}}{W} \right\rangle^{q+1} \tag{2.41}$$

Y and n are viscous constants corresponding to the regular plasticity; Z, m and W, q are time-dependence related constants corresponding to the ASB and MV degradation mechanisms respectively.

2.3.3.7 Evolution laws

A non-associated plasticity is followed such that the plastic potential $\mathrm{H} = \mathrm{F}_{total}\left(\langle \sigma_N \rangle \equiv 0\right)$ as expressed below.

$$\begin{gathered}
\mathrm{H} = \sigma_{eq} + 3\xi\,\Delta G_{MV}^2 \exp\left(\frac{\sigma_m}{\bar{\sigma}}\right) - \left(R_0 + r\right) = \sigma_v \geq 0 \\
with \quad \sigma_{eq}{}^2 = \sigma_{VM}{}^2 + \sigma_{ASB}{}^2 + \sigma_{MV}{}^2 \\
\sigma_{VM} = \sqrt{\frac{3}{2}\mathrm{s}:\mathrm{s}} \; ; \; \sigma_{ASB} = \sqrt{3\eta_{ASB}\Delta G_{ASB}^2 \tau_{res}^2} \; ; \sigma_{MV} = \sqrt{3\eta_{MV}\Delta G_{MV}^2 \tau_{res}^2}
\end{gathered} \tag{2.42}$$

The viscoplastic multiplier Λ_p and viscous-deterioration multipliers $\Lambda_{ASB}, \Lambda_{MV}$ are expressed below.

$$\Lambda_p = \left\langle \frac{\partial \phi_p}{\partial F} \right\rangle = \left\langle \frac{\mathrm{H}}{Y} \right\rangle^n \; ; \; \Lambda_{ASB} = \left\langle \frac{\partial \phi_{ASB}}{\partial F} \right\rangle = \left\langle \frac{\mathrm{H}}{Z} \right\rangle^m \; ; \; \Lambda_{MV} = \left\langle \frac{\partial \phi_{MV}}{\partial F} \right\rangle = \left\langle \frac{\mathrm{H}}{W} \right\rangle^q \tag{2.43}$$

The detailed rate equations derived from the plastic potential according to the normality rule are shown below. In addition to the deviatoric component, the MV induced strain rate $\mathbf{d}^{in(MV)}$ is also composed of a hydrostatic component. The MV expansion described by the dependence on the mean stress according to $\exp(\sigma_m / \bar{\sigma})$ was initially proposed by Rice and Tracey [40].

$$\begin{cases} d_{ij}^{in(PP)} = \dfrac{3}{2}\Lambda_P \dfrac{s_{ij}}{\sigma_{eq}} \\ d_{ij}^{in(ASB)} = 3\Lambda_P \dfrac{\eta_{ASB}\Delta G_{ASB}^2 \tau_{res}}{\sigma_{eq}} M_{ij} \\ d_{ij}^{in(MV)} = 3\Lambda_P \left[\dfrac{\eta_{MV}\Delta G_{MV}^2 \tau_{res}}{\sigma_{eq}} M_{ij} + \dfrac{\xi}{3\bar{\sigma}} \Delta G_{MV}^2 \exp\left(\dfrac{\sigma_m}{\bar{\sigma}} \right) I_{ij} \right] \end{cases} \tag{2.44}$$

$$\dot{\kappa} = \Lambda_p \tag{2.45}$$

$$\begin{cases} \overset{\nabla}{D}{}_{ij}^{ASB} = \dfrac{3\tau_{res}^2}{\sigma_{eq}} \Lambda_{ASB}\eta_{ASB}\Delta G_{ASB} N_{ij} \\ \overset{\nabla}{D}{}_{ij}^{MV} = 3\Lambda_{MV} \left[\dfrac{\tau_{res}^2}{\sigma_{eq}} \eta_{MV}\Delta G_{MV} + 2\xi\Delta G_{MV} \exp\left(\dfrac{\sigma_m}{\bar{\sigma}} \right) \right] N_{ij} \end{cases} \tag{2.46}$$

It is to be noted that in the present study void expansion is modelled irreversibly and the void closure which may take place during change of the loading sign is not taken into consideration. The inclusion of ΔG_{MV}^2 in the void expansion term of the yield function translates into ΔG_{MV}^2 and ΔG_{MV} in the corresponding terms of $d_{ij}^{in(MV)}$ and $\overset{\nabla}{D}{}_{ij}^{MV}$ respectively. This ensures the concomitance of the deviatoric and hydrostatic terms of the rate equation relevant to MV.

The components of the deterioration induced spin rates can be deduced from (2.7) and (2.44) as:

$$\begin{aligned} \omega_{ij}^{in(ASB)} &= 3\Lambda_P \frac{\eta_{ASB}\Delta G_{ASB}^2 \tau_{res}}{\sigma_{eq}} T_{ij} \\ \omega_{ij}^{in(MV)} &= 3\Lambda_P \frac{\eta_{MV}\Delta G_{MV}^2 \tau_{res}}{\sigma_{eq}} T_{ij} \end{aligned} \tag{2.47}$$

2.3.3.8 Viscous stress

The viscous stress in (2.42)$_1$ is deduced from (2.43)$_1$ and (2.45) as follows:

$$\sigma_v = Y \dot{\kappa}^{1/n} \tag{2.48}$$

It is reminded that Y and n are viscous constants corresponding to the regular plasticity and as such do not depend on D.

2.3.3.9 Temperature rise

The regular temperature rate is calculated from the intrinsic plastic dissipation expressed in (2.21) assuming adiabatic conditions as:

$$\rho c\dot{T} = \tau_{ij} : d_{ji}^{p} - r\dot{\kappa} \tag{2.49}$$

As the dissipation progressively concentrates within the band during the ASB process, the regular temperature rate accordingly vanishes and the regular temperature saturates; further cooling during unloading should be accounted for in prospective works.

2.4 DETERIORATION INCIPIENCE CRITERIA

The mechanisms leading to onset of the ASB and MV and the corresponding criteria adopted are discussed in the current section.

2.4.1 Assumption of adiabatic conditions

While resolving the thermomechanical problem, the heat conduction attenuates the temperature rise and as a result postpones the ASB onset, see e.g. Bonnet-Lebouvier et al.[13]. The isothermal vs adiabatic condition can be deduced from θ the ratio of the characteristic test time t_{test} and the thermal diffusion time t_{dif}. The expression for θ obtained from [41] is shown below :

$$\theta = \frac{t_{test}}{t_{dif}} = \frac{2\alpha_k}{\left[L_0 \exp(\Delta\varepsilon)\right]^2}\frac{\Delta\varepsilon}{\dot{\varepsilon}} \tag{2.50}$$

where L_0 is the characteristic length of the specimen, α_k the thermal diffusivity, $\Delta\varepsilon$ change in strain and $\dot{\varepsilon}$ the strain rate. Isothermal condition can be assumed when $\theta >> 1$. Adiabatic condition is assured when $\theta << 1$. When $\theta \approx 1$ coupled condition exists. Assigning $\theta = 1$, a critical strain rate $\dot{\varepsilon}_c$ can be calculated for transition from isothermal to adiabatic conditions for a given L_0. Adiabatic/quasi-adiabatic conditions cause significant rise in local temperature making it conducive for ASBs to form.

Oussouaddi and Klepaczko [42]and Rusinek et al. [43] demonstrated from numerical simulations that adiabatic conditions can be assumed for copper, aluminium and steel when the strain rate exceeds 10^2 s^{-1} and the critical strain rate decreases with increase in specimen length.

2.4.2 Softening mechanisms triggering the ASB formation

A criterion for the incipience of the ASB based on the physics of the mechanism is essential. In the literature, several arbitrary ASB incipience criteria have been postulated for example based on critical strain, see Zhou et al. [44], strain rate, see Bonnet-Lebouvier et al. [13], temperature rise, see Teng et al. [14], and energy, see Dolinski et al. [45]. Although the above mentioned engineering oriented criteria are easy to implement, they strongly depend on the geometry and loading conditions. Hence there is a need for a robust physics based criterion consistent with the constitutive equations. Such a criterion may be obtained from the linear perturbation analysis, see e.g. Anand et al. [46]. Longère et al. [15] developed a criterion as shown in (2.51) based on simplified analysis of material instability accounting for the competition between hardening and softening mechanisms using the linear perturbation method. A detailed account of this approach can be consulted in the references - Molinari [47], Longère et al. [15], Longère and Dragon [48].

$$\mathrm{J}\left(\tau_{ij}, r, \dot{\kappa}; \frac{\partial r}{\partial \kappa}, \frac{\partial r}{\partial T}\right) = \sqrt{3}\tau - \left(r - \frac{1}{n} Y \dot{\kappa}^{\frac{1}{n}} + \rho_0 c_0 \left(\frac{\partial r}{\partial \kappa} / \left(-\frac{\partial r}{\partial T}\right)\right)\right) \geq 0 \qquad (2.51)$$

where $Y\dot{\kappa}^{1/n}$ represents the strain rate-induced overstress, $\partial r / \partial \kappa$ the strain hardening and $\partial r / \partial T$ the thermal softening effects. The deterioration process is actually assumed to run as soon as $\mathrm{J} = 0$.

This criterion allows for determining G_{ASB} (= $\mathbf{G} : \mathbf{N}$ at the instant of ASB incipience).

Two softening mechanisms triggering the ASB formation are considered in the present study, viz. thermal softening and dynamic recrystallization.

2.4.2.1 Thermal softening

Thermal softening along with quasi-adiabatic condition plays an important role in provoking the ASB onset. The form of the thermal softening function can be adapted to different materials as shown in (2.29) and (2.30). It is therefore essential to accurately calculate the regular temperature rise causing the thermal softening. The plasticity induced regular temperature rise shown in (2.49) can also be expressed as:

$$\rho c\dot{T} = \left(\frac{\sigma_{VM}^2}{\sigma_{eq}} - r \right)\dot{\kappa} \tag{2.52}$$

In most studies in the literature, the percentage of plastic work converted to heat i.e. the inelastic heat fraction β is assumed to be constant; for example $\beta = 0.6$ in [49], $\beta = 0.9$ in [50]. However the experiments by Mason et al [51] show that β is not a constant and varies with the strain, strain rate and temperature (se eg. [52],[53]) as is potentially the case in the present study. The form of the inelastic heat fraction can be deduced from (2.52) as:

$$\rho c\dot{T} = \beta \sigma_{VM} \dot{\kappa} \quad ; \quad \beta = \frac{\sigma_{VM}}{\sigma_{eq}} - \frac{r}{\sigma_{VM}} \tag{2.53}$$

Before the onset of ASB, the equivalent stress is solely composed of Von Mises stress and therefore the above expression is reduced to:

$$\rho c\dot{T} = (\sigma_{VM} - r)\dot{\kappa} \quad ; \quad \beta = 1 - \frac{r}{\sigma_{VM}} \tag{2.54}$$

As r depends on strain and temperature and σ_{VM} accounts for strain, strain rate and temperature, β is expected to depend on strain, strain rate and temperature as well, see [54]. During the ASB process, the dissipation progressively concentrates within the bands. Correspondingly, the evolution of the regular temperature outside the bands diminishes and finally saturates.

2.4.2.2 Dynamic recrystallization

It has been shown that the microstructure also influences the ASB incipience, see eg. Liu et al. [29]. The micro-mechanisms contributing to the regular material softening and influencing the ASB onset, which are taken into consideration in the present study, are the dynamic recovery (DRC) and dynamic recrystallization (DRX). Many studies have shown that the DRX occurs as a consequence of the adiabatic shear banding ([55],[56],[57]). Contrarily, for certain alloys such as those of titanium, DRX is shown to contribute significantly to the softening leading to the formation of ASB (see [58],[59]). The latter approach is considered in the present work and the competition between the DRX softening and thermal softening provoking the ASB initiation is studied. The detailed development of the DRX related model can be found in the article by Longère [31].

For the initial study on DRX, a critical value of the isotropic hardening variable κ_c is imposed to initiate occurrence of DRX. According to Mohamed and Bacroix [60], the stored energy at DRX onset should depend on temperature. But in the present study, for simplification, κ_c is maintained constant and temperature independent.

The DRC and DRX induce a negative hardening effect (softening) and it is modelled in the hardening term $h'(\kappa)$ as shown in (2.55).

$$h'(\kappa) = \tau_s\left(\bar{Y}(\kappa)\right)\left[1 - \exp\left(-\frac{\bar{Y}(\kappa)}{2}\kappa\right)\right] \tag{2.55}$$

τ_s is DRC and DRX dependent the saturation value of hardening stress. $\bar{Y}(\kappa)$ is a non-dimensional quantity phenomenologically composed of DRC and DRX components expressed below.

$$\bar{Y}(\kappa) = \bar{Y}_{DRC} + \bar{Y}_{DRX}(\kappa); \qquad \tau_s\left(\bar{Y}(\kappa)\right) = \frac{\eta}{\bar{Y}(\kappa)} \tag{2.56}$$

where

$$\begin{cases} \bar{Y}_{DRC} = \bar{Y}_0 \\ \bar{Y}_{DRX} = \bar{Y}_{\max}\left[1 - \exp\left(-\dfrac{\langle \kappa - \kappa_c \rangle}{\Delta\kappa_r}\right)\right] \end{cases} \tag{2.57}$$

η and $\Delta\kappa_r$ are kinetics related constants. $\bar{Y}_{DRC} = \bar{Y}_0$ is considered a constant. $\bar{Y}_{\max}$ represents the saturation value of the quantity $\bar{Y}_{DRX}$. The influence of the DRX on the material strain hardening is shown for example using $\Delta\kappa_r$ in Fig. 2.22. The lower the value of $\Delta\kappa_r$, the steeper the drop in strain hardening.

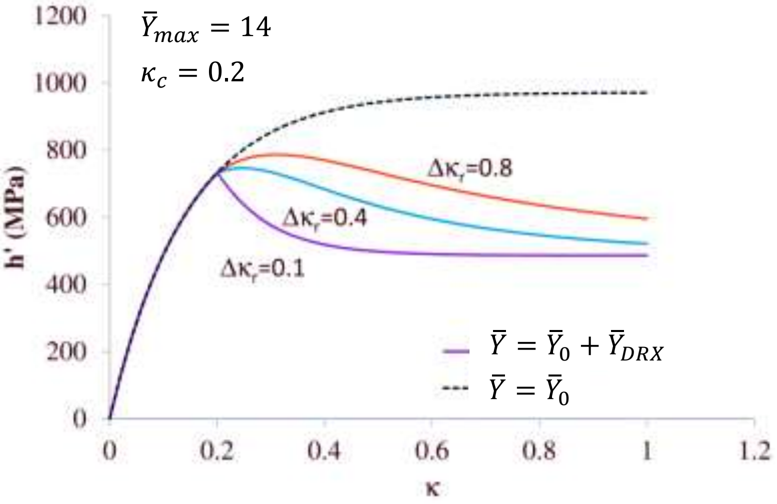

Fig. 2.22 After [31]. Influence of DRC-DRX related constants on strain hardening.

2.4.3 Mechanisms triggering the MV formation

The micro-voiding triggered during the loading and after unloading are distinguished here.

- During loading

Micro-voids can nucleate during the ductile damage process in several ways. The voids primarily nucleate around inclusions [61] and also at the grain boundary triple points [62] in the material. The void nucleation may be triggered by the particle-matrix interface decohesion, the particle rupture or micro-cracking of the matrix around the particle [63].

- After unloading

As mentioned in section 2.2.1.2, the phase transformation due to quenching of the ASB after unloading provokes the formation of micro-crack at the ASB/matrix interface. The question arises whether the micro-cracks observed by Peirs et al. [1] within the ASB are formed during or after the loading.

The case treated in the current work is effect of MV during the characteristic loading time.

From a modelling point of view, Chu and Needleman [64]proposed a void nucleation rate which is statistically distributed over the inelastic strain rate in a Gaussian form as depicted in (2.58) and Fig. 2.23. The statistical void nucleation function A_n is governed by three parameters: f_N the maximum void volume fraction possible to nucleate, ε_N the plastic strain value at which the void nucleation rate is maximum, and S_N the standard deviation of the distribution.

$$A_n = \frac{f_N}{S_N\sqrt{2\pi}} \exp\left[-\frac{1}{2}\left(\frac{\kappa - \varepsilon_N}{S_N} \right)^2 \right] \tag{2.58}$$

The shortcoming of this type of void nucleation rate is that it is non-nil even for very small strains and is independent of the loading path.

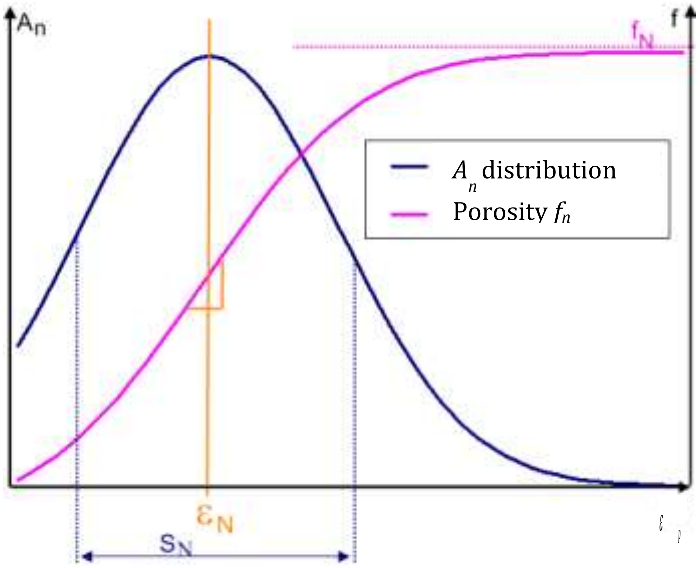

Fig. 2.23 After [65]. Void nucleation function A_n and porosity f_n as a function of accumulated plastic strain.

In another approach, Longère et al [61] devised a latent hole nucleation function overcoming the non-conformity of the former model to small strain and allowing for taking the loading path into account. The plastic strain at hole nucleation as a function of the stress triaxiality for different temperatures is shown in Fig. 2.24a. In Fig. 2.24b, void nucleation domain is given by Φ_{I_0} ; $\Phi_0(0)$ and $\Phi_0(\kappa)$ represent the initial and current elastic domain of the sound material respectively. Different loading paths (LP) involving different stress triaxiality is depicted which lead to void nucleation at different amounts of plastic strain (LP2 and LP3 in Fig.3.25b) and even without plastic strain when the stress triaxiality is high enough (LP1 in Fig.3.25b).

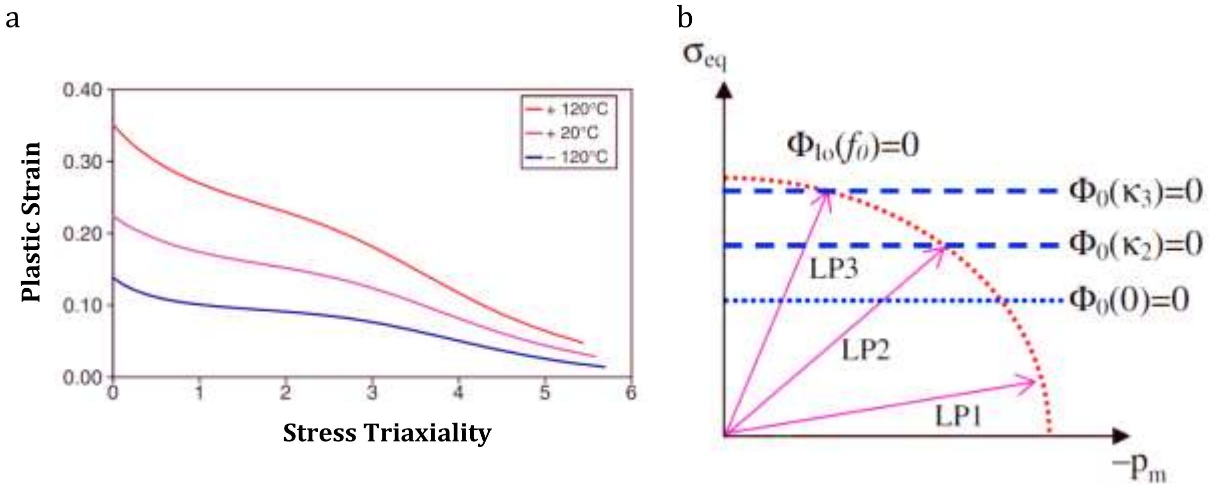

Fig. 2.24 After [61] a) Plastic strain at hole nucleation vs. stress triaxiality b) Illustration of various loading paths on the map of initial and current elastic domains and the void nucleation locus.

In absence of further analytical tools or experimental data, the micro-voiding is tentatively assumed to initiate as soon as the ΔG_{ASB} reaches a transition-to-voiding/critical level ΔG_{ASB}^{crit} such that $G_{MV} = \mathrm{Tr}\left(\mathbf{GN}\right)_{MV} = G_{ASB} + \Delta G_{ASB}^{crit}$. The ΔG_{ASB}^{crit} is calculated as $\Delta G_{ASB}^{crit} = (\Omega - 1) * G_{ASB}$ where Ω is an arbitrary constant greater than unity. After the MV initiation, ΔG_{ASB} is maintained constant at the value of ΔG_{ASB}^{crit} while ΔG_{MV} evolves taking the predominance as the degradation driving force.

2.5 NUMERICAL IMPLEMENTATION

The model in itself does not show the ASB and MV as entities in the finite elements but phenomenologically reproduces their consequences in the elements.

2.5.1 Numerical issues

Dealing numerically with this local softening phenomenon, resulting from a competition between material hardening and softening mechanisms and which has severe irreversible consequences at the structural level, still remains a challenging task. Indeed, the aim is to control the evolution of this material instability all along its progress and accordingly overcome the numerical instability the finite element computation code is subject to in the softening regime and subsequent meshing dependence of the numerical results.

Explicit time integration schemes are considered for both the initial-boundary value problem and rate equations of the constitutive model. In other words, the finite element computation code, namely LS-DYNA, is explicit and the rate equations are integrated within a user material subroutine according to an explicit time integration scheme.

2.5.1.1 Regularization and mesh dependence

The viscosity (rate dependency of both plasticity and degradation mechanisms) contributes to regularize the boundary value problem in the softening regime. Yet, as the ASB induces a very strong local softening, additional measures need to be applied to overcome the numerical instability. For this purpose, an adaptive time sub-increment procedure is imposed on the concerned elements as explained later.

Due to the usage of large scale postulate in the model, an a priori knowledge of the shear band path and hence mesh refining in the selected regions is not required. A study on the influence of the mesh size of the initial model describing the effect of ASB was carried out by Longère et al. [16]and [4]. The large scale postulate requires the ASB to be embedded within the finite element which in turn implies that it is not feasible to use mesh of any given size. It was shown that a mesh size of approximately five times the shear band (~500µm for high strength steel) width satisfies the scale postulate. A very coarse meshing would give rise to a dispersed area of deteriorated finite elements.

2.5.1.2 Sampling of the time increment

The ASB being a strong softening localisation requires additional measure to be applied in order to avoid numerical instability. For this purpose, the local integration time step in the concerned elements is reduced by following an adaptive time sub-increment procedure. A maximum strain increment principle is used (see [66],[16]) where the adaptive time sub-increment $\Delta\bar{t}$ is defined by the ratio of numerically admissible strain increment $\Delta\bar{e}$ determined numerically and the current strain rate $\dot{\bar{e}}$.

$$\begin{aligned} \Delta\bar{t} &= \frac{\Delta\bar{e}}{\dot{\bar{e}}} \\ \dot{\bar{e}} &= \sqrt{\frac{2}{3} d_{ij} d_{ji}} \end{aligned} \tag{2.59}$$

After the incipience of ASB, an adaptive time sub-increment of $\Delta\bar{t}\,/\,2$ is used to reinforce the numerical stability. As long as the current time step Δt fixed by the explicit computation code according to Courant-Friedrichs-Lewy (CFL) stability condition is less than $\Delta\bar{t}$, it is maintained the same. Once the Δt exceeds $\Delta\bar{t}$ (or $\Delta\bar{t}\,/\,2$ after the ASB incipience), an optimized integration time integration $\Delta\bar{t}_{opt}$ is used which is given by:

$$\Delta\bar{t}_{opt} = \frac{\Delta t}{N} \quad with \begin{cases} N = 1 & if\ \Delta t \leq \Delta\bar{t} \\ N = Int\left(\dfrac{\Delta t}{\Delta\bar{t}}\right) + 1 & if\ \Delta t > \Delta\bar{t} \end{cases} \tag{2.60}$$

It is to be noted that this procedure applies only to the concerned elements and therefore does not greatly affect the calculation cost.

2.5.1.3 Band orientation

According to experimental observations, the ASB is oriented in the plane of the maximum shear stress within the finite element. This requires the information of the principal stress values. With the knowledge of the plane of maximum shear stress, the resolved shear stress τ_{res} can be calculated which is then injected into the expression of ASB incipience criteria and yield function/plastic potential.

2.5.1.4 Stress triaxiality

The ASBs are formed and propagate under conditions of negative or zero stress triaxiality. Accordingly, in the user material subroutine, an external condition is imposed such that the incipience of ASB and the evolution of $\overset{\nabla}{D}^{ASB}$ take place only under positive or nil pressure.

On the other hand, different arguments have been proposed in the literature regarding the stress triaxiality conditions for the formation and growth of micro-voids. Bao and Wierzbicki [67] stated the micro-voids occur only under positive stress triaxiality and they transform into micro-shear decohesion under an asymptote of -1/3 negative stress triaxiality. However, Longère et al. [27] demonstrated that the micro-voids could initiate and grow around inclusions in the material even under shear pressure loading. The latter view point is adopted herein and hence in the user material subroutine, the MV mechanism is allowed to operate both under negative and positive pressure conditions. The MV expansion is also minimally active in the negative stress triaxiality condition, thanks to its exponential dependence on the mean stress whose form is adopted from Rousselier [36] which itself is derived from Rice and Tracey [40].

2.5.1.5 Crack formation

A material failure criterion is required in order to numerically process the element deletion. A theoretical upper bound for $\mathcal{D}$ from (2.2) exists considering melting point of the material as the maximum temperature limit which is explained in [15]. The crude theoretical approximation for critical deterioration intensity $\mathcal{D}_c = \mu / b$ is shown in (2.27).

Numerically implementing the $\mathcal{D}_c$ as a threshold for element failure is not feasible as the elements would undergo excessive distortion (even though LS-DYNA is able to deal with large distortion) at such high values of $\mathcal{D}$. Therefore currently an upper limit for $Tr\mathbf{D}$ is imposed in the user subroutine as a criterion for element deletion. It is to be noted that the numerical simulation of the crack propagation still remains a challenge and it could be dealt with X-FEM in the future, see for example Wolf et al. [68]

2.5.2 ASB+MV model implementation on RVE scale

The coupled ASB and micro-voiding (ASB+MV)-model is numerically implemented as a user material in the engineering finite element explicit computational code LS-DYNA. The first implementation is done on a 3D RVE i.e. a single *H*-length (3D, 8 nodes, reduced integration) brick finite element which is clamped on the bottom 4 nodes while the top 4 nodes are subjected to a tangent velocity *V* leading to simple shear loading. The shear strain Γ is defined as $\Gamma = \int \dot{\Gamma} dt$ where $\dot{\Gamma} = V / H$ and this shear configuration yields a horizontal ASB plane. A qualitative analysis of the enriched model is done in order to study the respective and combined contributions to the material response of the two degradation mechanisms at stake, namely adiabatic shear banding and micro-voiding.

Two cases are studying in the following corresponding to two typical materials susceptible to ASB: high strength steel for which the ASB onset is controlled by thermal softening and high strength titanium alloy for which there is a competition between/combination of thermal softening and DRX for the ASB initiation.

2.5.2.1 High strength steel: Thermal softening-controlled ASB onset

The material under consideration is high strength 30 Ni-Cr-Mo 6-6 steel. The constants pertaining to plasticity and hardening are obtained from [4]. The constants related to the ASB and MV induced softening are assigned arbitrary values in the current performance study.

Table 2.5 Material properties for 30 Ni-Cr-Mo 6-6 steel

Elastic - viscoplastic constants:

ρ_0 (kg/m^3)	c_0 (J/kg.K)	E (MPa)	ν	R_∞ (MPa)	R_{int} (MPa)	Y (MPa. s$^{1/n}$)	n
7800	420	200e+3	0.33	400	920	60	6

Thermal properties:

k	υ (°C^{-1})	T_0 (°C)	$\bar{\alpha}$ (/K)	$\dot{\varepsilon}_{crit}$ (/s)
10	1.1e-3	20	1e-6	100

ASB related constants:

Z (MPa. s$^{1/n}$)	m	η_{ASB} (MPa^{-2})	χ_1	χ_2	a (MPa)	b (MPa)
15	2	0.01	0.04	0.04	0	15e+3

MV related constants:

W (MPa. s$^{1/n}$)	q	η_{MV} (MPa^{-2})	ξ	Ω
20	2	0.08	1	1.5

Fig. 2.25 shows the shear stress – shear strain plot for 3 different cases. Case 1 is the material model exhibiting only polycrystalline plasticity (no shear localization) and hence only smooth thermal softening is seen without brutal drop in stress. Case 2 is the material with ASB induced degradation. Case 3 is the enriched model with ASB and MV induced material degradation. The MV incipience and growth induces a delayed supplementary material softening leading to a more abrupt drop in strength, as expected. The drop in stress is attenuated by the viscosity of both ASB and MV. In other words, increasing the velocity, results in a less brutal drop in stress with a smoother slope. The inertial effects which are known to play an important role during void growth, see e.g. Jacques et al. [69], are not explicitly accounted for in the present model, but their regularizing consequences are at least partly reproduced thanks to the viscous feature of the MV process.

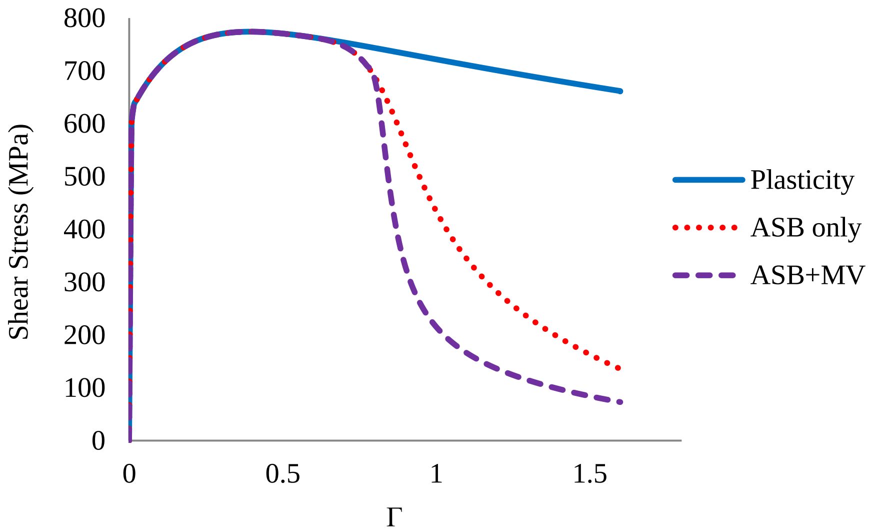

Fig. 2.25 Shear stress vs Shear strain for different cases. Case 1: polycrystalline plasticity only. Case 2: polycrystalline plasticity + ASB. Case 3: polycrystalline plasticity + ASB + MV

The constants pertaining to the MV in Table 2.5 are chosen in such a way so as to magnify its effect on the material and kinematics for the sole purpose of visualization. The MV related constants can be assigned different values to get the desired material behaviour. In Fig. 2.26, different sets of MV related constants are used to demonstrate the capacity of the model to reproduce different forms of MV induced drop in strength of the material. The stress-strain behaviour using the constants in Table 2.5 is shown in Fig. 2.26a. In this case, an early MV onset is seen and the MV influences a major part of the drop in strength. The MV incipience is delayed in Fig. 2.26b and Fig. 2.26c by means of the constant Ω. The magnitude of the MV influence is controlled by the constants W,q and η_{MV}. Fig. 2.26a,b use MV constants which reproduces a more severe drop in strength whereas Fig. 2.26c uses constants to show a gentle drop in strength due to MV.

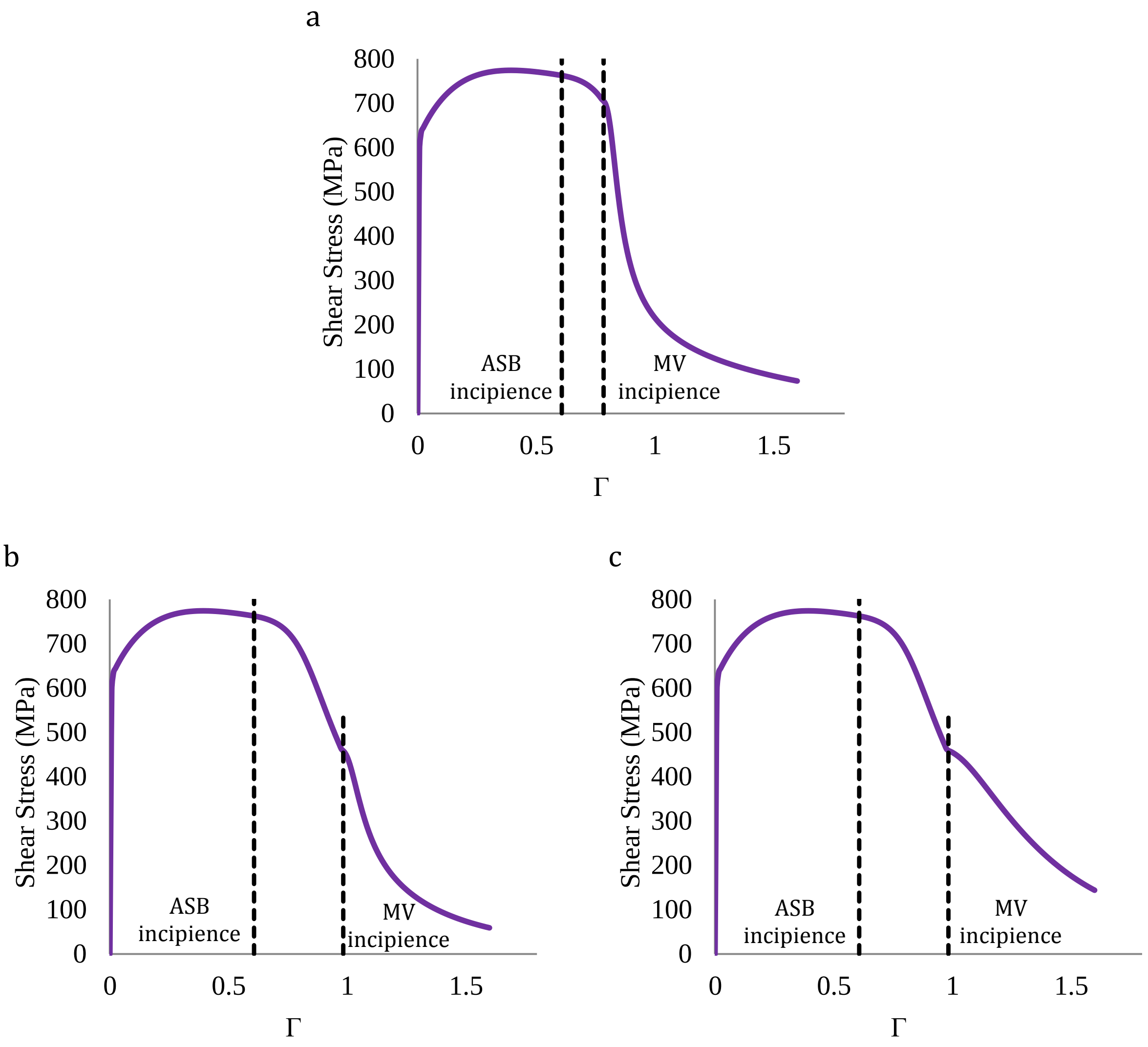

Fig. 2.26 Comparison of plots corresponding to different MV onset value and MV constants. Shear Stress vs Shear Strain with MV constants as a) $\Omega=1.5,\ W=20,\ \eta_{MV}=0.08$ b) $\Omega=2.8,\ W=20,\ \eta_{MV}=0.08$ c) $\Omega=2.8,\ W=25,\ \eta_{MV}=0.01$.

In the following (Fig. 2.27-Fig. 2.29), constants from Table 2.5 are used. The quantity $G=\tilde{\mathbf{G}}:\mathbf{N}$ containing the damage driving force is plotted against the shear strain for Cases 2 and 3 in Fig. 2.27a. An additional contribution of the void-growth is seen once the MV initiates in the case ASB+MV. The progression of ΔG for the case ASB+MV is shown in Fig. 2.27b. Once the ΔG_{ASB} attains the critical value ΔG_{ASB}^{crit}, it remains constant and simultaneously the ΔG_{MV} initiates and grows.

The fact that ΔG_{ASB} is non zero when MV operates allows the ASB-related process to operate until vanishing. In other words, MV becomes progressively and not suddenly predominant, as shown later.

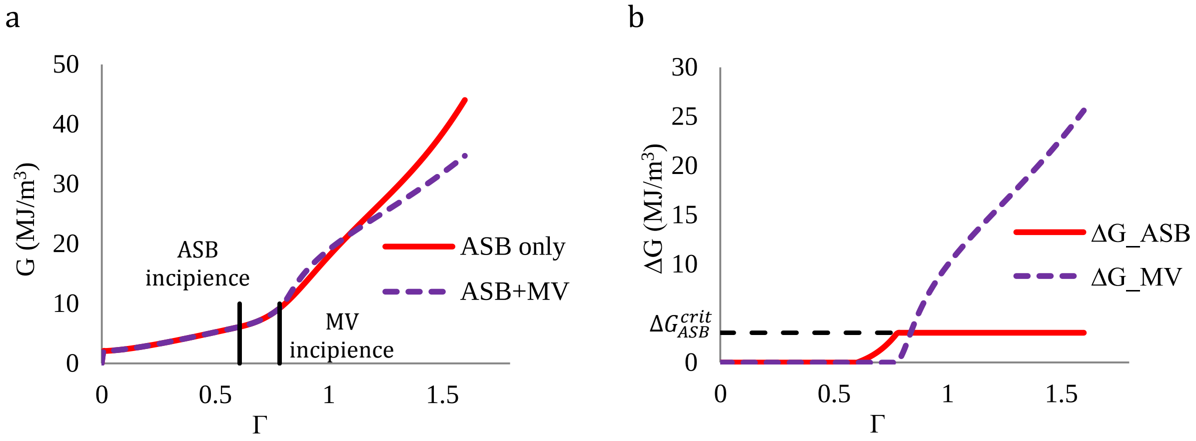

Fig. 2.27 (a) **G:N** for the cases: ASB only and ASB+MV ; (b) ΔG for the case ASB+MV showing the two components

For the enriched (ASB+MV)-model, the total inelastic strain rate d_{12}^{in} and its various components vs the shear strain are shown in Fig. 2.28. The "regular" plastic or the polycrystalline plastic strain rate is predominant in the initial stages. The contribution of the damage mechanisms termed as "singular" plastic strain rate becomes prevalent in the later stages. The singular strain rate is initially composed of the ASB induced strain rate $d_{ij}^{in(ASB)}$ and later by the MV induced strain rate $d_{ij}^{in(MV)}$.

Likewise the evolution of the total damage rate $Tr(\overset{\nabla}{\mathbf{D}}^{ASB+MV})$ with the shear strain and its two components are shown in Fig. 2.29a. Finally, Fig. 2.29b presents the trace of the damage rate tensor for the Cases 2 and 3. The significant addition to the Tr**D** for the case ASB+MV due to the void-growth is clearly seen.

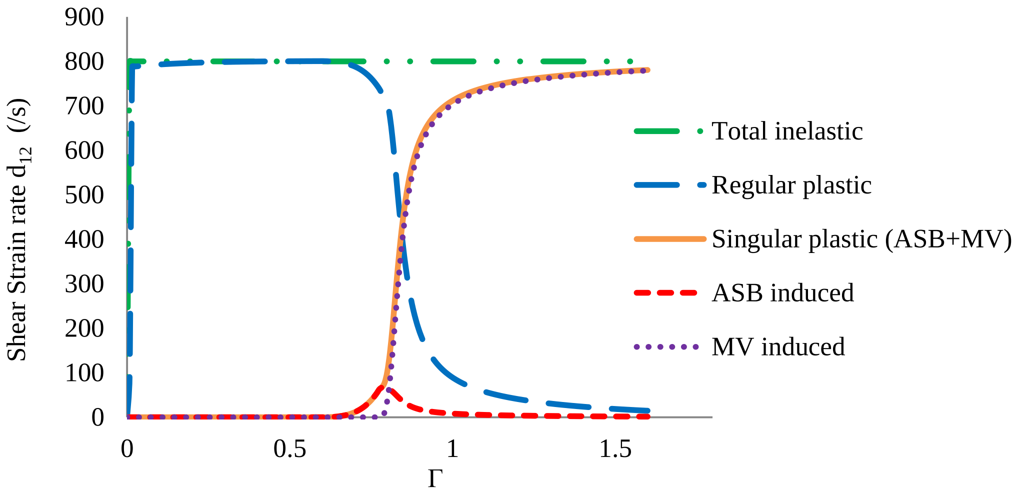

Fig. 2.28 Case ASB+MV: Inelastic strain rate with its components

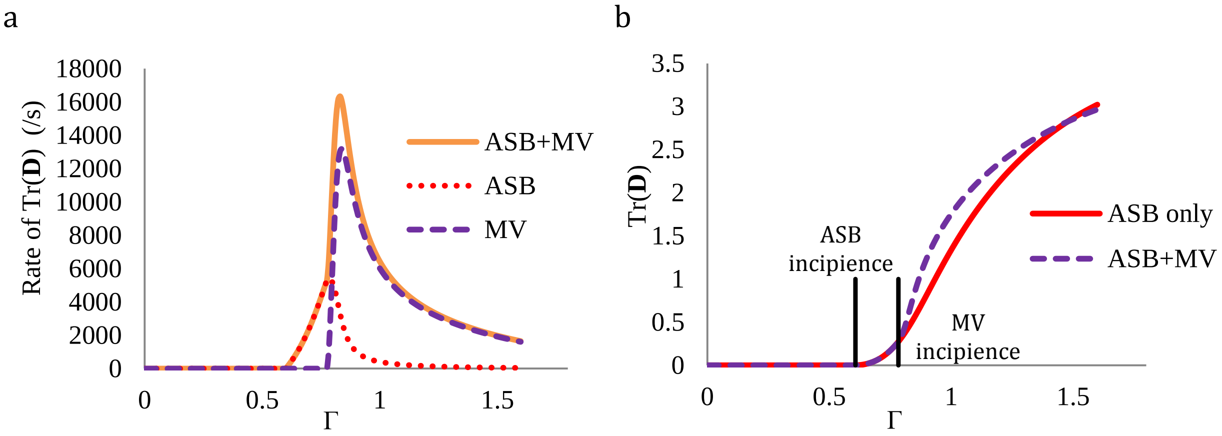

Fig. 2.29 (a) Case ASB+MV: Damage rate with its components; (b) TrD for the cases: ASB only and ASB+MV

2.5.2.2 *High strength titanium alloy: Influence of dynamic recrystallization*

The DRX mechanism is predominantly found to occur in Ti-6Al-4V as a potential cause of softening leading to the formation of ASBs [58]. In this section the enriched ASB+MV constitutive model containing DRX aspects is implemented on the RVE scale i.e. a single brick finite element for the Ti6Al4V alloy. The material properties concerning viscoplasticity and the thermal properties are obtained from experimental results as observed in [31]. The ASB, MV and DRX constants are assigned arbitrary values for the current parametric study.

Table 2.6 Material properties for Ti-6Al-4V

Elastic - viscoplastic constants:

ρ_0 (kg/m^3)	c_0 (J/kg.K)	E (MPa)	ν	R_∞ (MPa)	R_{int} (MPa)	Y (MPa. s$^{1/n}$)	n
4500	460	113e+3	0.34	972	1080	400	44

Thermal properties:

T_0 (°C)	$\bar{\alpha}$ (/K)	T_{ref} (K)	t	$\dot{\varepsilon}_{crit}$ (/s)
20	1e-6	923	0.6	100

ASB related constants:

Z (MPa. s$^{1/n}$)	m	η_{ASB} (MPa^{-2})	χ_1	χ_2	a (MPa)	b (MPa)
100	2	0.01	0.04	0.04	0	15e+3

MV related constants:

W (MPa. s$^{1/n}$)	q	η_{MV} (MPa^{-2})	ξ	Ω
75	2	0.05	1	2

DRX related constants:

$\bar{Y}_0$	$\bar{Y}_{\max}$	κ_c	$\Delta\kappa_r$	η (MPa)
14	14	0.2	0.8	1.36e+4

In line of the work by [31] dealing with ASB only, the competitive influence of the two softening mechanisms provoking the formation of the ASB, namely thermal softening and DRX induced softening, and their effects on MV are studied here. Four different cases are numerically studied here :

(1) no thermal softening and no DRX (No TS & No DRX)
(2) no thermal softening and with DRX (No TS & With DRX)
(3) with thermal softening and no DRX (With TS & No DRX)
(4) with thermal softening and with DRX (With TS & With DRX)

The DRX related constants are chosen such that the ASB incipience and consequently the start of the drop in strength take place almost at the same time for cases (2) and (3). Fig. 2.30 shows the plot of shear stress vs shear strain for the four different cases. For the first case, when no softening mechanism comes into play, no material degradation takes place as expected. The ASB incipience instant is marked by a red spot and MV incipience by a green one on the curves. It is seen that as calibrated, the ASB incipience takes place more or less simultaneously for cases (2) and (3) i.e. cases incorporating thermal softening only or DRX softening only. When both the softening mechanisms act in case (4), it is seen that the ASB onset takes place much earlier. The MV onset on the other hand is not directly influenced by the softening mechanisms but it depends on the value of G_{ASB} according to the current model.

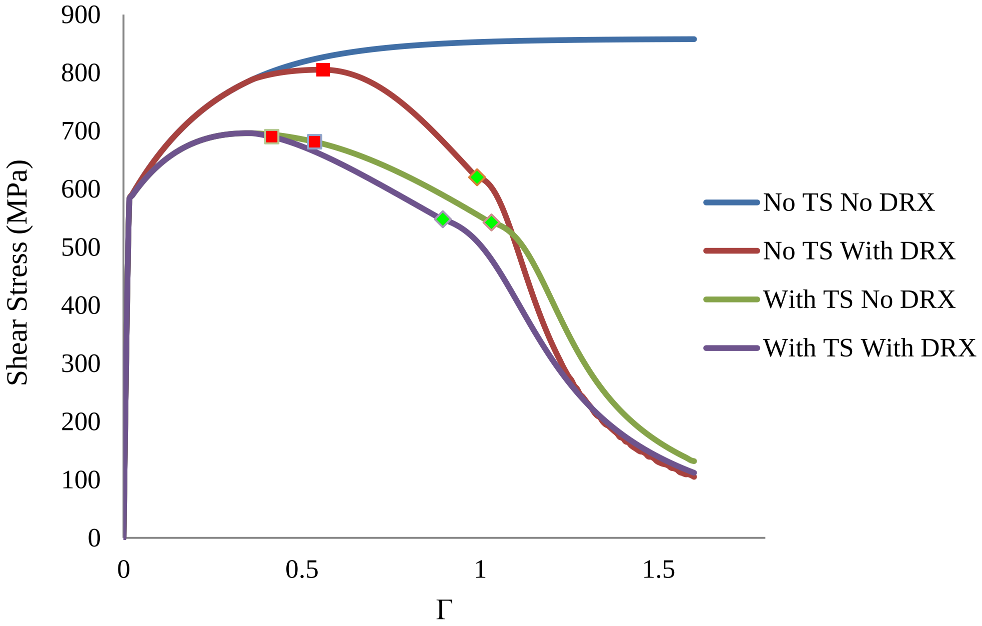

Fig. 2.30 Shear stress vs shear strain for different cases of thermal softening and DRX induced softning.

2.6 CONCLUSION

The formation and propagation of adiabatic shear bands (ASB) is a very complex mechanism. A physics motivated phenomenological model describing the ASB induced degradation and kinematics in the framework of large scale postulate was initially developed by Longère et al. [15]. This model required enrichment in terms of taking into account the micro-mechanisms that operate in the late pre-failure stage. Experimental evidence showed the presence of micro-voiding (MV) in the wake of the ASB. Hence, the existing ASB constitutive model was conceptually enriched to comprise the additional void-growth induced degradation [24].

This enlarged ASB+MV model is revisited in accordance with the physics of the shear localization and subsequent ductile damage process. The present enlarged model is numerically implemented here and has been demonstrated to be numerically feasible at the representative volume element scale. The qualitative analysis on the RVE shows the desired behaviour with the supplementary void-growth contribution.

In the current model, arbitrary ASB and MV deterioration related constants have been employed so as to observe its numerical feasibility and qualitative response. The challenge remains to experimentally identify the instance of MV onset and hence the related constants.

The current model tentatively assumes identical orientation for both the ASB and MV. It has been shown by Peirs et al. [1] that the micro-cracks within the ASB are oriented in a direction different from that of the ASB. This scenario has to be taken into account in future works by using different orientation tensors for ASB and MV which may pose other issues on objective derivatives (spin to be considered). The phase transformation of the ASB and the corresponding change in singular material properties with time could be considered as well.

Finally, the numerical simulation of the crack propagation still remains a challenge and it could be dealt with enriched FEM, e.g. X-FEM or E-FEM, see [18] and [19] respectively.

2.7 REFERENCES

[1] J. Peirs, W. Tirry, B. Amin-Ahmadi, F. Coghe, P. Verleysen, L. Rabet, D. Schryvers, J. Degrieck "Microstructure of adiabatic shear bands in Ti6Al4V," *Materials Characterization*, vol. 75. 2013.

[2] Q. Xue, M. A. Meyers, and V. F. Nesterenko, "Self-organization of shear bands in titanium and Ti-6Al-4V alloy," *Acta Mater.*, vol. 50, no. 3, pp. 575–596, 2002.

[3] D.-G. Lee, Y. H. Lee, S. Lee, C. S. Lee, and S.-M. Hur, "Dynamic deformation behavior and ballistic impact properties of Ti6Al4V alloy having equiaxed and bimodal microstructures," *Met. Mater. Trans. A*, vol. 35 A, no. October, pp. 3103–3112, 2004.

[4] P. Longère, A. Dragon, and X. Deprince, "Numerical Study of Impact Penetration Shearing Employing Finite Strain Viscoplasticity Model Incorporating Adiabatic Shear Banding," *ASME, J. Eng. Mater. Technol.*, vol. 131, no. 1, p. 011105.1-011105.14, 2009.

[5] B. E. Schuster, J. P. Ligda, Z. L. Pan, and Q. Wei, "Nanocrystalline refractory metals for extreme condition applications," *JOM*, vol. 63, no. 12, pp. 27–31, 2011.

[6] W. S. Andrews, "Depleted Uranium on the battlefield," *Can. Mil. J.*, pp. 41–46.

[7] L. S. Magness Jr., "High strain rate deformation behaviors of kinetic energy penetrator materials during ballistic impact," *Mech. Mater.*, vol. 17, pp. 147–156, 1994.

[8] A. Molinari, C. Musquar, and G. Sutter, "Adiabatic shear banding in high speed machining of Ti – 6Al – 4V : experiments and modeling," *Int. J. Plast.*, vol. 18, pp. 443–459, 2002.

[9] G. G. Ye, S. F. Xue, M. Q. Jiang, X. H. Tong, and L. H. Dai, "Modeling periodic adiabatic shear band evolution during high speed machining Ti-6Al-4V alloy," *Int. J. Plast.*, vol. 40, pp. 39–55, 2013.

[10] Y. L. Bai and B. Dodd, *Adiabatic shear localization*. Pergamon Press, Oxford., 1992.

[11] A. Marchand and J. Duffy, "An experimental study of the formation process of adiabatic shear bands in a structural steel," *J. Mech. Phys. Solids*, vol. 36, no. 3, pp. 251–283, 1988.

[12] J. Peirs, P. Verleysen, J. Degrieck, and F. Coghe, “The use of hat-shaped specimens to study the high strain rate shear behaviour of Ti – 6Al – 4V,” *Int. J. Impact Eng.*, vol. 37, no. 6, pp. 703–714, 2010.

[13] A. Bonnet-Lebouvier, A. Molinari, and P. Lipinski, “Analysis of the dynamic propagation of adiabatic shear bands,” *Int. J. Solids Struct.*, vol. 39, no. 16, pp. 4249–4269, 2002.

[14] X. Teng, T. Wierzbicki, and H. Couque, “On the transition from adiabatic shear banding to fracture,” *Mech. Mater.*, vol. 39, no. 2, pp. 107–125, 2007.

[15] P. Longère, A. Dragon, H. Trumel, T. De Resseguier, X. Deprince, and E. Petitpas, “Modelling adiabatic shear banding via damage mechanics approach,” *Arch. Mech.*, vol. 55, no. 1, pp. 3–38, 2003.

[16] P. Longère, A. Dragon, H. Trumel, and X. Deprince, “Adiabatic shear banding-induced degradation in a thermo-elastic / viscoplastic material under dynamic loading,” *Int. J. Impact Eng.*, vol. 32, pp. 285–320, 2005.

[17] S. Su, L. Stainier, and S. Mercier, “Eergy-based variational modeling of fully formed adiabatic shear bands,” *Eur. J. Mech. / A Solids*, vol. 47, pp. 1–13, 2014.

[18] P. M. A. Areias and T. Belytschko, “Two-scale method for shear bands: Thermal effects and variable bandwidth,” *Int. J. Numer. Methods Eng.*, vol. 72, pp. 658–696, 2007.

[19] H. M. Mourad, C. A. Bronkhorst, V. Livescu, J. N. Plohr, and E. K. Cerreta, “Modeling and simulation framework for dynamic strain localization in elasto-viscoplastic metallic materials subject to large deformations,” *Int. J. Plast.*, vol. 88, pp. 1–26, 2017.

[20] P. Longère, “Adiabatic shear banding assisted dynamic failure: Some modeling issues,” *Mech. Mater.*, vol. 116, pp. 49–66, 2018.

[21] C. McVeigh, F. Vernerey, W. K. Liu, B. Moran, and G. Olson, “An interactive micro-void shear localization mechanism in high strength steels,” *J. Mech. Phys. Solids*, vol. 55, no. 2, pp. 225–244, 2007.

[22] A. G. Odeshi, S. Al-ameeri, S. Mirfakhraei, F. Yazdani, and M. N. Bassim, “Deformation and failure mechanism in AISI 4340 steel under ballistic impact,” *Theor. Appl. Fract. Mech.*, vol. 45, pp. 18–24, 2006.

[23] P. Longère and A. Dragon, “Dynamic vs . quasi-static shear failure of high strength metallic alloys : Experimental issues,” *Mech. Mater.*, vol. 80, pp. 203–218, 2015.

[24] P. Longere and A. Dragon, “Enlarged finite strain modelling incorporating adiabatic shear banding and post-localization microvoiding as shear failure mechanisms,” *Int. J. Damage Mech.*, pp. 1–28, 2016.

[25] H. L. Dorothy, P. Longère, and A. Dragon, “Coupled ASB-and-microvoiding-assisted dynamic ductile failure,” *Procedia Eng.*, vol. 197, pp. 60–68, 2017.

[26] C. Zener and J. H. Hollomon, “Effect of Strain Rate Upon Plastic Flow of Steel,” *J. Appl. Phys.*, no. 15, pp. 22–32, 1944.

[27] P. Longère, S. Bhogaraju, and D. Craciun, “Void collapse/growth in solid materials under overall shear loading,” *Mech. Res. Commun.*, vol. 69, pp. 1–7, 2015.

[28] E. Roux, P. Longère, O. Cherrier, T. Millot, D. Capdeville, and J. Petit, "Analysis of ASB assisted failure in a high strength steel under high loading rate," *Mater. Des.*, vol. 75, pp. 149–159, 2015.

[29] X. Liu, C. Tan, J. Zhang, Y. Hu, H. Ma, F. Wang, H. Cai, "Influence of microstructure and strain rate on adiabatic shearing behavior in Ti-6Al-4V alloys," *Mater. Sci. Eng. A*, vol. 501, no. 1–2, pp. 30–36, 2009.

[30] L. M. Kachanov, "On the Time to Rupture under Creep Conditions," *Izv. Acad. Nauk SSSR, OTN*, vol. 8, pp. 26–31, 1958.

[31] P. Longère, "Respective/combined roles of thermal softening and dynamic recrystallization in adiabatic shear banding initiation," *Mech. Mater.*, vol. 117, pp. 81–90, 2018.

[32] S. P. Timothy, "The structure of adiabatic shear bands in metals: A critical review," *Acta Metall.*, vol. 35, no. 2, pp. 301–306, 1987.

[33] K. A. Hartley, J. Duffy, and R. H. Hawley, "Measurement of the Temperature Profile During Shear Band Formation in Steels Deforming At High-Strain Rates," *J. Mech. Phys. Solids*, vol. 35, no. 3, pp. 283–301, 1987.

[34] D. Halm and A. Dragon, "A Model of Anisotropic Damage by Mesocrack Growth; Unilateral Effect," *Int. J. Damage Mech.*, vol. 5, pp. 384–402, 1996.

[35] J. Lemaitre, "A Continuous Damage Mechanics Model for Ductile Fracture," *J. Eng. Mater. Technol.*, vol. 107, pp. 83–89, 1985.

[36] G. Rousselier, "Ductile fracture models and their potential in local approach of fracture," *Nucl. Eng. Des.*, vol. 105, pp. 97–111, 1987.

[37] V. Tvergaard and A. Needleman, "Analysis of the Cup-Cone Fracture in a Round Tensile bar," *Acta Metall.*, vol. 32, no. 1, pp. 157–169, 1984.

[38] R. Becker, A. Needleman, O. Richmond, and V. Tvergaard, "Void Growth and Failure in Notched bars," *J. Mech. Phys. Solids*, vol. 36, no. 3, pp. 317–351, 1988.

[39] H. L. Dorothy, P. Longère, and A. Dragon, "Modelling of high strain rate failure under ASB and microvoiding," *Procedia Eng.*, vol. 173, pp. 593–600, 2017.

[40] J. R. Rice and D. M. Tracey, "On the ductile enlargement of voids in triaxial stress fields," *J. Mech. Phys. Solids*, vol. 17, pp. 201–217, 1969.

[41] P. Longère, "Some issues related to the modeling of dynamic shear localization-assisted failure," in *Dynamic Damage and Fragmentation*, O. Cazacu and E. Buzuard, Eds. ISTE-WILEY, to be published.

[42] O. Oussouaddi and J. R. Klepaczko, "Analyse de la transition entre des déformations isothermes et adiabatiques dans le cas de la torsion d'un tube," *J. Phys. IV Colloq.*, vol. 01, no. (C3), pp. C3-323-C3-330, 1991.

[43] A. Rusinek, S. P. Gadaj, W. K. Nowacki, and J. R. Klepaczko, "Simulation of heat exchange during simple shear of sheet steel," *J. Theor. Appl. Mech.*, vol. 40, no. 2, pp. 317–337, 2002.

[44] M. Zhou and G. Ravichandran, "Dynamically Propagating Shear Bands in Impact-Loaded Plates-II. Numerical Simulations," *J. Mech. Phys. Solids*, vol. 44, no. 6, 1996.

[45] M. Dolinski, D. Rittel, and A. Dorogoy, "Modeling adiabatic shear failure from

energy considerations," *J. Mech. Phys. Solids*, vol. 58, no. 11, pp. 1759–1775, 2010.

[46] L. Anand, K. H. Kim, and T. G. Shawk, "Onset of shear localization in viscoplastic solids," *J. Mech. Phys. Solids*, vol. 35, no. 4, pp. 407–429, 1987.

[47] A. Molinari, "Instabilité thermoviscoplastique en cisaillement simple," *J. mécanique théorique appliquée*, vol. 4, no. 5, pp. 659–684, 1985.

[48] P. Longère and A. Dragon, "Adiabatic Heat Evaluation For Dynamic Plastic Localization," *J. Theor. Appl. Mech.*, vol. 45, no. 2, pp. 203–223, 2007.

[49] S. Osovski, D. Rittel, and A. Venkert, "The respective influence of microstructural and thermal softening on adiabatic shear localization," *Mech. Mater.*, vol. 56, pp. 11–22, 2013.

[50] A. Needleman and V. Tvergaard, "Analysis of a brittle-ductile transition under dynamic shear loading," *Int. J. Solids Struct.*, vol. 32, no. 17–18, pp. 2571–2590, 1995.

[51] J. J. Mason, A. J. Rosakis, and G. Ravichandran, "On the strain and strain rate dependence of the fraction of plastic work converted to heat: an experimental study using high speed infrared detectors and the Kolsky bar," *Mech. Mater.*, vol. 17, no. 2–3, pp. 135–145, 1994.

[52] P. Longère and A. Dragon, "Evaluation of the inelastic heat fraction in the context of microstructure-supported dynamic plasticity modelling," *Int. J. Impact Eng.*, vol. 35, no. 9, pp. 992–999, 2008.

[53] P. Longère and A. Dragon, "Inelastic heat fraction evaluation for engineering problems involving dynamic plastic localization phenomena," *J. Mech. Mater. Struct.*, vol. 4, no. 2, pp. 319–349, 2009.

[54] L. Stainier and M. Ortiz, "Study and validation of a variational theory of thermo-mechanical coupling in finite visco-plasticity," *Int. J. Solids Struct.*, vol. 47, no. 5, pp. 705–715, 2010.

[55] M. Meyers, V. Nesterenko, J. LaSalvia, and Q. Xue, "Shear localization in dynamic deformation of materials: microstructural evolution and self-organization," *Mater. Sci. Eng. A*, vol. 317, no. 1, pp. 204–225, 2001.

[56] G. A. Li, L. Zhen, C. Lin, R. S. Gao, X. Tan, and C. Y. Xu, "Deformation localization and recrystallization in TC4 alloy under impact condition," *Mater. Sci. Eng. A*, vol. 395, pp. 98–101, 2005.

[57] B. Wang, J. Li, J. Sun, X. Wang, and Z. Liu, "Shear localization and its related microstructural evolution in the ultrafine grained titanium processed by multi-axial compression," *Mater. Sci. Eng. A*, vol. 612, pp. 227–235, 2014.

[58] D. Rittel, P. Landau, and A. Venkert, "Dynamic Recrystallization as a potential cause for adiabatic shear failure," *Phys. Rev. Lett.*, vol. 101, no. 165501, 2008.

[59] P. Landau, S. Osovski, A. Venkert, V. Gärtnerová, and D. Rittel, "The genesis of adiabatic shear bands," *Nature, Sci. Reports*, vol. 6: 37266, 2016.

[60] G. Mohamed and B. Bacroix, "Role of Stored Energy in Static Recrystallization of Cold Rolled Copper Single and Multicrystals," vol. 48, no. 13, pp. 3295–3302, 2000.

[61] P. Longere, A. G. Geffroy, B. Leble, and A. Dragon, "Modeling the Transition

between Dense Metal and Damaged (Microporous) Metal Viscoplasticity," *Int. J. Damage Mech.*, vol. 21, no. 7, pp. 1020–1063, 2012.

[62] S. H. Goods and L. M. Brown, "The Nucleation of Cavities by Plastic Deformation," *Acta Metall.*, vol. 27, no. 1, pp. 1–15, 1979.

[63] J. W. Hancock and A. C. Mackenzie, "HIGH-STRENGTH STEELS SUBJECTED TO MULTI-AXIAL mean stress," *j. Mech. Phys. Solids*, vol. 24, pp. 147–169, 1976.

[64] C. C. Chu and A. Needleman, "Void Nucleation Effects in Biaxially Stretched Sheets," *J. Eng. Mater. Technol.*, vol. 102, no. 3, pp. 249–256, 1980.

[65] A.-G. Geffroy, "Modélisation numérique de la rupture de structures navales sous l 'effet d 'explosions au contact," Université de Bretagne-Sud, 2010.

[66] M. Kulkarni, T. Belytschko, and A. Bayliss, "Stability and error analysis for time integrators applied to strain-softening materials," *Comput. Methods Appl. Mech. Eng.*, vol. 124, no. 4, pp. 335–363, 1995.

[67] Y. Bao and T. Wierzbicki, "On fracture locus in the equivalent strain and stress triaxiality space," *Int. J. Mech. Sci.*, vol. 46, no. 1, pp. 81–98, 2004.

[68] J. Wolf, P. Longère, J. M. Cadou, and J. P. Crété, "Numerical modeling of strain localization in engineering ductile materials combining cohesive models and X-FEM," *Int. J. Mech. Mater. Des.*, vol. 14, no. 2, pp. 177–193, 2018.

[69] N. Jacques, S. Mercier, and A. Molinari, "Effects of microscale inertia on dynamic ductile crack growth," *J. Mech. Phys. Solids*, vol. 60, no. 4, pp. 665–690, 2012.

3 APPLICATION TO INITIAL BOUNDARY VALUE PROBLEMS

ABSTRACT

The numerical implementation of the constitutive model developed to describe the ASB and MV induced material deterioration is carried out here. Firstly, the interest of employing the developed advanced constitutive model, tentatively considering the ASB contribution alone, termed as the '**D** type model' is demonstrated by comparison with an engineering oriented model termed as '(1-*D*) type model'. The (1-*D*) type model uses a scalar isotropic damage variable to describe the ASB assisted failure in contrast to the **D** type model which uses a second order tensor deterioration variable taking into account the anisotropy induced by the ASB. The performances of the two models are evaluated considering the dynamic shear loading of a hat shaped structure (HSS) within a complete calibration procedure. It is shown that the (1-*D*) type model considered is not able to satisfy the calibration procedure and that the ASB induced failure requires an advanced modelling as done in the **D** type model.

Secondly, the performance of the enriched model comprising the effects of adiabatic shear banding and micro-voiding mechanisms considering an initial-boundary value problem is evaluated. To that purpose, the model has been implemented as user material in the engineering finite element computation code LS-DYNA. Numerical simulation of the dynamic shearing of HSS is conducted and the interest of accounting for the pre-failure stage consisting of micro-voiding in the ASB wake is emphasized.

The enriched model is then sought to be implemented onto a more complex IBVP namely high speed machining (HSM). The HSM of alloys such as those of Ti6Al4V shows ASBs which contribute to the chip serration and reduction in load on the cutting tool. The limitations of conventional models used to simulate HSM in terms of their strong dependency on arbitrary constants are demonstrated by studying the influence of some parameters on the numerical results obtained from the simulation of the HSM process using a commercial finite element computation code, namely Abaqus.

CONTENTS

3.1 INTRODUCTION

The shear localization induced failure often occurs on high strain rate loaded structures in regions of low stress triaxiality. As stated in Chapter 1, the ASB+MV are found to occur either as useful or undesirable phenomena in various applications involving complex loading path such as failure of armour plates on ballistic impacts, self-sharpening of kinetic energy penetrators, high speed machining, etc. It is therefore essential to numerically test the developed ASB+MV model on a structural scale considering initial boundary value problems which is done in the current chapter.

For a constitutive model to be considered predictive, it has to satisfy a complete Verification and Validation (V&V) procedure which consists in numerically evaluating the performances of the model on initial boundary value problems (IBVP) with increasing complexity against corresponding experimental results. In the literature, the models describing ASB are widely calibrated and evaluated using a single IBVP. Indeed, the high strain rate loading of a hat shaped structure (HSS) is often used to this end, but this should not be considered as a sole evaluating configuration as the ASB orientation and path are entirely controlled by the specimen geometry and the predictability of the model cannot be sufficiently assessed.

In the (V&V) procedure, the model is first numerically implemented at the scale of a representative volume element (RVE) in order to determine the viscoplasticity and viscous deterioration related constants for a given material from simple experimental results such as those of standard tension/compression tests at various temperatures and strain rates along with high strain rate torsion or/and shear tests. This is the step of material constants **calibration**. The model performance is then evaluated and the constants are further adjusted if needed by considering an initial-boundary value problem (IBVP) for example using a structure, e.g. HSS [1] or Kalthoff and Winkler (KW) impact specimen ([2],[3]), as the ASB path in these structures is known a priori. The set of material constants is expected to satisfy the experimental results obtained from both the simple tests and the tests on the structures. This is the step of **verification**. The final challenging **validation** step is to test the model on a more complex structure where the shear band path is a priori unknown, for example, ballistic impact of a thick plate [1], high speed machining, etc.

In the first part of the chapter, in Section 3.2, the motivation for using the developed constitutive model to describe ASB assisted material failure is demonstrated by a comparative modelling and simulation. In both the approaches studied, the ASB is considered as a deterioration mechanism whose consequences in the material are described via an internal damage-like variable in the context of phenomenological modelling. The first approach comprising the use of a scalar internal variable D for describing the damage of materials has been widely used for decades for various applications with (1-D) representing the ratio of the remaining strength of the material. Here, the ability of the (1-D) type model to represent the ASB induced deterioration is evaluated considering a complete calibration procedure using the commercial finite element computation code Abaqus. The second approach examined is a physics motivated and an advanced model developed by Longère et al. [4] and implemented in the commercial finite element computation code LS-DYNA in which the ASB is considered as a form of anisotropic deterioration acting on both material properties and plastic flow. This anisotropic mechanical deterioration induced in the structural material by the bands is dealt with by using a 2nd order tensor internal variable **D**. The two models are tested following the V&V procedure. It is shown that the $(1-D)$ type model is not predictive and that the **D** type model is more adapted to describe the ASB induced deterioration.

The feasibility of the enriched constitutive model developed in the previous chapter distinguishing the adiabatic shear banding (ASB) and micro-voiding (MV) mechanisms on an IBVP is studied here employing the commercial finite element computation code LS-DYNA. Due to the challenge of obtaining material constants relative to the micro-voiding, rather than constants identification of the V&V procedure, a model feasibility study was conducted at the RVE scale in Chapter 2. Likewise here, the feasibility of the ASB+MV on a structural scale considering the dynamic shearing of the HSS is evaluated in Section 3.3. In addition, the interest of distinguishing the respective pre-failure contributions of ASB on one hand and MV on the other hand is evidenced: while the ASB may cross the whole structure, the MV may cover only a local area. Knowing that the material inside ASB zones may recover its initial properties after unloading – unless micro-crack form during this stage –, the structure may be damaged only locally, which constitutes information of utmost interest for the residual strength of the structure.

The numerical simulation of a complex IBVP using the ASB+MV model is foreseen in Section 3.4. High speed machining (HSM) implies high strain rate loading and hence favours the formation of adiabatic shear bands in high strength metallic materials such as titanium alloys. When formed, these shear bands play a role in chip serration in terms of chip morphology and reduce the load on the cutting tool. The present study aims at studying the influence of some parameters on the numerical results obtained from the simulation of the HSM process using the commercial finite element computation code Abaqus. The parameters in question include notably the level of the thermo-mechanical coupling, the method for evaluating the self-heating and the failure criterion. The limitations of usual models in terms of their strong dependency on arbitrary constants are discussed. The requirement for an advanced model which is able to describe the thermo-viscoplasticity, temperature rise consistent with the material state, controlled strain localization and the micro-mechanisms in operation is postulated.

3.2 MOTIVATION FOR AN ADVANCED MODEL

In this Section no distinction between ASB and MV is done. The term ASB in the following includes both mechanisms indistinctly.

The interest of using the advanced constitutive model developed in Chapter 2, which is presently termed as '**D** type model', is demonstrated here. In the current section, the models considered describe the ASB induced deterioration without distinguishing the micro-voiding contribution. The other simpler model considered for comparative study termed as '$(1-D)$ type model' is constructed below.

The concept of continuous damage mechanics (CDM) using $(1-D)$ type model was initially introduced by L. Kachanov [5] to describe the damage acceleration leading to creep rupture. Lemaître [6] then used it to describe the elastic properties' deterioration induced by ductile damage in the form of void growth in materials subjected to tension loading. Recently, for the purpose of engineering applications and to avoid the complexity of the constitutive models, Dolinski et al. [7] applied it to reproduce the material softening induced by ASB formation. This approach is considered in Section 3.2.1.

3.2.1 (1-D) type constitutive model

The approach dealt with in the following also assumes a large scale postulate in which the characteristic length of the representative volume element (RVE) is greater than the bandwidth of the ASB.

To characterize the deterioration of the material properties under loading conditions, an evolving scalar parameter $0 \le D \le 1$ is used. $D = 0$ corresponds to the undamaged state and $D = 1$ is the failed state of the material. D is a an isotropic parameter used to reduce the current strength of a material under loading. $(1-D)$ signifies the ratio of the remaining strength in the material.

An empirical energy based criterion for ASB evolution proposed by Dolinski et al. [7] is adopted here. They expressed the ASB deterioration kinetics as being governed by the rate of plastic strain energy density $\dot{W}_p$ as shown below where $\mathbf{d^p}$ is the plastic strain rate.

$$\dot{W}_p = \boldsymbol{\tau} : \mathbf{d^p} \tag{3.1}$$

According to the authors in [7], the ASB induced damage D evolution is given by (3.2), where W_{cr} is the critical value of plastic strain energy density at the ASB onset; and W_f the ultimate fracture energy density (see Fig. 3.1) – critical energy at ASB onset was already suggested by Mazeau et al. [8]. The quantities W_f and W_{cr} constitute an ASB related material constant A as shown below. In the context of the present work, the value of W_{cr} is deduced from the linear perturbation method as presented in Chapter 2, and accordingly may differ from a FE to another depending on the loading path whereas in Dolinski et al. [7] its value, which is obtained from experimental results, is unique whatever the FE and loading path.

$$D=\begin{cases}0 & if \quad W_p \le W_{cr} \\ A(W_p - W_{cr}) & else\end{cases} \quad ; \qquad A=\frac{1}{W_f - W_{cr}} \tag{3.2}$$

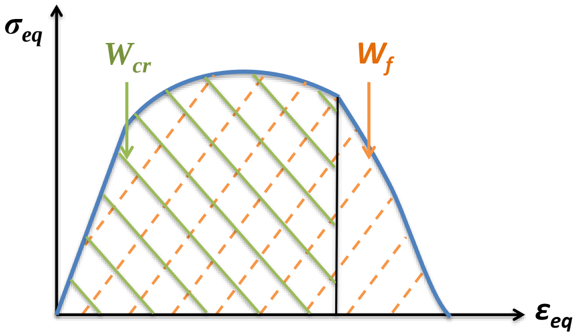

Fig. 3.1 Criterion for ASB induced failure according to Dolinski et al [7]. ASB initiates as soon as W_p reaches W_{cr} leading to drop in stress and the remaining energy in the post-critical stage is W_f-W_{cr}.

Constitutive equations integrating ASB-deterioration-like process in the $(1-D)$ type model are derived herein from thermodynamic potentials, namely the free energy and dissipative potentials, in the general framework of the internal state variables formulation, which is another difference from the approach of Dolinski et al. The constitutive model accounts for the strain hardening, thermal softening and ASB-induced material strength deterioration. The internal state variables to account for accordingly are: the elastic strain tensor $\mathbf{e}^e$, the absolute temperature T, the isotropic hardening variable κ and the ASB-related damage variable D. In developing the $(1-D)$ type model, it is possible to express the equations comprising the $(1-D)$ in different forms. Here, following the general idea of [7], a coupling is imposed between the ASB-induced deterioration and hardening at the stored energy part of the state potential. The state potential is assumed in the form of Helmholtz free energy $\psi(e^e,T,\kappa;D)=\psi^e(e^e)+\psi^p(\kappa,T;D)$ and the elastic $\psi^e(e^e)$ and stored energy parts $\psi^p(\kappa,T;D)$ are then expressed as:

$$\begin{cases}\rho_0\psi^e = \frac{\lambda}{2}e^e_{ii}e^e_{jj} + \mu e^e_{ij}e^e_{ji} \\ \rho_0\psi^p = (1-D)h(\kappa)g(T)\end{cases} \tag{3.3}$$

The strain hardening function $h(\kappa)$ and thermal softening $g(T)$ function take the same form as the **D** type model, see Chapter 2, Section 2.3.3, as:

$$\begin{aligned} h(\kappa) &= R_\infty \left[\kappa + \frac{1}{k} \exp\left(-k\kappa\right) \right] \\ g(T) &= \exp\left(-\upsilon T\right) \end{aligned} \tag{3.4}$$

The state laws comprising the conjugate forces namely the stress tensor $\boldsymbol{\tau}$, the strain hardening thermodynamic force (affinity) r and the deterioration conjugate force scalar G are derived from (3.3) as:

$$\begin{cases} \tau_{ij} = \rho_0 \dfrac{\partial \psi}{\partial e^e_{ij}} = \lambda e^e_{kk} I_{ij} + 2\mu e^e_{ij} \\ r = \rho_0 \dfrac{\partial \psi}{\partial \kappa} = (1-D) h'(\kappa) g(T) \\ G = -\rho_0 \dfrac{\partial \psi}{\partial D} = h(\kappa) g(T) \end{cases} \tag{3.5}$$

The intrinsic dissipation $\mathfrak{D}_{\text{int}}$ is formulated as:

$$\mathfrak{D}_{\text{int}} = \boldsymbol{\tau} : \mathbf{d}^{\mathbf{p}} - r\dot{\kappa} + G\dot{D} \geq 0 \tag{3.6}$$

The regular temperature evolution is expressed by the common relation established with the assumption of adiabaticity ([9], [10]), where the contribution of $G\dot{D}$ is tentatively neglected.

$$\dot{T} = \frac{\boldsymbol{\tau} : \mathbf{d}^{\mathbf{p}} - r\dot{\kappa}}{\rho_0 c_0} \tag{3.7}$$

An associated plasticity is followed here with the yield function and plastic potential given by a single function F shown in (3.8) ; it contains the information about both regular plasticity and singular ASB-induced strain localization, and allows further for deriving the internal variables evolution laws in the context of the normality rule.

$$\mathrm{F}\left(\boldsymbol{\tau}, r\right) = \sigma_{eq}\left(\boldsymbol{\tau}\right) - \left[(1-D) R_0 g(T) + r\right] = \sigma_v \tag{3.8}$$

$$\sigma_{eq}\left(\boldsymbol{\tau}\right) = \sqrt{\frac{3}{2} \mathbf{s} : \mathbf{s}} \tag{3.9}$$

σ_{eq} is the Von Mises equivalent stress with **s** being the deviatoric part of the stress tensor $\boldsymbol{\tau}$.

The plastic strain rate and isotropic hardening variable rate are derived from the yield function (3.8) according to the normality rule as shown in (3.10) below, whereas the evolution law of *D* is derived from the empirical expression in (3.2).

$$\begin{cases} d_{ij}{}^{p} = \Lambda \dfrac{\partial F}{\partial \tau_{ij}} = \dfrac{3}{2} \Lambda \dfrac{s_{ij}}{\sigma_{eq}} \\ -\dot{\kappa} = \Lambda \dfrac{\partial F}{\partial r} = -\Lambda \\ \dot{D} = A \dot{W}_p \end{cases} \tag{3.10}$$

The viscoplastic multiplier Λ is expressed in (3.11) where *Y* and *n* are viscosity constants.

$$\Lambda = \left\langle \frac{\mathrm{F}}{(1-D)Y} \right\rangle^{n} \tag{3.11}$$

The viscous stress σ_v in (3.8) is therefore deduced from $(3.10)_2$ and (3.11) as follows:

$$\sigma_v = (1-D) Y \dot{\kappa}^{1/n} \tag{3.12}$$

Combining (3.8) and (3.11) yields:

$$\sigma_{eq} = (1-D)\left[R_0 g(T) + h'(\kappa) g(T) + Y \dot{\kappa}^{1/n} \right] \tag{3.13}$$

It must be noted that the form (3.13) is intentionally close to the form (2) in [7] p.1761 (with exponent b=1), while the strain, strain rate hardening and thermal softening functions are different (expressed by (4) in [7] p.1761).

3.2.2 Model Calibration and Verification

As mentioned in the Introduction, the first two steps of the V&V process, namely the constants calibration and verification of the **D** type and $(1-D)$ type models, are dealt with in the current section. The first step in numerically implementing the models is to identify the deterioration related material constants at the RVE scale by fitting the numerical results to the experimental one. Then the model has to be verified before applying it to a complex initial boundary value problem. This verification step is ideally done on a simple structure with the shear band path known a priori. One such structure is the hat shaped structure. The model is validated if the simulation results fit the experimental ones. The material considered in the present section is high strength steel.

$(1-D)$ type model was implemented as a user material subroutine VUMAT in the commercial, explicit, finite element computational code Abaqus-Exp with the rate equations being integrated using an implicit scheme. The numerical analyses are carried out using finite elements of the type C3D8R (Continuum, 3-D, 8-node, Reduced integration).

3.2.2.1 Step 1: Constants identification

In the case of $(1-D)$ type model, the single damage-material constant is A (in (3.2)) and in the case of $\mathbf{D}$ type model, there are seven damage-material constants $(a, b, \chi_1, \chi_2, Z, m, \eta_{ASB})$ (refer Chapter 2). In order to identify these constants, the result of the experiments performed by Marchand and Duffy [11] to study ASB formation process was used as a base. According to the large scale postulate, the HY-100 steel torsional specimen used by Marchand and Duffy is indeed rolled out and herein viewed as the RVE, see Fig. 3.2. The corresponding numerical analyses are carried out on a single finite element subjected to dynamic shear loading as shown in Fig. 3.2.

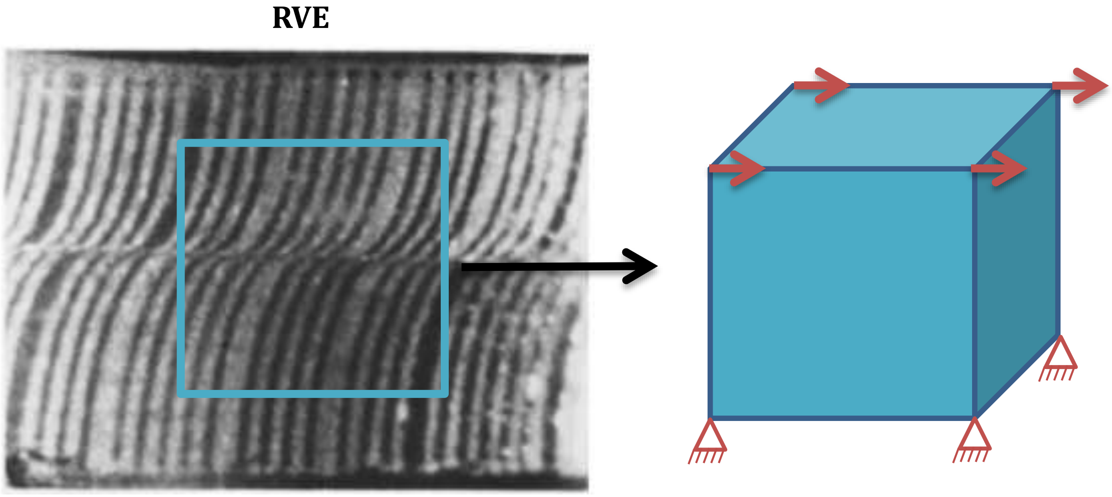

Fig. 3.2 Left: Shear deformation pattern observed in specimen after dynamic torsional loading showing the desired RVE. After [11]**. Right:** Brick finite element subjected to dynamic shear similar to the former RVE.

Rather than using W_f as failure criterion, see (3.2) and Fig.3.1, a critical value of damage was set to 0.8 rather than 1 for the $(1-D)$ type model. This was done by Lemaitre [6] based on the experimental observations. At this value of *D*, the material loses its load bearing ability completely and the stresses are assigned zero. This step was carried out for the **D** type model in LS-DYNA by Longère et al. [4]. For the **D** type model, the theoretical maximum of the deterioration intensity $\mathcal{D}_c = \mu / b$ for the given material would be 5, which value is never attained in the present analyses.

The ASB-induced drop in stress is fitted with that of the experimental curve. The Fig. 3.3 shows the superposed shear stress – shear strain plots reproduced from Marchand & Duffy's experiment and the numerical results for the $(1-D)$ type model and **D** type model.

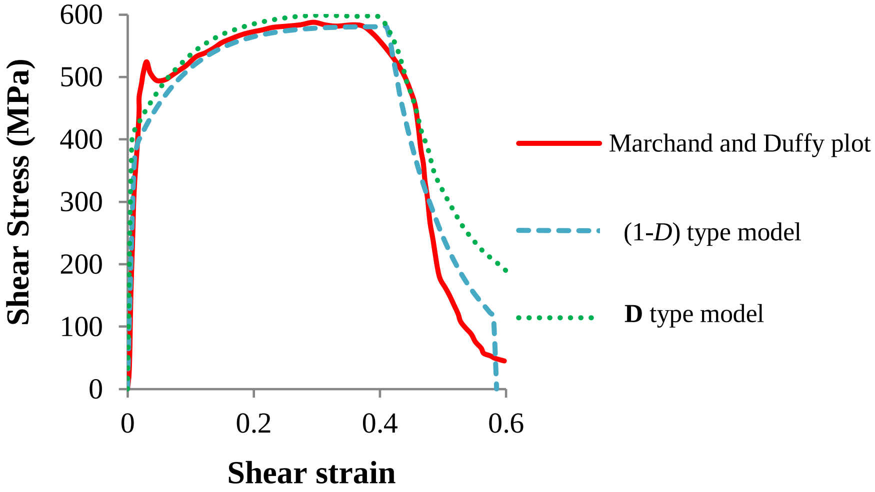

Fig. 3.3 Experimental and simulated shear stress-shear strain curves for Marchand and Duffy torsion test.

The elastic-viscoplastic and thermal constants for HY-100 identified are shown in Table 3.1. By fitting the ASB-induced drop in stress with that of the experimental curve, the corresponding value of the constant *A* of the $(1-D)$ type model was found to be $3\text{x}10^{-8}$ $(\text{J/m}^3)^{-1}$. The ASB induced deterioration related constants identified for the **D** type model are presented in Table 3.2.

Table 3.1 Material properties for HY 100 steel

Elastic - viscoplastic constants:

ρ_0 (kg/m^3)	c_0 (J/kg.K)	E (MPa)	ν	R_∞ (MPa)	R_{int} (MPa)	Y (MPa. s$^{1/n}$)	n
7800	500	200e+3	0.33	400	510	100	10

Thermal properties:

k	υ (°C^{-1})	T_0 (°C)	$\bar{\alpha}$ (/K)
20	1.5e-3	20	1e-6

Table 3.2 ASB related constants for **D** type model for high strength steel

Z (MPa. s$^{1/n}$)	m	η_{ASB} (MPa^{-2})	χ_1	χ_2	a (MPa)	b (MPa)
19	2	0.12	0.05	0.05	0	15e+3

3.2.2.2 Step 2: Application to dynamic shear loading of a structure

The hat shaped structure (HSS) used here for the verification of the models was developed by Couque [12] in which the gauge section is tilted by an angle (32.6°) to the loading axis (see Fig. 3.4a). This geometry admits constant positive pressure and shear loading thereby creating a condition of negative stress triaxiality making it conducive for ASBs to form. The ASB trajectory (i.e. gauge section) is known a priori and hence relatively fine mesh can be placed in this region. The test consists of directly impacting the hat specimen in a direct Hopkinson pressure bar setup (Fig. 3.4b) with a striker bar of a given length ($L_{striker}$) and impacting velocity ($V_{striker}$). The striker and output bar are made of tungsten.

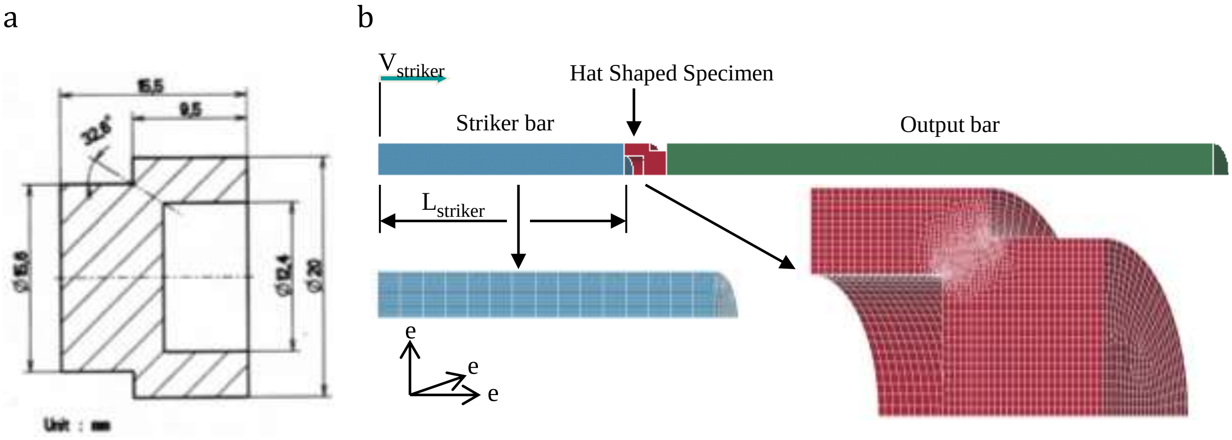

Fig. 3.4 (a) Hydrodynamic Hat Specimen; (b) Direct Hopkinson bar setup. After Longère et al. [1].

The material used for HSS in the current step is 30 Ni-Cr-Mo 6-6 steel in order to be able to compare with the available experimental data. The elastic-viscoplastic and thermal material constants of 30 Ni-Cr-Mo 6-6 steel tabulated in Chapter 2 are very close to HY-100 steel properties and are shown again in Table 3.3 below, whereas the damage constants identified from Step 1 are maintained in the current step in the interest of verifying the models.

The experimental results and the numerical simulation for the **D** type model are obtained from [1] and [13]. Experimental and numerical results for both (1-*D*) and **D** type models are compared in terms of:

- ASB induced deterioration map
- History of the stress transmitted into the output bar.

Table 3.3 Material properties for 30 Ni-Cr-Mo 6-6 steel

Elastic - viscoplastic constants:

ρ_0 (kg/m^3)	c_0 (J/kg.K)	E (MPa)	ν	R_∞ (MPa)	R_{int} (MPa)	Y (MPa. s$^{1/n}$)	n
7800	420	200e+3	0.33	400	920	60	6

Thermal properties:

k	υ (°C^{-1})	T_0 (°C)	$\bar{\alpha}$ (/K)	$\dot{\varepsilon}_{crit}$ (/s)
10	1.1e-3	20	1e-6	100

(1) Severe shock intensity

Consider the first configuration with L_{striker}=40 mm; V_{striker}=35.6 m/s, which produces a severe shock. In the post-mortem observation of the specimen (Fig. 3.5a), a macro-crack is observed in the gauge section on the upper side and a crossing ASB on the lower side. This implies that the ASB path has served as the site for crack formation. In the numerical simulation, the shear bands are seen to have initiated on both corners of the gauge section and propagated and crossed each other. This is the case for both $(1-D)$ and **D** type models and it is well in agreement with the specimen observation (Fig. 3.5 b,c). However it has to be noted that this condition is achieved very soon for the $(1-D)$ type model (step time = 6μs) as opposed to 40μs step time in the **D** type model.

Hence the numerical deterioration map in itself is not sufficient to validate the performance of the models. The pulse transmitted to the output bar of the Hopkinson setup gives an indication of the intactness of the specimen. So numerical stress histories in the output bar obtained for the two models are compared with the experimental one. From (Fig. 3.6 a,b), it is seen that for the $(1-D)$ type model, the material failure occurs very soon, whereas the **D** type model is able to trace the experimental stress history.

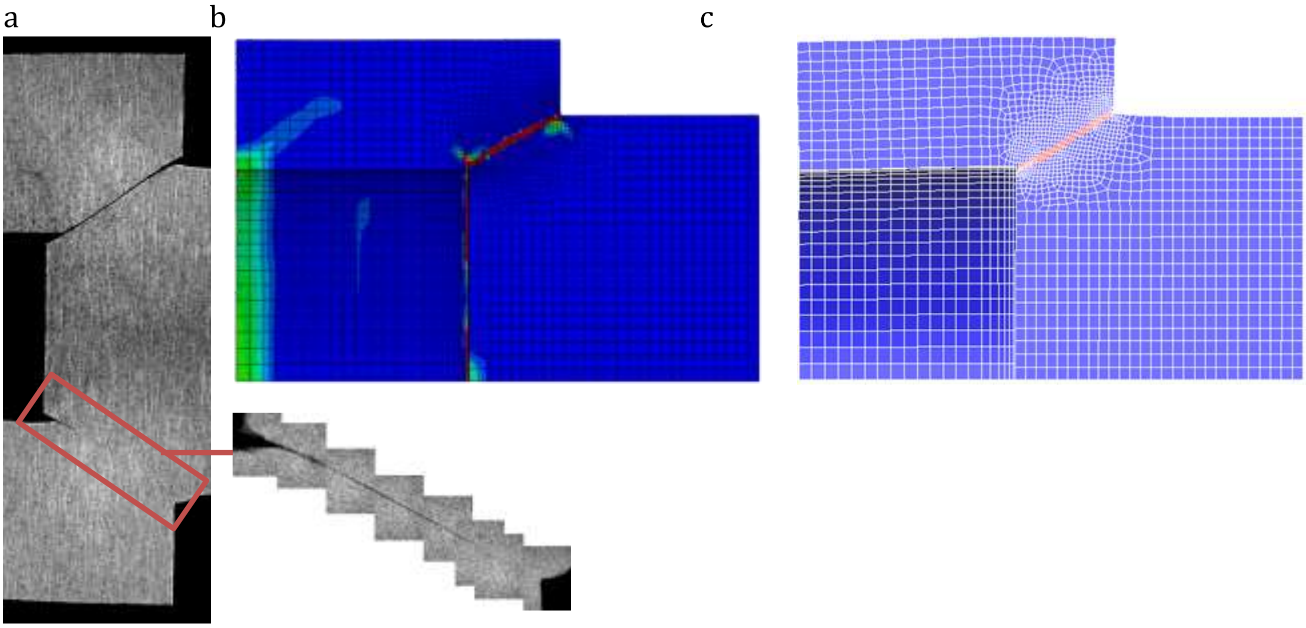

Fig. 3.5 Configuration with Lstriker=40 mm; Vstriker=35.6 m/s. (a) Specimen post-mortem; (b) numerical deterioration map of (1-*D*) type model (Step time = 6 μs); (c) numerical deterioration map of **D** type model (Step time = 40 μs). After [1].

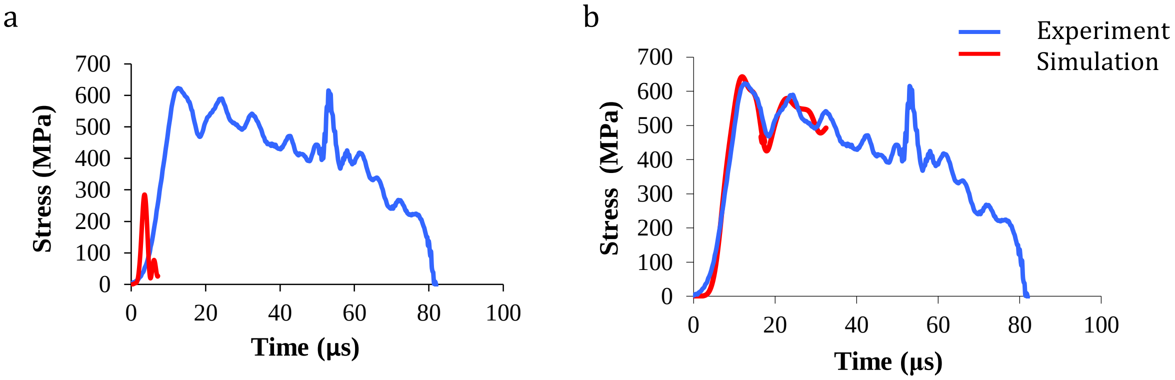

Fig. 3.6 Configuration with Lstriker=40 mm; Vstriker=35.6 m/s. (a), (b) Experimental and numerical stress histories in the output bar for (1-*D*) and **D** type model respectively.

(2) Moderate shock intensity

The configuration with $L_{striker}$=90 mm and $V_{striker}$=23.7 m/s produces a moderate shock. In the post-mortem observation of the specimen (Fig. 3.7a), the ASB is seen to have partially propagated along the gauge sections. In the numerical simulation, for the case of $(1-D)$ type model (Fig. 3.7b), crossing shear bands across the gauge section is observed unlike the experimental observation, whereas the **D** type model shows partially propagated shear bands similar to the specimen post-mortem (Fig. 3.7c). Likewise in the stress history (Fig. 3.8), it is seen that the $(1-D)$ type model shows material failure at about 8µs, whereas the **D** type model is able to reproduce the full experimental stress plot.

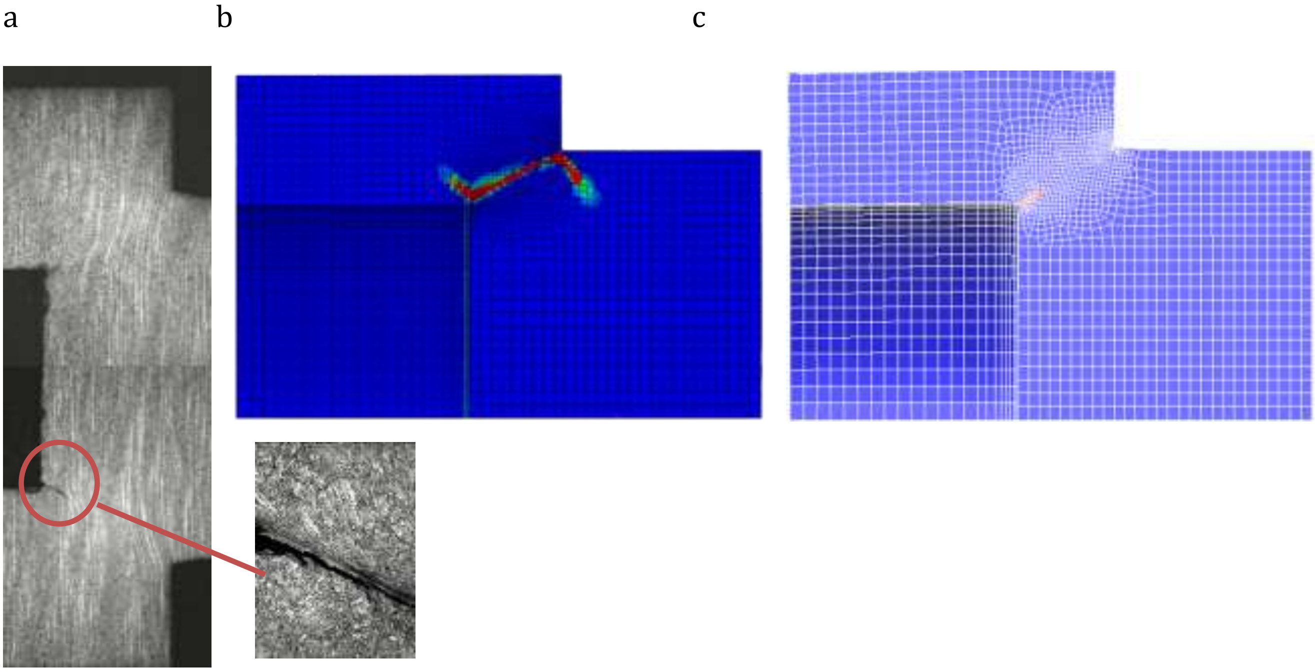

Fig. 3.7 Configuration with Lstriker=90 mm; Vstriker=23.7 m/s. (a) Specimen post-mortem; (b) numerical deterioration map of $(1-D)$ type model (Step time = 8.2 µs); (c) numerical deterioration map of **D** type model (Step time = 150 µs). After [1].

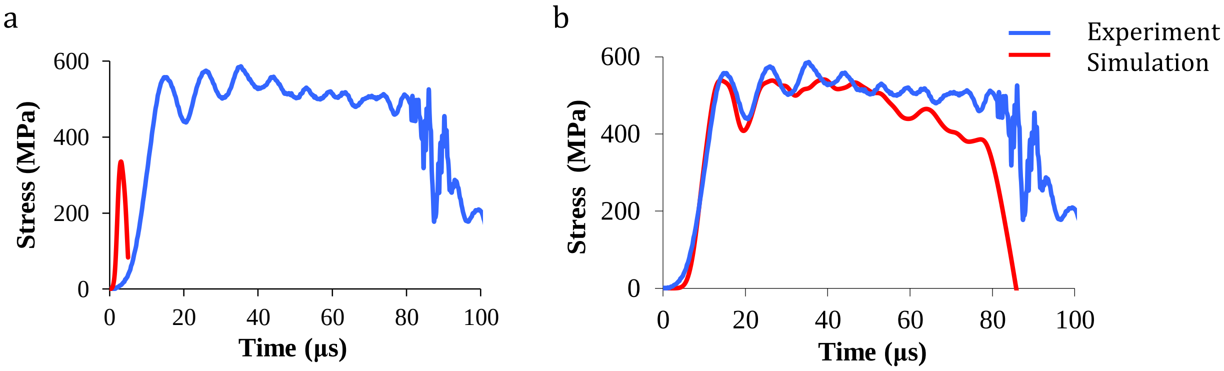

Fig. 3.8 Configuration with Lstriker=90 mm; Vstriker=23.7 m/s. (a), (b) Experimental and numerical stress histories in the output bar for $(1-D)$ and **D** type model respectively.

(3) Low shock intensity

Fig. 3.9 shows the results for the low shock configuration with $L_{striker}$=200 mm; $V_{striker}$=17.8 m/s. Again the $(1-D)$ type model shows a full crossing band at 9µs but the **D** type model shows partially propagated bands similar to the experimental observation.

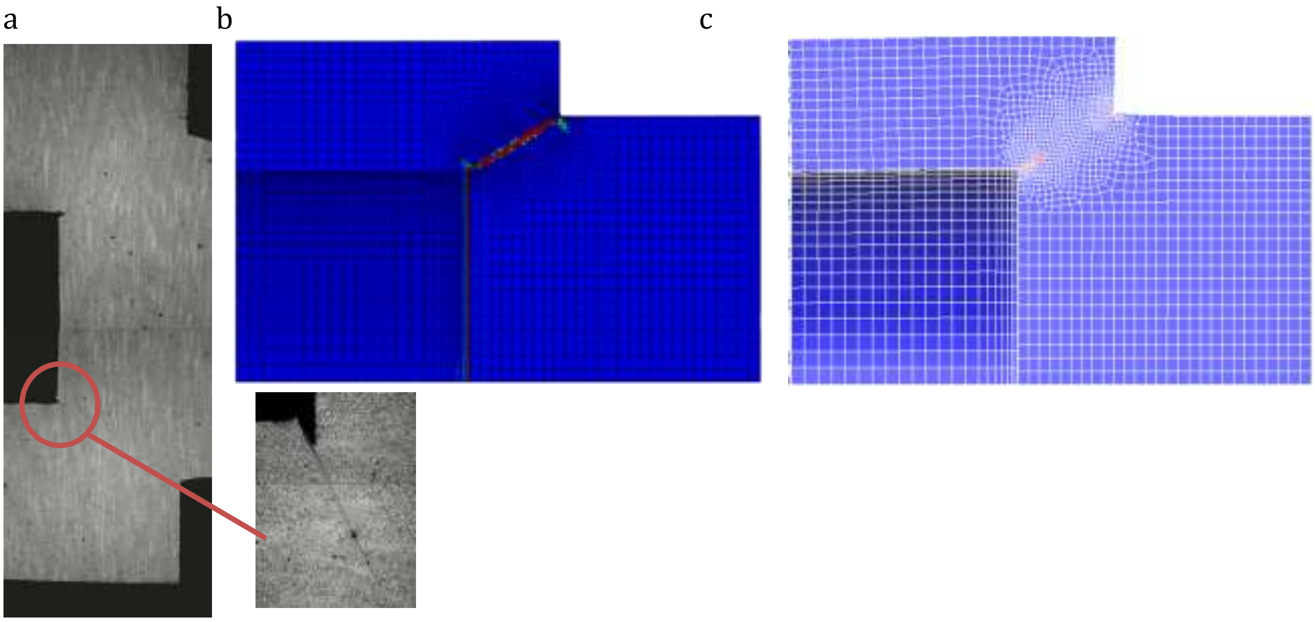

Fig. 3.9 Configuration with Lstriker=200 mm; Vstriker=17.8 m/s. (a) Specimen post-mortem; (b) numerical deterioration map of (1-D) type model (Step time = 9 µs); (c) numerical deterioration map of **D** type model (Step time = 100 µs). After [1].

Correspondingly the stress histories (Fig. 3.10) reveal that the $(1-D)$ model shows premature material failure but the **D** type model is able to reproduce the experimental result.

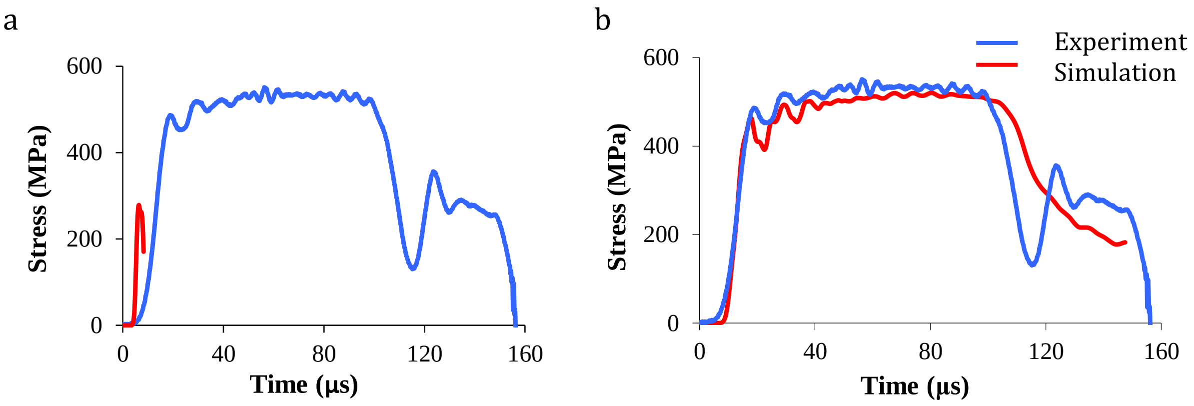

Fig. 3.10 Configuration with Lstriker=200 mm; Vstriker=17.8 m/s. (a), (b) Experimental and numerical stress histories in the output bar for (1-D) and **D** type model respectively.

3.2.3 Discussion

In order to understand the discrepancies of the results obtained with the two models and in particular the reason why the $(1-D)$ type model is unable to reproduce the experimental results, the damage evolutions are plotted for selected finite elements in the gauge section (Fig. 3.11). In Fig. 3.12, for the $(1-D)$ type model, the rate of damage evolution is seen to be very high and increasing when compared to that of **D** type model. It is to be noted that the time scale is in microsecond for the $(1-D)$ type model and in millisecond for the **D** type model. It takes approximately 40µs for the deterioration to grow from zero to maximum for the **D** type model, whereas it takes just about 1µs for the $(1-D)$ type model. Thus it is deduced that this increasing rate of damage for the (1-D) type model is the cause for the premature failure of the structure in the numerical simulation. By contrast, the **D** type model has a self-controlled damage evolution rate.

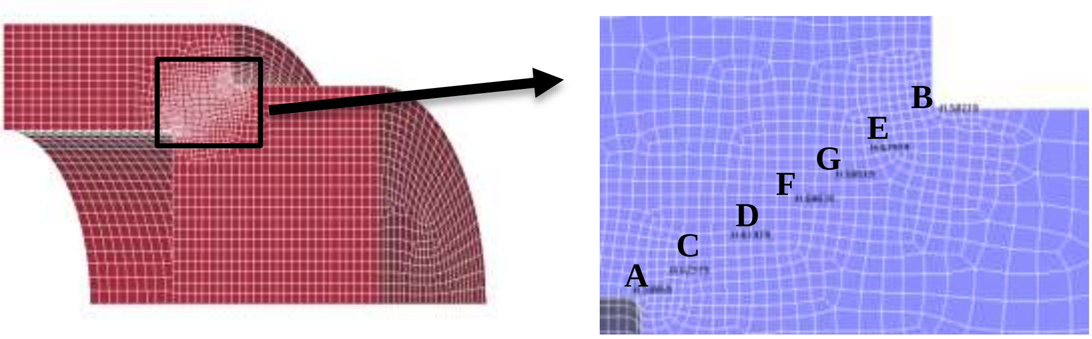

Fig. 3.11 Finite elements selected for damage plot

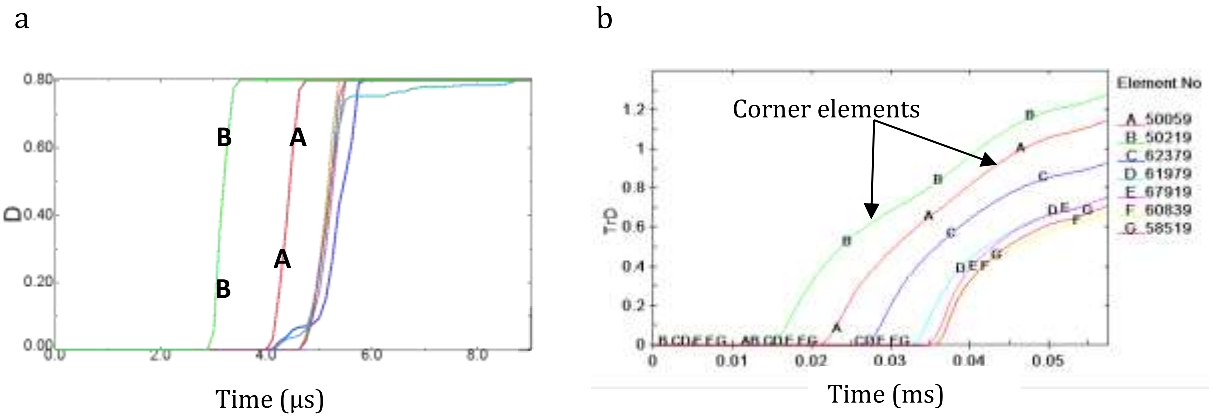
a

b

Fig. 3.12 (a) Increasing damage rate seen in (1-D) type model ; (b) Self-controlled damage rate in **D** type model. After [13]

As it is known that the damage kinetics in the $(1-D)$ type model is proportional to the damage related material constant A (see (3.2)), it would be interesting to observe the results with a slowed damage rate by reducing the value of this constant A. The $(1-D)$ type model was able to reproduce the experimental deterioration and stress-history (Fig. 3.13) when the constant A was reduced from $3\text{x}10^{-8}$ $(\text{J/m}^3)^{-1}$to $9\text{x}10^{-10}$ $(\text{J/m}^3)^{-1}$. Physically this would imply that the value of the failure strain energy density W_f is increased.

However while re-plotting the stress-strain for the single finite element, as done in the first step for constants identification in subsection 3.2.2.1 but now proceeding with the new value of A=9x10^{-10} (J/m^3)$^{-1}$, it is seen in Fig. 3.14 that the stress-strain dashed response does not fit the experimental curve. The softening due to the ASB is extremely slow. Thus we see that there is lack of compatibility between the single finite element and the HSS for this $(1-D)$ type model. A is supposed to be a material constant in [7] but in fact it needs to be adapted for different structures geometry and loading configurations accordingly to ensure model predictability.

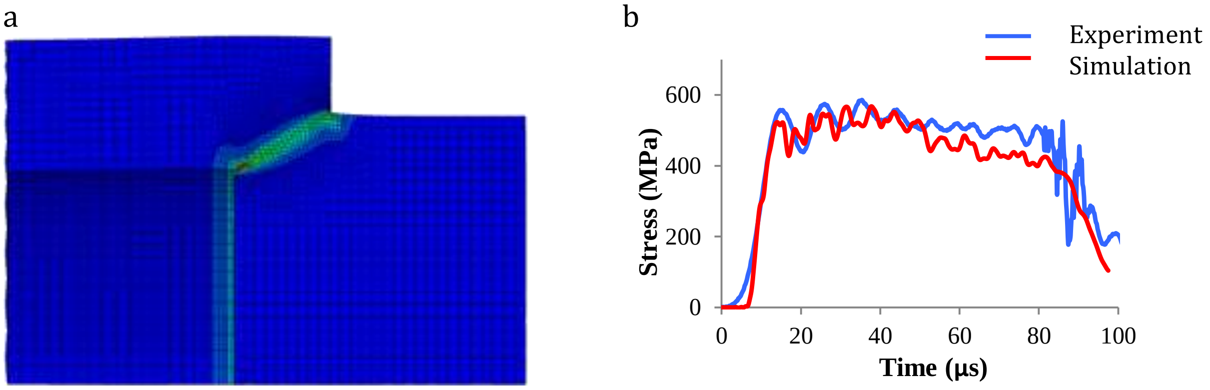

Fig. 3.13 (1-D) type model with slowed damage kinetics (a) Numerical deterioration map; (b) Stress history in output bar

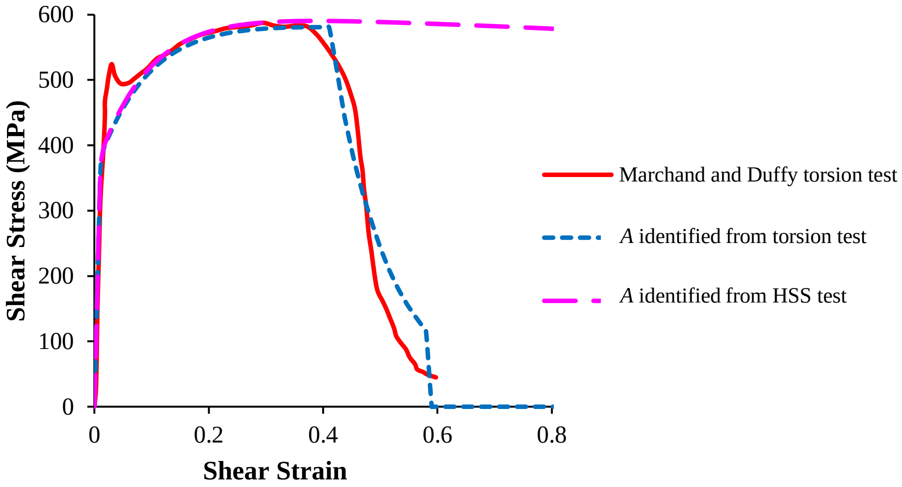

Fig. 3.14 (1-D) type model shear stress-shear strain plot for torsion test. The simulated post critical response is strongly dependent on the experiment (torsion test vs. HSS test) considered for the calibration of the constant A

On the other hand, it is evident that the **D** type model satisfies the HSS numerical simulation with the same set of damage-material constants as identified from the torsion test. It is to be noted that the numerical stress history in the output bar fits well the experimental one, except in the latest stage just before the material failure where there is slight deviation from the experimental plot. This shows that the **D** type model requires further enrichment in terms of taking into account the micro-mechanisms that operate in the late pre-failure stage such as the void growth. It is to be noted that the **D** type model describing the ASB induced deterioration without distinguishing micro-voiding has stood the test of V&V up to the final step of implementation on a complex IBVP considering the ballistic impact of a thick plate in [1].

3.3 ASSESSMENT OF THE ENLARGED MODEL

The feasibility of the enriched ASB+MV constitutive model at an RVE scale was demonstrated in Chapter 2. Following the (V&V) procedure, it is now required to verify the ASB+MV model on a structural scale. A HSS is used again to that purpose. It is reminded that the deterioration (ASB, MV) related constants for enriched model are tentatively chosen in such a way so as to exaggerate the effect of MV in order to be able to clearly distinguish the respective contributions of the two mechanisms of ASB and MV.

The enlarged ASB+MV constitutive model has been implemented as a user material subroutine in the commercial, explicit, finite element computation code LS-DYNA with the rate equations being integrated using an explicit scheme. The numerical analyses are carried out using brick finite elements (continuum, 3-D, 8-node, reduced integration)

3.3.1 Case of High Strength Steel

Simulations are carried out for impact of steel HSS in a direct Hopkinson bar setup made up of tungsten, with a striker bar velocity of 30 m/s; see Fig. 3.4. As it is the case of steel, only thermal softening is taken into account as the softening mechanism leading to the formation of ASB. The ASB and MV related material constants used here for 30 Ni-Cr-Mo 6-6 steel are tabulated in Chapter 2 and shown below in Table 3.4.

Table 3.4 Material properties for 30 Ni-Cr-Mo 6-6 steel

ASB related constants:

Z (MPa. $s^{1/n}$)	m	η_{ASB} (MPa^{-2})	χ_1	χ_2	a (MPa)	b (MPa)
15	2	0.01	0.04	0.04	0	15e+3

MV related constants:

W (MPa. $s^{1/n}$)	q	η_{MV} (MPa^{-2})	ξ	Ω
20	2	0.08	1	1.5

Two configurations are studied in the following: (i) configuration describing ASB effect only, i.e. with MV onset being deactivated, and (ii) configuration reproducing both ASB and MV effects where ASB-related constants are the same as those used in (i). The elementary responses of the RVE for both cases can be seen in Figs. 2.26-2.30.

Firstly, the resolved shear stress τ_{res} is examined as function of time for the elements in the gauge section (as shown in Fig. 3.11) of the HSS. The ASB model shows a relatively mild drop in strength in Fig. 3.15 after the ASB onset whereas the loss of strength is accelerated by the presence of MV in Fig. 3.16 for the ASB+MV model.

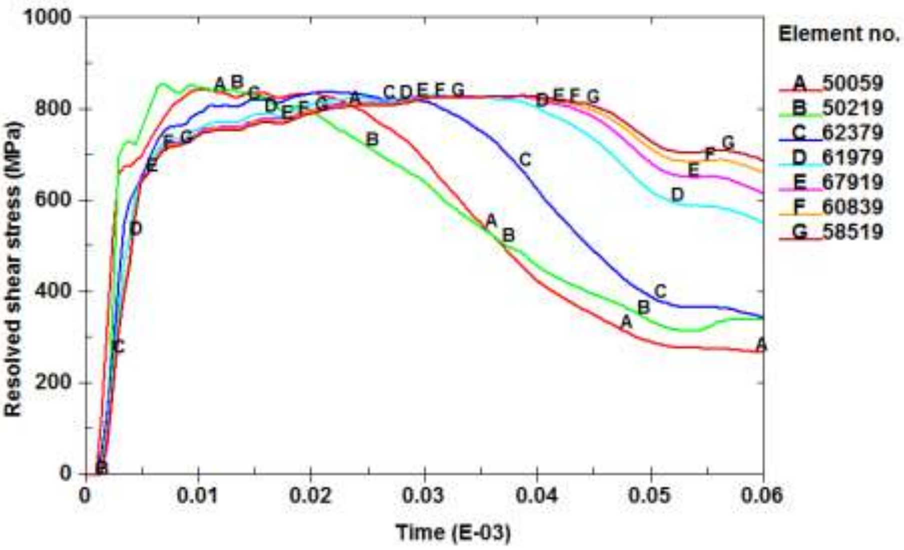

Fig. 3.15 Resolved shear stress history in finite elements located inside the strip of intense shearing, see Fig. 3.11. Configuration with ASB only. Numerical simulation of the dynamic loading of hat shaped structure.

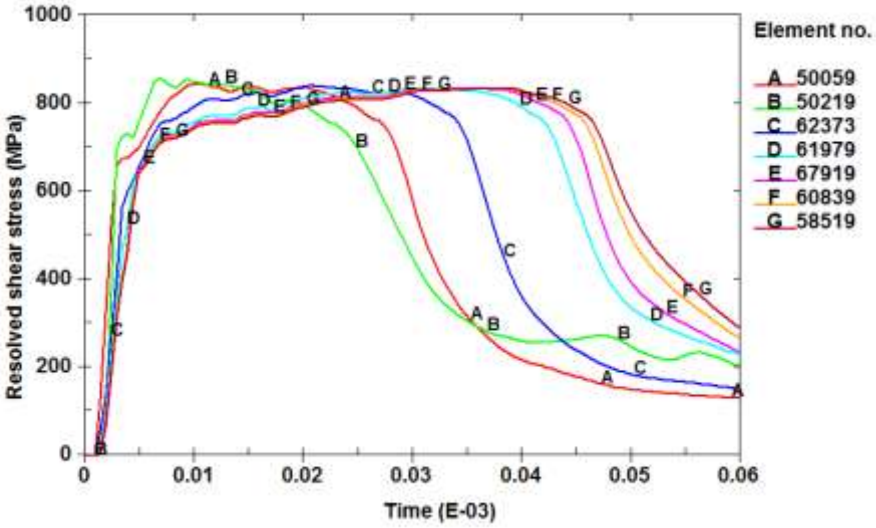

Fig. 3.16 Resolved shear stress history in finite elements located inside the strip of intense shearing, see Fig. 3.11. Configuration with ASB+MV. Numerical simulation of the dynamic loading of steel hat shaped structure.

The evolution of the deterioration variable $Tr\mathbf{D}$ for ASB and ASB+MV is plotted in Fig. 3.17 and Fig. 3.18 respectively. As expected, the deterioration intensity is significantly higher for the ASB+MV case, Fig. 3.18, when compared with the ASB only model, Fig. 3.17.

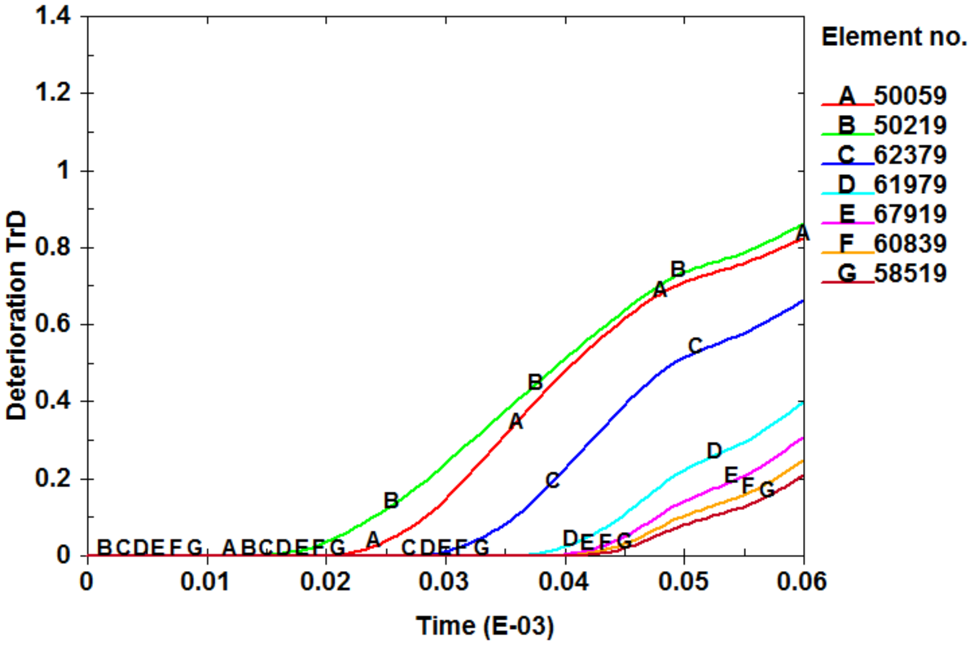

Fig. 3.17 Degradation variable history in finite elements located inside the strip of intense shearing, see Fig. 3.11. Configuration with ASB only. Numerical simulation of the dynamic loading of HSS.

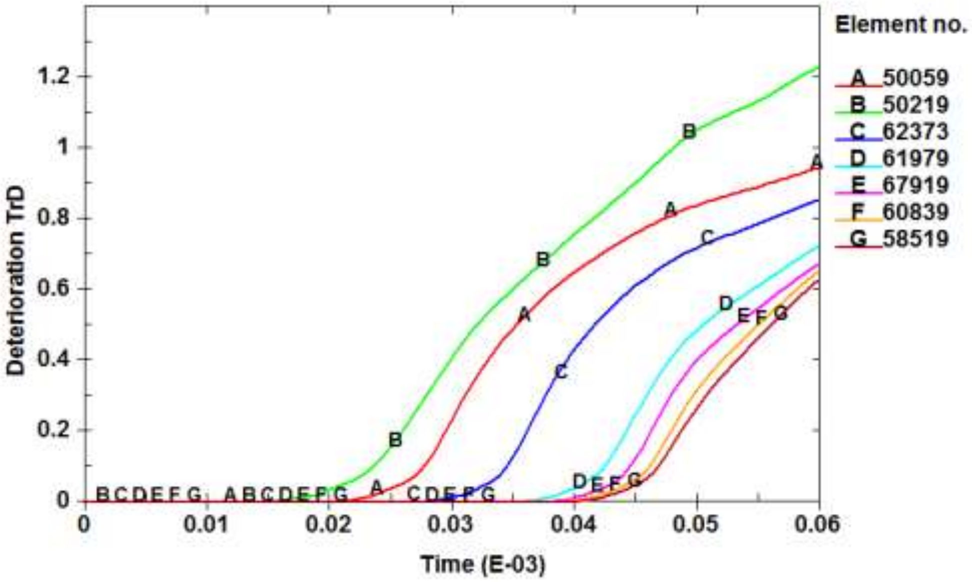

Fig. 3.18 Degradation variable history in finite elements located inside the strip of intense shearing, see Fig. 3.11. Configuration with ASB+MV. Numerical simulation of the dynamic loading of HSS.

The numerical deterioration map gives an indication of the presence of ASB/MV in the finite elements. In Fig. 3.19, for the case of ASB only, the elements in red are subject to ASB whereas the elements in green are not. Fig. 3.20, corresponding to the configuration with ASB+MV, shows the elements subject to ASB (Fig. 3.20a, elements in red) and the elements subject to MV (Fig. 3.20b, element in magenta). These numerical results bring two comments. Firstly, at the same time, considering ASB only leads to a partial propagation of ASB in the gauge section (Fig. 3.19), whereas considering both ASB+MV leads to a complete propagation of ASB (Fig. 3.20). MV in ASB wake thus contributes to propagating the ASB farther. Secondly, according to Fig. 3.20 and assuming that the loading ends at the time considered, although ASB has propagated throughout the whole structure, MV zones cover very limited areas, viz. near the specimen corners. The material in the ligament between the MV zones, which has been subject to ASB, may recover its initial properties after unloading due to phase transformation. In other words, the remaining effect of ASB+MV may reduce to MV alone with only local parts of the structure affected. In another scenario, the quenching of the material of ASB after unloading and cooling may cause micro-cracking, leading to a complete fracture of the structure.

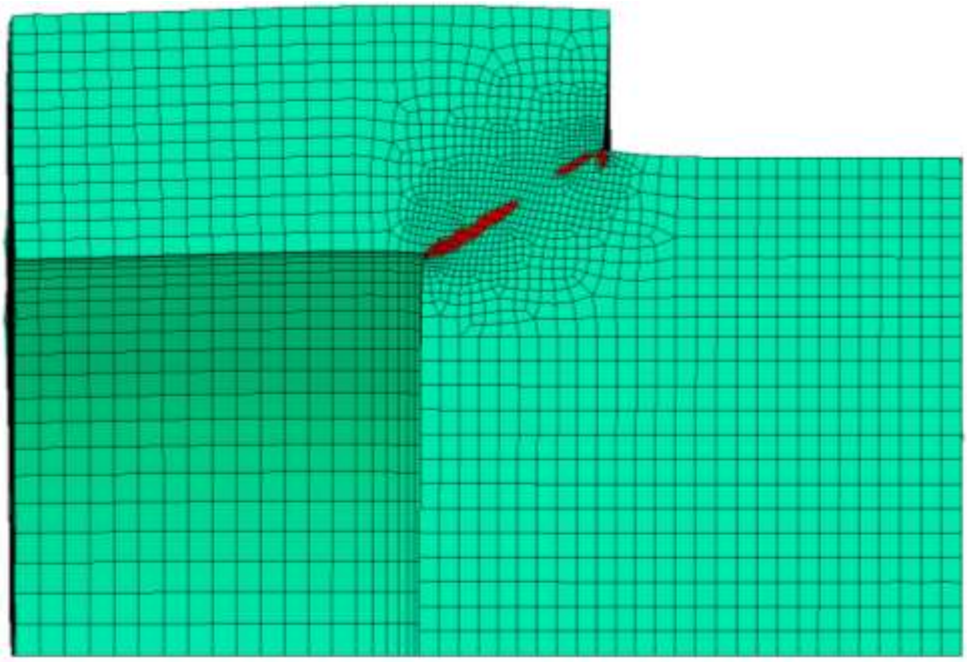

Fig. 3.19 Map of the degradation variable indicator at 40.5μs. Elements in red/dark are subject to ASB. Configuration with ASB only. Numerical simulation of the dynamic loading of HSS.

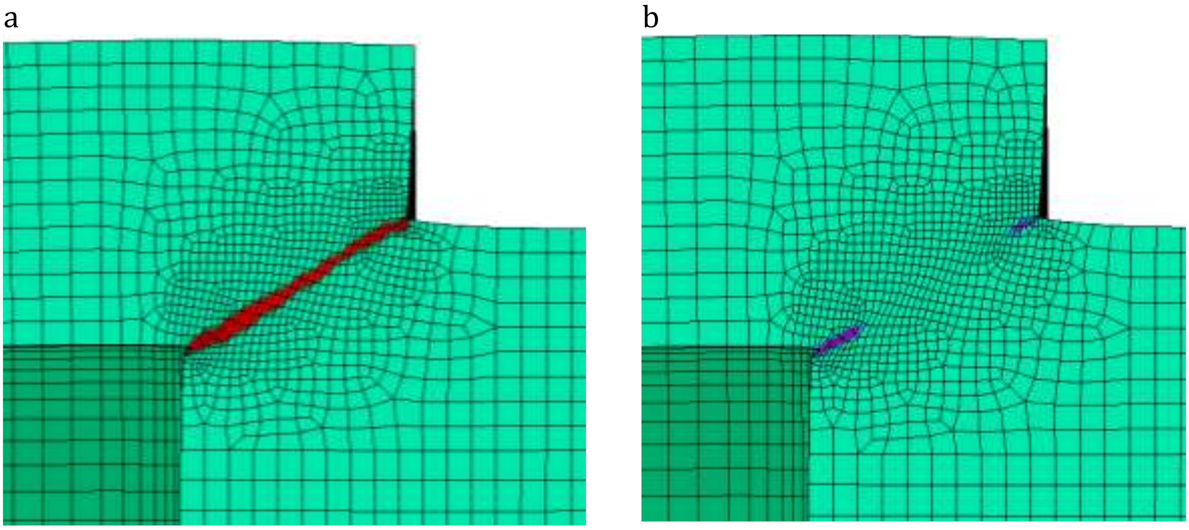

Fig. 3.20 Map of the degradation variable indicator at 40.5µs. Configuration with ASB+MV. Numerical simulation of the dynamic loading of HSS. a) Elements in red are subject to ASB. b) Elements in magenta are subject to MV.

3.3.2 Case of Ti6Al4V

As mentioned in Chapter 2, Section 2.4.2.2, the works of Rittel and co-workers [14] suggest that, for materials such as Ti alloys, the phenomenon of dynamic recrystallization (DRX) potentially needs to be taken into account in ASB initiation. Unlike the common assumption that DRX is a consequence of ASB, they argue that the DRX not only precedes the ASB but is also a dominant microstrutural factor in the very generation of the band. Osovski et al. [15] concluded that the respective influence of thermal and DRX induced softening depends on the chronology of the process and the material considered: in case of Ti6Al4V, DRX develops earlier and overrides the thermal softening effects; on the other extreme case of pure tantalum which does not undergo DRX, the thermal softening plays a dominant role in the ASB initiation. In the line of their work, the competition occurring between thermal and DRX induced softening is analyzed here on a structural scale. The table showing the materials constants of Ti6Al4V from Chapter 2, see Section 2.5.2.2, is reminded below.

Table 3.5 Material properties for Ti-6Al-4V

Elastic - viscoplastic constants:

ρ_0 (kg/m^3)	c_0 (J/kg.K)	E (MPa)	ν	R_∞ (MPa)	R_{int} (MPa)	Y (MPa. s$^{1/n}$)	n
4500	460	113e+3	0.34	972	1080	400	44

Thermal properties:

T_0 (°C)	$\bar{\alpha}$ (/K)	T_{ref} (K)	t	$\dot{\varepsilon}_{crit}$ (/s)
20	1e-6	923	0.6	100

ASB related constants:

Z (MPa. s$^{1/n}$)	m	η_{ASB} (MPa^{-2})	χ_1	χ_2	a (MPa)	b (MPa)
100	2	0.01	0.04	0.04	0	15e+3

MV related constants:

W (MPa. s$^{1/n}$)	q	η_{MV} (MPa^{-2})	ξ	Ω
75	2	0.05	1	2

DRX related constants:

$\bar{Y}_0$	$\bar{Y}_{\max}$	κ_c	$\Delta\kappa_r$	η (MPa)
14	14	0.2	0.8	1.36e+4

In order to study the potential effect of DRX on ASB formation and evolution, two cases are examined in the simulation of HSS:
(1) no thermal softening and with DRX (No TS & With DRX)
(2) with thermal softening and with DRX (With TS & With DRX)
These configurations have to be considered together with those studied in Chapter 2, Section 2.5.2.2.

The resolved shear stresses for both cases for the selected elements in the gauge section (as shown in Fig. 3.11) of the HSS are plotted in Fig. 3.21a,b. In the graphs, the red marks indicate the ASB onset and the green ones MV onset. While examining the two cases for the instant of ASB onset, it is clearly seen that the case with combined DRX and thermal softening (Fig. 3.21b) shows relatively early onset of ASB when compared to the case of DRX induced softening only (Fig. 3.21a). Consequently the MV onset also takes place earlier for the former case than the latter. The results seen here are similar to the ones observed in the corresponding cases for the single FE in Chapter 2, Section 2.5.2.2.

The deterioration maps showing the elements with ASB and MV activated respectively at a given instant (viz. 40.5µs) for the above two cases are shown in Fig. 3.22. In the case considering DRX induced softening solely (Fig. 3.22a), fewer elements show ASB and MV at the given instant. The combined influence of thermal and DRX induced softening seems to have accelerated the ASB and MV onset which is seen in the deterioration map (Fig. 3.22b) in which relatively more elements are seen with the presence of ASB and MV.

As a consequence, neglecting the thermal softening and considering only DRX induced softening for materials such as Ti6Al4V as proposed by Osovski et al.[15], would lead to delay of ASB initiation and underestimation of the ASB propagation. However more experimental evidence is needed to characterize each material in terms of the respective influence of thermal and DRX induced softening on the shear localization onset.

a

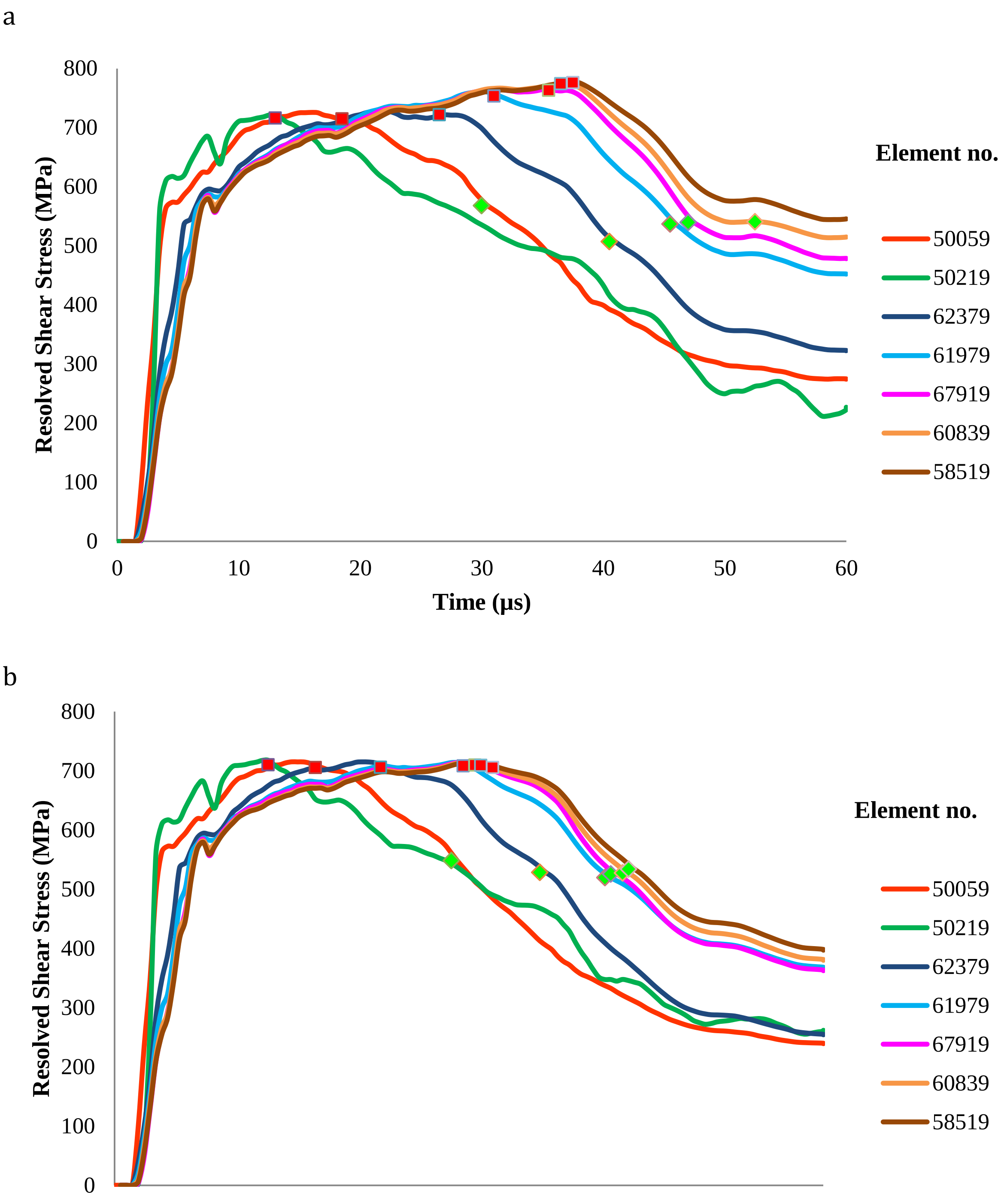

Fig. 3.21 Resolved shear stress history in finite elements located inside the strip of intense shearing, see Fig. 3.11. Configuration with ASB+MV. Numerical simulation of the dynamic loading of Ti6Al4V hat shaped structure. a) Case of no thermal softening and with DRX b) Case considering thermal softening and DRX.

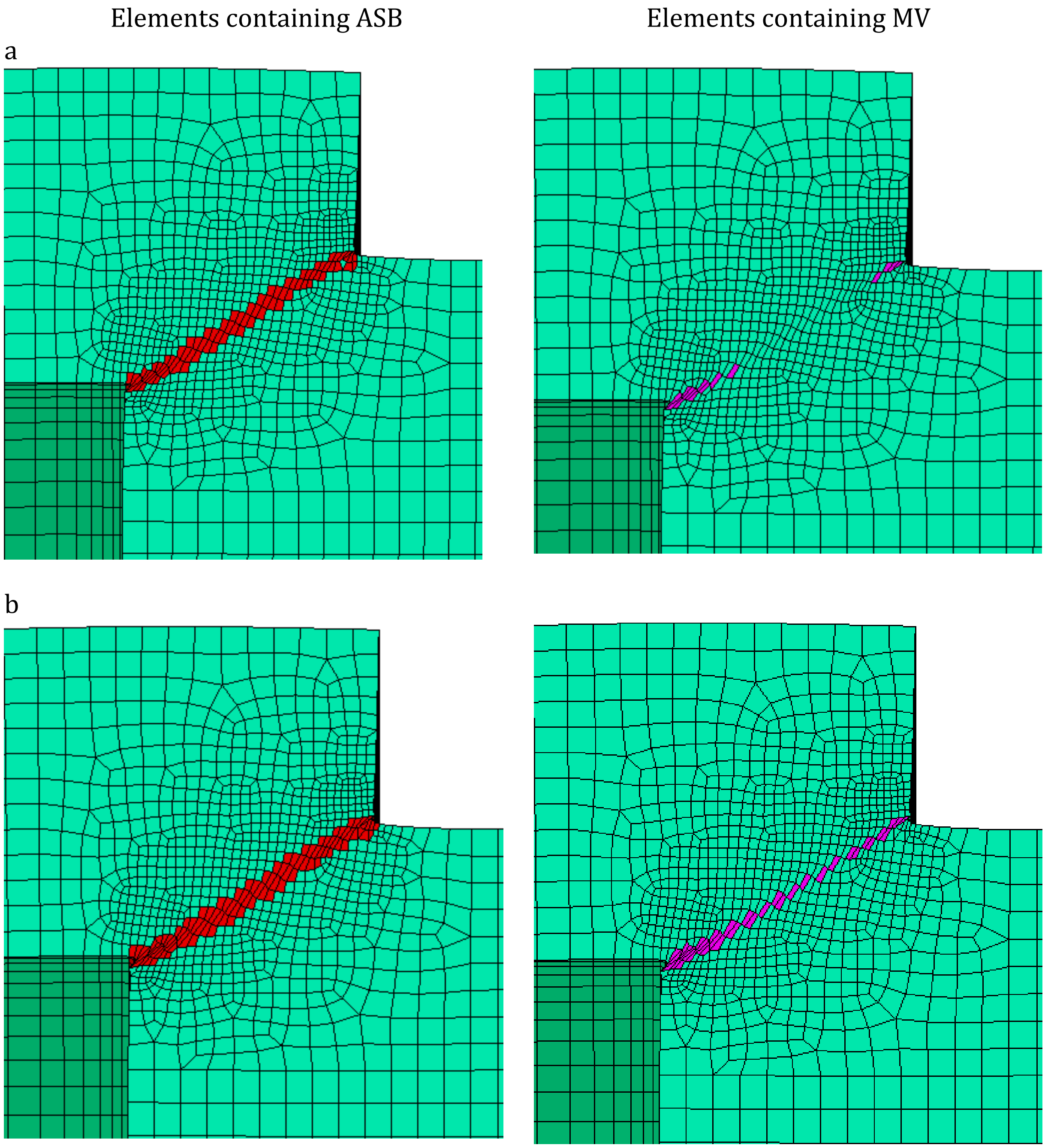

Fig. 3.22 Map of the degradation variable indicator at 40.5μs. Configuration with ASB+MV. Numerical simulation of the dynamic loading of Ti6Al4V hat shaped structure. Elements in red/dark are subject to ASB. Elements in magenta/dark are subject to MV. a) Case of no thermal softening and with DRX b) Case considering thermal softening and DRX.

3.3.3 Discussion/assessment

The enriched ASB+MV constitutive model is thus demonstrated to be feasible on a structural scale and shows the desired qualitative performance on the IBVP.

- ASB only vs. ASB+MV

While comparing the two models exhibiting ASB only and ASB+MV when implemented on a structural scale, the following conclusion can be drawn. The model with ASB and MV activated exhibits increased deterioration intensity and therefore accelerates the drop in strength of the material which is the expected behaviour. Also, while comparing with the ASB only model, the presence of MV advances the ASB propagation.

Not all elements containing ASB show the presence of MV at a given instant. This would imply that, upon loading at that given instant, if the material within the ASB recovers its initial properties due to phase transformation, the only deteriorated region would be the elements containing MV. It is thus essential to distinguish the two mechanisms of ASB and MV.

- DRX vs. DRX+TS

In case of materials susceptible to DRX such as Ti alloys, in addition to thermal softening, the DRX induced softening plays a role on the ASB onset. The influence of the two softening mechanisms has been studied here concerning two cases namely DRX only and DRX+TS. It is seen that the combined DRX+TS leads to a much earlier onset of ASB and consequently MV when compared to the case with DRX induced softening only. It is therefore important to consider both the softening mechanisms in order to be conservative in the engineering approach.

3.4 TOWARD COMPLEX IBVP

In the aim of reducing the duration of machining process, high speed machining is preferred in modern production engineering. High speed machining (HSM) implies high strain rate loading and hence favours the formation of ASBs in high strength alloys. When formed, these shear bands play a role in chip serration in terms of chip morphology and reduce the load on the cutting tool while producing rough surface finish and causing tool oscillations. To optimize the conditions for HSM of high strength, light-weight alloys, it is thus essential to conduct numerical simulations. The present study aims at studying the influence of some parameters on the numerical results obtained from the simulation of the HSM process using a commercial finite element computation code, namely Abaqus. The parameters in question include notably the thermal conditions and some phenomenological criteria.

A number of theoretical and numerical studies have been carried out on the optimization of the cutting process notably on the Ti-6Al-4V titanium alloy in the small scale postulate framework, i.e. with a mesh size smaller than the bandwidth. Due to its engineering-oriented formulation, the Johnson-Cook model and its modified versions are the most widely used constitutive models to describe the workpiece material behaviour during HSM (see eg. [16],[17],[18],[19]). Molinari et al. [20] carried out numerical and analytical investigations about the role of cutting conditions on adiabatic shear banding and chip serration during the orthogonal cutting of Ti-6Al-4V. Here we extend their parametric study by performing numerical analyses of the effect of (i) plastic dissipation induced self-heating and (ii) the material failure triggered by a critical strain value. It is shown that the chip morphology is strongly dependent on the arbitrary values given to the inelastic heat fraction β and the critical strain to failure ε_p^{crit}.

Unlike the enlarged ASB+MV constitutive model, described in Chapter 2 and assessed in Section 3.3, developed in the large scale postulate framework, the small scale postulate is considered in the present Section. The limitations of the current methods aiming at reproducing the thermo-mechanical processes operating during HSM, including ASB and MV, are expected to be overcome by using the enlarged ASB+MV model in a prospective work.

3.4.1 Constitutive modelling

Some modelling related considerations are presented in this section.

- *Constitutive model*

In order to conduct numerical simulations of HSM, various factors characterizing the process need to be taken into account such as large strains, high strain rate and high temperature rise. The Johnson-Cook rate dependent model includes a multiplicative contribution of the combined effects of strain hardening, strain rate hardening and thermal softening. The Johnson-Cook constitutive equations expressed in (3.14) and (3.15) are tentatively employed here to model the thermo-viscoplastic behaviour of the Ti-6Al-4V workpiece material. In the current section, engineering notations are adopted.

$$\sigma_{eq}(\boldsymbol{\sigma}) = \sigma_y\left(\varepsilon_p, \dot{\varepsilon}_p, T\right) \tag{3.14}$$

With

$$\begin{cases} \sigma_{eq} = \sqrt{\dfrac{3}{2}\mathbf{s}:\mathbf{s}} \\ \sigma_y = (A + B\varepsilon_p^n)\left(1 + C\ln\dfrac{\dot{\varepsilon}_p}{\dot{\varepsilon}_0}\right)\left(1 - \left(\dfrac{T - T_0}{T_m - T_0}\right)^m\right) \end{cases} \tag{3.15}$$

where σ_{eq} represents Mises equivalent stress and σ_y is the flow stress, $\boldsymbol{\sigma}$ and $\mathbf{s}$ the Cauchy stress tensor and its deviatoric part respectively ; $\mathbf{I}$ is the identity tensor ; $\dot{\varepsilon}_p$ represents the equivalent Mises plastic strain rate and $\dot{\varepsilon}_0$ a reference strain rate, ε_p the accumulated plastic strain, T the current temperature, T_0 a reference temperature and T_m the melting temperature ; A, B, n, m are constants.

The plastic strain rate $\mathbf{d}^{PP}$, the equivalent Mises plastic strain rate $\dot{\varepsilon}_p$ and the accumulated plastic strain ε_p are expressed by

$$\mathbf{d}^{PP} = \frac{3}{2}\dot{\varepsilon}_p \frac{\mathbf{s}}{\sigma_{eq}} \quad ; \quad \dot{\varepsilon}_p = \sqrt{\frac{2}{3}\mathbf{d}^{PP} : \mathbf{d}^{PP}} \quad ; \quad \varepsilon_p = \int_t \dot{\varepsilon}_p dt \tag{3.16}$$

- *Thermal considerations*

The local form of the heat equation reads

$$\rho C_p \dot{T} - k\Delta T = \dot{Q} \tag{3.17}$$

where $\dot{T}$ is the time derivative of the temperature T and ΔT is the Laplacian of T . ρ ,C_p and k represent the mass density, the specific heat capacity and the thermal conductivity respectively.

In the present work, the heat generation due to tool-workpiece friction is not taken into account. The rate of heat generation $\dot{Q}$ in (3.17) coming from the plastic dissipation is assumed in the form

$$\dot{Q} = \beta\, \boldsymbol{\sigma} : \mathbf{d}^{PP} = \beta \sigma_y \dot{\varepsilon}^p \tag{3.18}$$

where β is the inelastic heat fraction, otherwise known as Taylor-Quinney coefficient in reference to [21], which represents the fraction of plastic work rate $\boldsymbol{\sigma} : \mathbf{d}^{PP}$ converted to heat. Combining (3.17) and (3.18) yields

$$\rho C_p \dot{T} - k\Delta T = \beta \sigma_y \dot{\varepsilon}^p \tag{3.19}$$

Two different cases of thermo-mechanical coupled analysis are considered here: full and weak coupling. Full coupling takes into account the heat conduction, as in (3.19), whereas the weak coupling assumes adiabatic conditions. In case of weak coupling (adiabatic conditions), the local form of the heat equation in (3.19) reduces to

$$\rho C_p \dot{T} = \beta \sigma_y \dot{\varepsilon}^p \tag{3.20}$$

- *Failure criterion*

A simple material failure criterion is used here which is given by a critical value of the equivalent plastic strain ε_p^{crit} above which the material fails. The failure of the material results numerically in the finite element deletion.

- *Friction at the work piece/tool interface*

Although the heat generated due to friction is not taken into account in the present parametric study, the mechanical contact at the tool-chip interface is simulated with the Coulomb friction law. The friction coefficient value is 0.5.

3.4.2 Numerical procedure

The numerical simulations are conducted using the commercial, explicit, finite element code Abaqus.

The geometry for the orthogonal machining set-up is adopted from [20] and is shown in Fig. 3.23 with a feed t_1 of 100µm. The important feature to note in this geometry is that the mesh of the workpiece is divided into three different zones: zone A which forms the chip, zone B the intermediate layer and zone C the workpiece base.

The work piece and the tool are meshed using

- CPE4RT plane strain 4-node finite element with reduced integration with temperature-displacement coupling in case of full coupling.
- CPE4R plane strain 4-node finite element with reduced integration with adiabatic condition in case of weak coupling.

The material of the work piece, namely Ti-6Al-4V titanium alloy, is assumed to obey Johnson-Cook constitutive law with the constants in Table 1 obtained from [20] where α is the thermal expansion coefficient and E the Young's modulus. Different values of ε_p^{crit} are assigned for each zone due to the variation of stress triaxiality involved in the different zones during HSM. Johnson-Cook model and shear failure criterion used in this work are those available in Abaqus standard library.

The tool material is CBN (Carbon-Boron-Nitride alloy) and is assumed to be rigid in the simulation.

The time integration scheme is explicit and the total time period depends on the cutting speed imposed on the tool. The boundary conditions are specified in Fig. 3.23. The initial temperature T_0 for both the tool and the workpiece was equal to 293 K.

Table 3.6 Constants of the Ti-6Al-4V titanium alloy under consideration. After [18].

A (MPa)	B (MPa)	n	C	m	$\dot{\varepsilon}_0$ (1/s)
782	498	0.28	0.028	1.0	10-5

k (W/mK)	C_p (J/kgK)	α (μm/mK)	T_m	ρ (kg/m3)	E (GPa)
7.2	560	9.2	1930	4420	114

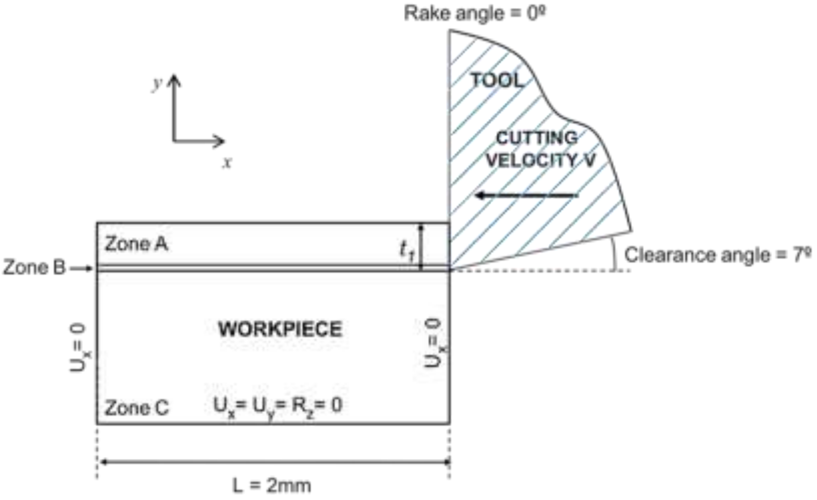

Fig. 3.23 High speed orthogonal machining configuration. After [18].

3.4.3 Parametric study

The numerical simulations are conducted considering cutting speeds ranging from 3m/s to 350m/s. According to [20] and [22], the numerical model described in Sections 3.4.1 and 3.4.2 above is well able to reproduce the experimental results in terms of cutting force, thrust force and shear band spacing. It is now required to analyse the robustness of this model by testing its dependency on certain constants which are chosen arbitrarily. Firstly, the interest of switching from full to weak thermo-mechanical coupling is explored. Then the influence of the critical plastic strain to failure and inelastic heat fraction on the chip morphology is studied.

(1) Full vs Weak thermo-mechanical coupling

The interest of switching from full to weak thermomechanical coupling would be to gain computational time. Also it seems reasonable to consider that as the cutting velocity increases, the conditions are near adiabatic due to the limited characteristic time of the process. Here, the chip morphology obtained from the simulation of full and weak coupling are compared with some experimental observations obtained in [17]. In this subsection, the values of ε^{p}_{crit} for the zones A, B and C are assumed to be 6, 3 and 3 respectively and β =0.9 which are close to the values found in [20].

A global view of the numerical simulation at a cutting velocity V of 3m/s in case of fully coupled analysis is shown in Fig. 3.24 at a given time during the machining process. The elements in the intermediate layer get deleted as the critical plastic strain is reached while the tool cuts through the workpiece. The top zone forms the chip which when closely observed shows mild serration in this case.

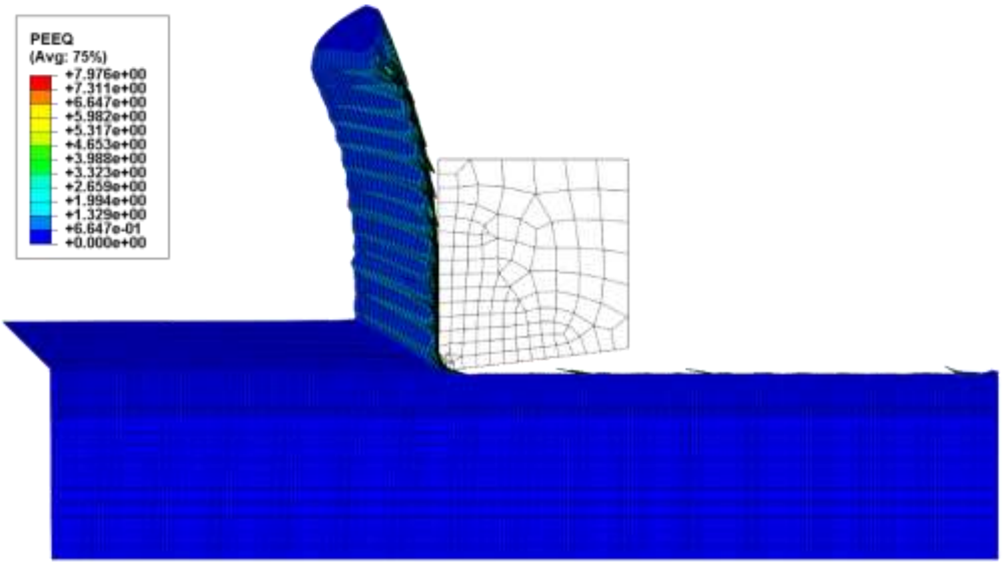

Fig. 3.24 Global view of the fully coupled analysis of orthogonal machining at V = 3m/s.

Local views of the chip during the machining process for cutting speeds of 5m/s, 31.2m/s and 350m/s in case of full and weak coupling are shown in Fig. 3.25.

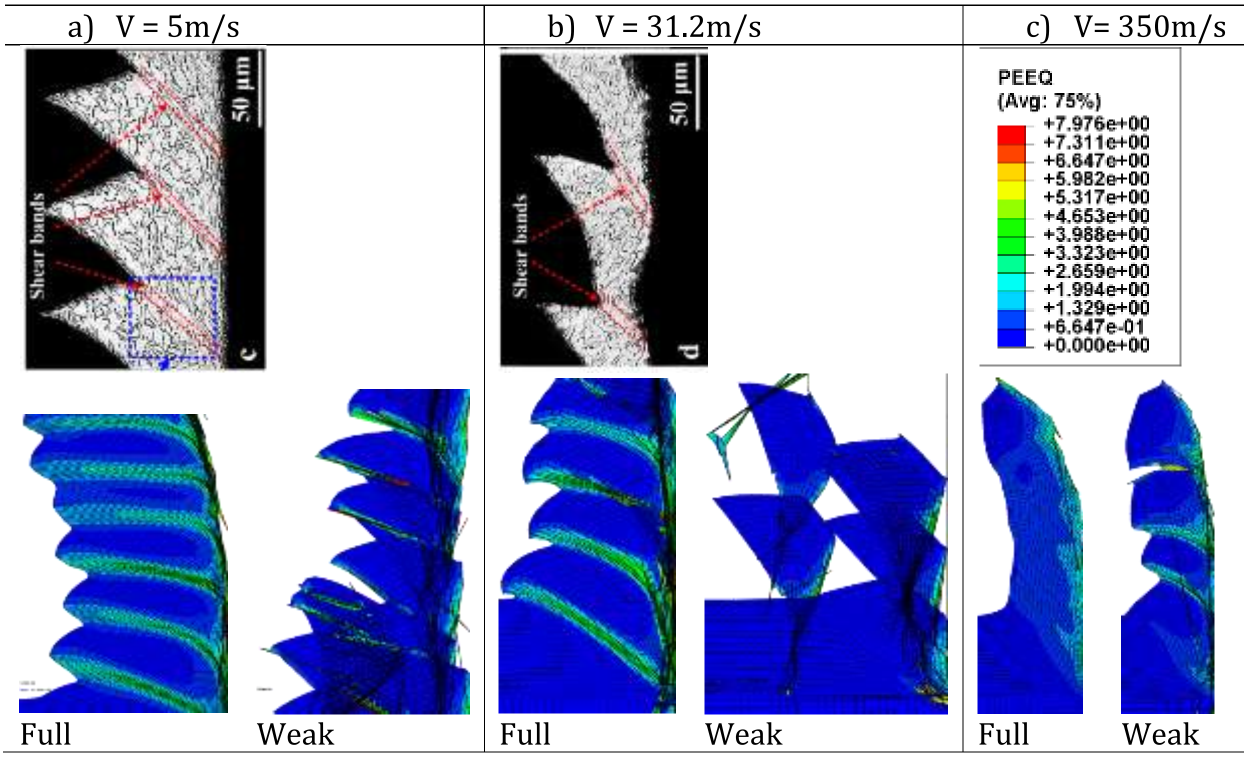

Fig. 3.25 Accumulated plastic strain ε_p map showing the chip morphology obtained from numerical simulation for full and weak coupling at cutting velocities of (a) V=5m/s (b) V=31.2m/s and (c) V=350m/s. Experimental chip micrograph after [17].

For a low cutting velocity of 5m/s which lies in the regime of conventional machining speed, the microstructure evidences the role of shear banding in chip serration, see Fig. 3.25a top. According to Fig. 3.25a bottom, the full coupling produces numerical serrated chips close to the experiment whereas in weak coupling the chip gets fragmented.

For a higher cutting velocity of 31.2 m/s which falls in the category of high speed machining, the microstructure shows almost fragmented chips along the shear bands with a small portion remaining intact, see Fig. 3.25b top. This result lies somewhat in between of what is observed of full and weak coupling, see Fig. 3.25b bottom.

A very high ballistic-like cutting speed of 350m/s is also explored which lacks experimental observations in literature. The simulation shows diffused high strain regions for the full coupling and shear localized, almost fragmented chips for weak coupling, see Fig. 3.25c. One could possible infer that the accuracy of the results with increase in cutting velocity increases while switching from full to weak coupling. However it needs to be backed by experimental evidence.

(2) Fracture criterion ε^{p}_{crit}

The critical plastic strain to failure is a constant chosen arbitrarily. Here the value of ε^{p}_{crit} on the different zones is varied to see if it significantly affects the chip form. At first the ε^{p}_{crit} of zones A and C i.e. the top and the base zones of the workpiece are kept constant at a value of 6 and 3 respectively and its value at the zone B or the intermediate layer is varied. The simulation results are shown in Fig. 3.26. It is seen that $\varepsilon^{p}_{crit} = 2$ yields almost a continuous chip, $\varepsilon^{p}_{crit} = 3$ shows the initiation of the chip serration and $\varepsilon^{p}_{crit} = 4$ shows shear localization.

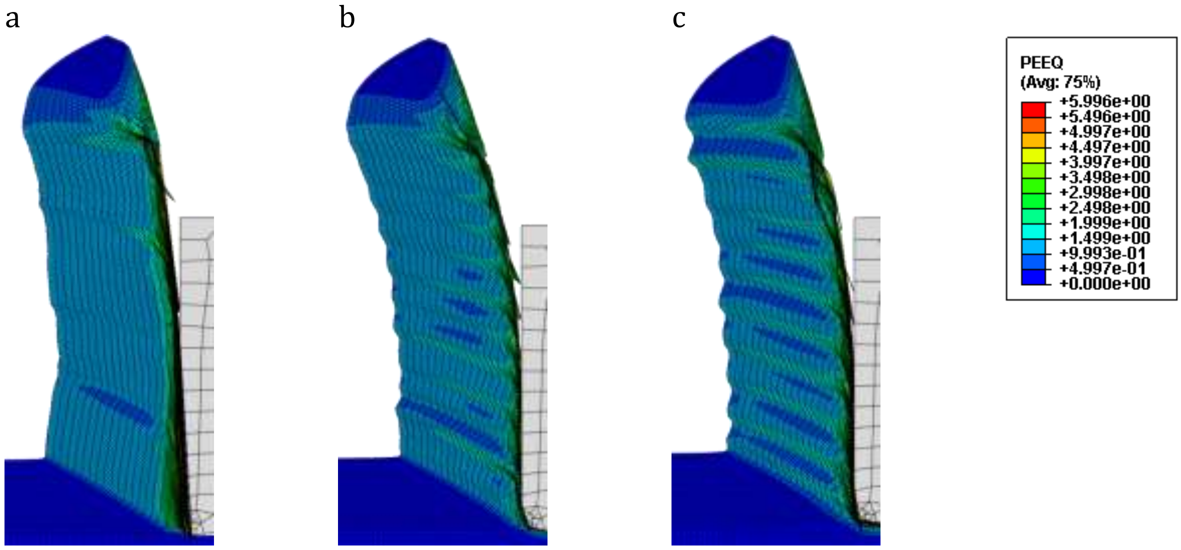

Fig. 3.26 Accumulated plastic strain ε_{p} map showing the chip morphology for varying ε^{p}_{crit} of the zone B a) $\varepsilon^{p}_{crit} = 2$, b) $\varepsilon^{p}_{crit} = 3$, c) $\varepsilon^{p}_{crit} = 4$

In Fig. 3.27, the ε^{p}_{crit} of the zone B is kept constant at 2 and its values for the zones A and C are varied equally. The trend shows that increasing values of ε^{p}_{crit} render more strain localized chips. Although this case does not exhibit much difference in the chip morphology, the previous case with the effect of the ε^{p}_{crit} of the intermediate layer is significant.

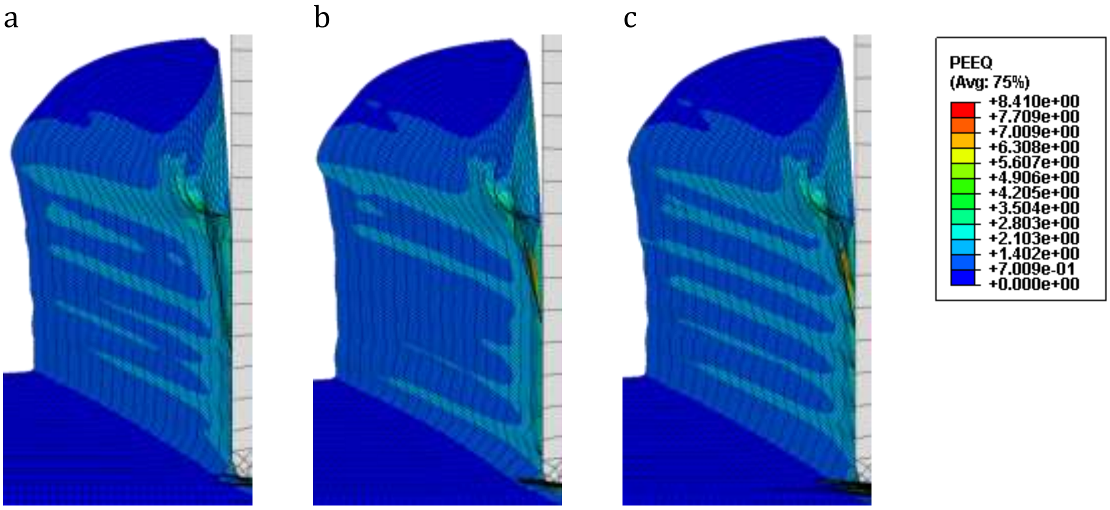

Fig. 3.27 Accumulated plastic strain ε_p map showing the chip morphology for varying ε^p_{crit} of the zones A and C a) ε^p_{crit} = 6, b) ε^p_{crit} = 8, c) ε^p_{crit} = 10

(3) Inelastic heat fraction β

The other arbitrary constant employed in this model is the Taylor and Quinney coefficient [21] or inelastic heat fraction β allowing for evaluating the plastic dissipation induced temperature rise, see (3.18). The typical value commonly used for β is 0.9. A parametric study is carried out here to see if the choice of the value of β is important. Numerical simulations are carried for β = 0.3, 0.6, 0.9 and for both strongly and weakly coupled cases. In Fig. 3.28, the results are displayed for some of the cases. The graphs in Fig. 3.29 show the shear band spacing vs β for strong and weak couplings. The band spacing equal to zero in the graphs implies that no shear bands were observed.

According to Fig. 3.28, for β = 0.3 no shear bands are seen in all the cases. At the very high cutting speed of 350 m/s, diffused strain localization was observed for all the values of β in the strongly coupled analyses. In all other cases, the general trend seen is that, with increasing value of β, i.e. more the proportion of plastic work converted to heat, more the chips show strain localization and chip segmentation.

These parametric studies clearly demonstrate that the level of the thermomechanical coupling (full vs weak) plays a significant role and that the values given to the constants ε^p_{crit} and β are significant and cannot be chosen arbitrarily.

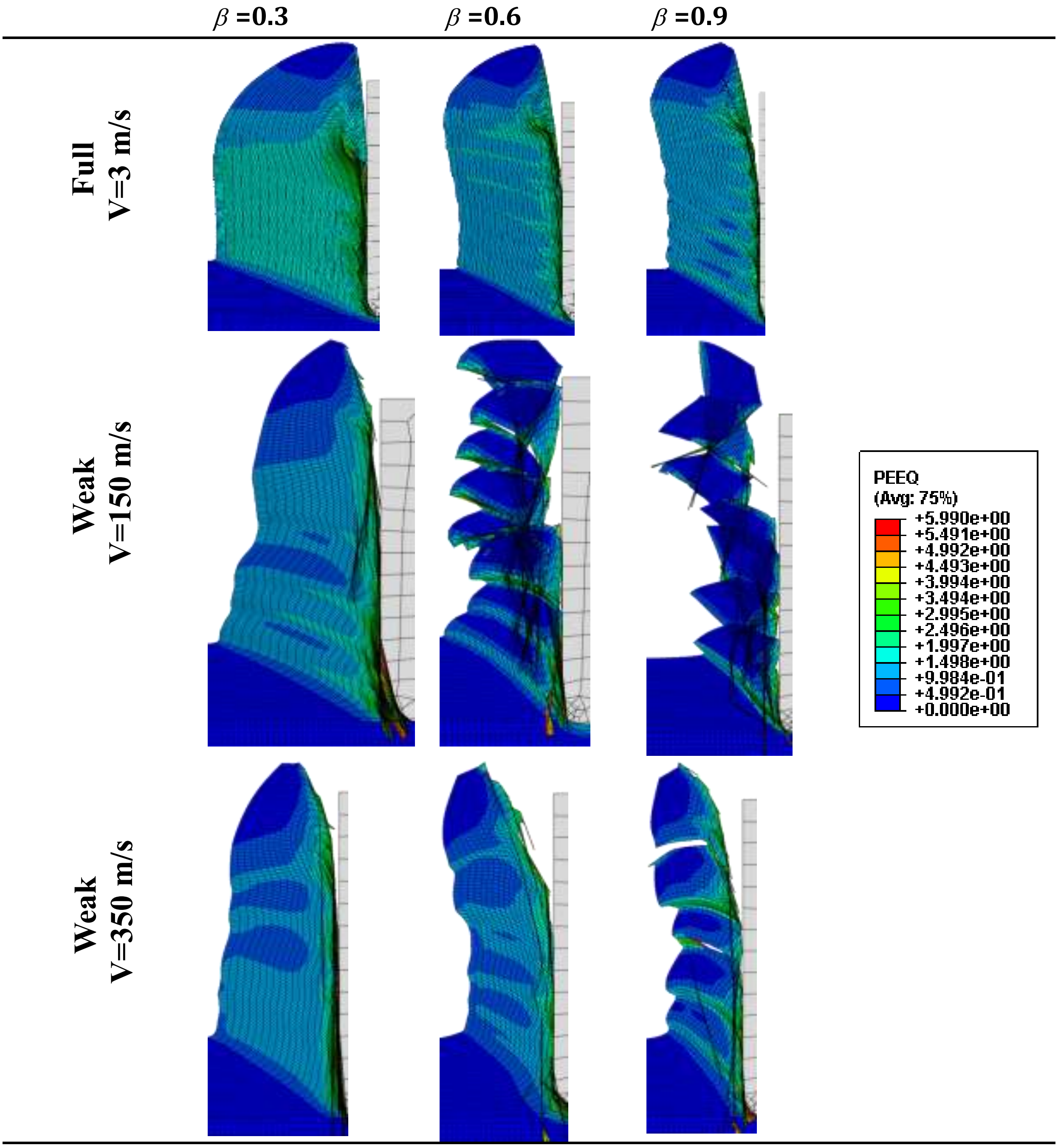

Fig. 3.28 Accumulated plastic strain ε_p map showing the chip morphology for varying β and cases of thermo-mechanical coupling.

3.4.4 Discussion

3.4.4.1 Assessment of the numerical simulations

It is deduced from the observations of the parametric study conducted in Section 3.4.3 that the chip morphology is strongly influenced by (i) the level of thermo-mechanical coupling (full vs weak), (ii) the method for evaluating the temperature rise (via β in (3.18)) and (iii) the value of the failure strain.

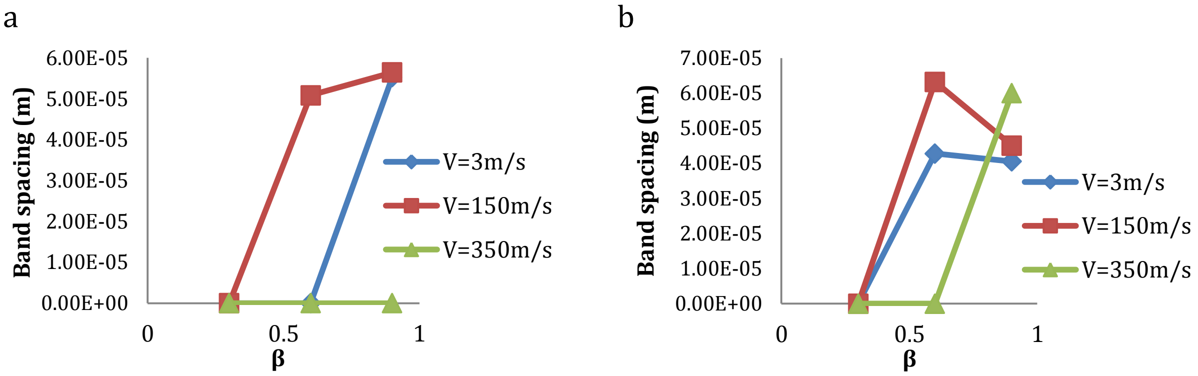

Fig. 3.29 Variation of shear banding spacing with β for (a) Full coupling (b) Weak coupling

3.4.4.2 Thermo-mechanical coupling

The fully and weakly coupled thermo-mechanical analyses options are readily available in the commercial finite element code Abaqus. A deeper evaluation of the computation code is required to understand the differences in the results obtained from the full and the weak coupling.

3.4.4.3 Evaluation of the temperature rise

It is important to accurately determine the self-heating due to plastic dissipation as the thermal softening plays a crucial role in the ASB incipience. While the β is assumed to be a constant in many studies, experimental results of e.g. Mason et al. [23] and theoretical studies of e.g. Longère and Dragon [9] show that it is, or may be, dependent on strain, strain rate and temperature, see discussion in Section 2.4.2.1.

An accurate knowledge of the softening mechanisms triggering ASBs is required, especially in Ti alloys for which a competition between thermal softening and DRX may take place, see [24], as mentioned in Section 2.4.2.2. It is also necessary to distinguish the conservative and dissipative mechanisms operating inside the material.

There is accordingly a need for a law governing the temperature rise which is consistent with the constitutive model and adapted to the mechanisms of deformation of the material under consideration.

3.4.4.4 From strain localization to failure

In the current (and usual) numerical simulations involving ASB and conducted in the context of the small scale postulate (the bandwidth covers several finite elements, implying that the bandwidth is greater than the finite element characteristic length) the softening regime leads to unregulated concentrations of high strain regions resulting from numerical instability, and not from material instability, accompanied by a pathological mesh size and orientation dependence.

As a consequence, the chip morphology induced by the finite element failure, conditioned by a constant critical value of the strain, as done in the present work, and not by a strain rate, stress triaxiality and temperature dependent value of the strain, as done in e.g. [10], is actually controlled by a numerical instability and not by a material instability.

A more realistic model would describe the thermo-viscoplasticity followed by controlled ASB induced strain localization and the subsequent micro-voiding in the wake of the ASB which ultimately fracture the material through the upper bound of the degradation variable giving rise to chips.

3.4.4.5 Proposition

There exists limitation of the options available in the standard library of the commercial FE computation codes. Therefore there is a requirement for an advanced model accounting for the coupled effects of dynamic plasticity with an inherent inelastic heat fraction, controlled strain localization and micro-voiding to be implemented as user material in the FE code.

An example of the constitutive model describing the aforementioned 'realistic' approach in the context of the large scale postulate (the band is embedded within the finite element, implying that the bandwidth is lower than the finite element characteristic length) would be the enlarged ASB+MV constitutive model detailed in Chapter 2.

The numerical implementation of this constitutive model on the high speed machining application is in progress.

3.5 CONCLUSION

The assessment of the numerical implementation of the developed constitutive model is considered here.

The interest of using the advanced model is demonstrated through a comparative study. Using the (1-D) type model to reproduce the complex ASB mechanism by a simple scalar isotropic damage variable presents the advantage of relatively simple implementation. However, the uncontrolled damage rate observed shows that this model requires an intrinsic control of the damage rate. Furthermore, this simple linear model is not predictive as it appears that the material related damage constant needs to be varied depending on the geometry of the structure and the loading analysed. On the other hand, the **D** type viscoplastic/visco-deterioration model is more adapted in describing the ASB induced material deterioration. The rate dependence of **D** provides a regularizing effect and thereby controls intrinsically its rate. In addition, as this model focuses on the predominant physics of the process, it describes the kinematic effects of the presence of the bands. It also accurately follows the V&V procedure and is consequently predictive.

The enriched model describing the adiabatic shear banding and micro-voiding mechanisms has been subjected to modifications in accordance with the physics of the shear localization and subsequent ductile damage process. The model performances are evaluated within a calibration procedure. Following this procedure, the model has been demonstrated to be numerically feasible at the representative volume element scale and also on a structural scale namely the hat shaped structure. The challenge remains to experimentally identify the micro-voiding related constants.

For the case of steel, two models have been compared on the HSS: one with effect of ASB only, the other with ASB and MV activated. Due to the additional deterioration mechanism of MV, the ASB+MV model shows increased drop in strength and accelerated propagation of ASB in the elements. At a given instant, not all elements containing ASB show MV. This implies that upon unloading it is possible for regions with ASB only to regain its strength on phase transformation and the deteriorated regions are limited only to the corner elements containing MV. For the case of Ti6Al4V, the influence of thermal and DRX induced softening on the ASB onset have been studied on HSS using two cases: DRX only and DRX+TS. The model with DRX+TS shows much earlier onset of ASB and consequently earlier onset of MV. Therefore neglecting either of the softening mechanisms would delay ASB initiation and underestimate the ASB propagation.

In order to complete the validation process, the model has to be evaluated on a complex initial boundary value problem such as high speed machining. The parametric study conducted using the conventional Johnson-Cook constitutive model demonstrates that the chip morphology during high speed machining is strongly influenced by (i) the level of thermo-mechanical coupling (full vs weak), (ii) the method for evaluating the temperature rise (via the inelastic heat fraction β often assumed to be constant) and (iii) the value of the failure strain. Two cases of thermo-mechanical coupled analyses are explored – strong coupling (with heat conduction) and weak coupling (adiabatic condition). At low cutting velocities, the strongly coupled analysis renders accurate outcome and at very high cutting velocities it is possible that the weakly coupled analysis is more accurate although it needs to be backed by experimental evidence. An alternative constitutive model accounting for dynamic plasticity, anisotropic strain localization and micro-voiding is suggested. The inelastic heat fraction is varying consistently with the material state. The numerical implementation of this model on HSM application is in progress.

3.6 REFERENCES

[1] P. Longère, A. Dragon, and X. Deprince, "Numerical Study of Impact Penetration Shearing Employing Finite Strain Viscoplasticity Model Incorporating Adiabatic Shear Banding," *ASME, J. Eng. Mater. Technol.*, vol. 131, no. 1, p. 011105.1-011105.14, 2009.

[2] J. F. Kalthoff and S. Winkler, "Failure mode transition at high rates of shear loading.," in *Impact Loading and Dynamic Behaviour of Materials*, Vol. 1., C. Y. Chiem, H.-D. Kunze, and L. W. Meyer, Eds. 1987, pp. 185–195.

[3] M. Zhou, A. J. Rosakiss, and G. Ravichandrans, "Dynamically propagating shear bands in impact-loaded prenotched plates-I. Experimental investigations of temperature signatures and propagation speed.," vol. 44, no. 6, pp. 981–1006, 1996.

[4] P. Longère, A. Dragon, H. Trumel, T. De Resseguier, X. Deprince, and E. Petitpas, "Modelling adiabatic shear banding via damage mechanics approach," *Arch. Mech.*, vol. 55, no. 1, pp. 3–38, 2003.

[5] L. M. Kachanov, "On the Time to Rupture under Creep Conditions," *Izv. Acad. Nauk SSSR, OTN*, vol. 8, pp. 26–31, 1958.

[6] J. Lemaitre, "A Continuous Damage Mechanics Model for Ductile Fracture," *J. Eng. Mater. Technol.*, vol. 107, pp. 83–89, 1985.

[7] M. Dolinski, D. Rittel, and A. Dorogoy, "Modeling adiabatic shear failure from energy considerations," *J. Mech. Phys. Solids*, vol. 58, no. 11, pp. 1759–1775, 2010.

[8] C. Mazeau, L. Beylat, P. Longere, and P. F. Louvigne, “On the quantitative evaluation of adiabatic shear banding sensitivity of various titanium alloys,” *J. Phys. IV JP*, vol. 07 (C3), pp. C3-429-C3-434, 1997.

[9] P. Longère and A. Dragon, “Inelastic heat fraction evaluation for engineering problems involving dynamic plastic localization phenomena,” *J. Mech. Mater. Struct.*, vol. 4, no. 2, pp. 319–349, 2009.

[10] P. Longère and A. Dragon, “Plastic work induced heating evaluation under dynamic conditions: Critical assessment,” *Mech. Res. Commun.*, vol. 35, no. 3, pp. 135–141, 2008.

[11] A. Marchand and J. Duffy, “An experimental study of the formation process of adiabatic shear bands in a structural steel,” *J. Mech. Phys. Solids*, vol. 36, no. 3, pp. 251–283, 1988.

[12] H. Couque, “A Hydrodynamic Hat Specimen to Investigate Pressure and Strain Rate Dependence on Adiabatic Shear Band Formation,” *J. Phys. IV. Fr.*, vol. 110, pp. 423–428, 2003.

[13] P. Longère, A. Dragon, H. Trumel, and X. Deprince, “Adiabatic shear banding-induced degradation in a thermo-elastic / viscoplastic material under dynamic loading,” *Int. J. Impact Eng.*, vol. 32, pp. 285–320, 2005.

[14] D. Rittel, P. Landau, and A. Venkert, “Dynamic Recrystallization as a potential cause for adiabatic shear failure,” *Phys. Rev. Lett.*, vol. 101, no. 165501, 2008.

[15] S. Osovski, D. Rittel, and A. Venkert, “The respective influence of microstructural and thermal softening on adiabatic shear localization,” *Mech. Mater.*, vol. 56, pp. 11–22, 2013.

[16] D. Umbrello, “Finite element simulation of conventional and high speed machining of Ti6Al4V alloy,” vol. 196, pp. 79–87, 2008.

[17] G. G. Ye, S. F. Xue, M. Q. Jiang, X. H. Tong, and L. H. Dai, “Modeling periodic adiabatic shear band evolution during high speed machining Ti-6Al-4V alloy,” *Int. J. Plast.*, vol. 40, pp. 39–55, 2013.

[18] S. Seo, O. Min, and H. Yang, “Constitutive equation for Ti – 6Al – 4V at high temperatures measured using the SHPB technique,” *Int. J. Impact Eng.*, vol. 31, pp. 735–754, 2005.

[19] M. Calamaz, D. Coupard, and F. Girot, “A new material model for 2D numerical simulation of serrated chip formation when machining titanium alloy Ti – 6Al – 4V,” *Int. J. Mach. Tools Manuf.*, vol. 48, pp. 275–288, 2008.

[20] A. Molinari, X. Soldani, and M. H. Miguélez, “Adiabatic shear banding and scaling laws in chip formation with application to cutting of Ti-6Al-4V,” *J. Mech. Phys. Solids*, vol. 61, no. 11, 2013.

[21] G. I. Taylor and H. Quinney, “The latent energy remaining in a metal after cold working,” *Proc. R. Soc. London. Ser. A*, vol. 143: 849, pp. 307–326, 1934.

[22] M. H. Miguélez, X. Soldani, and A. Molinari, “Analysis of adiabatic shear banding in orthogonal cutting of Ti alloy,” *Int. J. Mech. Sci.*, vol. 75, pp. 212–222, 2013.

[23] J. J. Mason, A. J. Rosakis, and G. Ravichandran, “On the strain and strain rate dependence of the fraction of plastic work converted to heat: an experimental study using high speed infrared detectors and the Kolsky bar,” *Mech. Mater.*, vol. 17, no. 2–3, pp. 135–145, 1994.

[24] P. Longère, “Respective/combined roles of thermal softening and dynamic recrystallization in adiabatic shear banding initiation,” *Mech. Mater.*, vol. 117, pp. 81–90, 2018.

Blank Page

4 CONCLUSION

4.1 RESULTS VS CHALLENGES

The realistic description of initiation and propagation of adiabatic shear bands and micro-voids (ASB+MV) and their consequences on the structural material in a wide range of situations implies modelling as close as possible to the complex physics of the mechanisms while being tractable and applicable to initial boundary value problems. In this context, a physics motivated phenomenological model describing the ASB induced degradation and kinematics in the framework of large scale postulate was initially developed by Longère et al. [1] and applied to IBVP in [2],[3]. This model required enrichment in terms of taking into account the micro-mechanisms that operate in the late pre-failure stage for (at least) two reasons: first, experimental evidence showed the presence of micro-voids in the wake of the ASB, with ASB and micro-voiding being two different softening mechanisms from the physics perspective, the former preserving matter cohesion whereas the latter causes internal surface separation; secondly, considering indistinctly the two aforementioned mechanisms does not allow for estimating the residual state of the material after unloading in terms of potentially recovered and irreversibly damaged zones. Hence, the existing ASB constitutive model was conceptually enriched to comprise the additional void-growth induced degradation [4].

This enlarged ASB+MV model is revisited here and has been subjected to modifications in accordance with the physics of the shear localization and subsequent ductile damage process. The two main effects of ASB+MV induced deterioration reproduced by the unified model in the framework of irreversible thermodynamics are: material consequence, viz. anisotropic deterioration of the material strength; and kinematic consequence, viz. progressive deviation of the plastic flow in the band plane and according to the micro-void orientation. It is to be noted that this model considers the anisotropy of the strongly oriented ASB+MV through the use of second order tensor deterioration variables. The ASB incipience criteria used is the one originally obtained from linear perturbation method. The influence of the softening mechanisms such as thermal softening and DRX induced softening on the ASB onset is also considered here. The MV incipience is tentatively treated using an arbitrary value of critical local energy release rate.

The interest of using the advanced model is demonstrated through a comparative modelling and simulation. The first, engineering-oriented approach considered is termed as (1-*D*) type model and uses a scalar isotropic damage-like variable *D* to describe the ASB induced deterioration. The second approach considered is the basic version of the present physics motivated model termed as the **D** type model which describes the ASB induced deterioration without distinguishing the micro-voiding contribution. The (1-*D*) type model was numerically implemented as VUMAT in Abaqus; the experimental and simulation results for **D** type model were obtained from [1], [2] and [3]. It was demonstrated that (1-*D*) type model presents the advantage of relatively simple implementation, however it showed uncontrolled damage rate. Furthermore, this simple linear model is not predictive as it appears that the material related damage constant needs to be varied depending on the structure, geometry and loading analysed. On the other hand, the **D** type viscoplastic/visco-deterioration model is more adapted in describing the ASB induced material deterioration. The rate dependence of **D** provides a regularizing effect and thereby controls intrinsically its rate. In addition, as this model focuses on the predominant physics of the process, it describes the kinematic effects of the presence of the bands. It also accurately follows the verification & validation procedure, i.e. it requires a unique set of material constants for a given material whatever the configuration, and is consequently predictive.

Many approaches describing the ASB in the literature are developed in the small scale postulate. However, as the ASB width in itself is of the order of micro-meters, this postulate requires the use of very fine meshing in the finite element (FE) simulations. Whereas in the current approach, the large scale postulate adopted, facilitates the use of coarser meshes in FE simulations and thus makes the model feasible to implement on engineering structural applications. Mesh dependency study of the basic **D** type model had been conducted by Longère et al. in [2] which is reasonably assumed valid for the ASB+MV model too. The large scale postulate requires the ASB to be embedded within the finite element which in turn implies that it is not feasible to use mesh of any given size. It was shown that a mesh size of approximately five times the shear band (~500μm for high strength steel) width satisfies the scale postulate. A very coarse meshing would give rise to a dispersed area of deteriorated finite elements.

The numerical instability the finite element computation code is subject to in the softening regime has been overcome by the following means. Firstly, the viscosity (viscoplasticity and visco-deterioration) of the model helps in regularizing the boundary value problem. Secondly, the strong localization induced by ASB required complementary procedure to be applied to overcome the numerical instability, for which an adaptive time step procedure is followed. In this procedure, a sampling of the global time increment is carried out after the ASB onset to obtain a local time increment for integrating the constitutive equations which reinforces the numerical stability.

The present enlarged ASB+MV model is then numerically implemented as user material in the engineering finite element code LS-DYNA. Due to the lack of experimental data to distinguish and separately identify the ASB and MV related constants, arbitrary constants are tentatively employed here in such a way as to exaggerate the MV effects for the purpose of visualization. The enriched model performances are evaluated within a calibration procedure based on the Verification and Validation (V&V) procedure. The V&V would require identifying the deterioration related constants; instead, following the principle of this procedure, the model has been successfully demonstrated to be numerically feasible at the representative volume element scale and also on a structure namely the hat shaped structure (HSS). The qualitative analysis of the ASB+MV model is done by comparing with ASB only model in which the MV is deactivated while maintaining the ASB related constants. On the scale of the RVE, the ASB+MV model demonstrates the desired behaviour by showing supplementary MV induced material deterioration and kinematics. On the HSS, it is observed that the presence of MV accelerates the propagation of ASB, see Fig 3.20, which has not been shown in literature and thus constitutes a novel result. Also, at a given instant, not all elements containing the ASB reach the criteria for MV onset; only the corner elements show the presence of MV. One could infer the following possible scenarios from the given state of elements on unloading: the material within the ASB might recover its initial properties after being quenched by the surrounding material and thus phase transformed leaving only the effect of MV in the respective elements in the corners; or the cooling on unloading might cause micro-cracking within the ASB leading to complete fracture. The respective influence of thermal softening and dynamic recrystallization (DRX) induced softening is also studied on the RVE and structural scale. In both the cases it is shown that the combined contribution of thermal and DRX softening brings about an earlier ASB onset as expected. Considering only one of the softening mechanisms would delay the ASB onset and underestimate the ASB propagation, which is in contradiction with some assumptions in literature considering that DRX is the unique mechanism controlling the ASB onset particularly in Ti-6Al-4V titanium alloy.

The calibration procedure also requires testing the model on a complex initial boundary (IBVP) value problem for which high speed machining (HSM) application is considered. An initial parametric study is conducted in Abaqus using the conventional Johnson-Cook model so as to demonstrate the deficiency of the conventional approaches to simulate the HSM process showing ASB. The study concluded that the chip morphology during HSM is strongly influenced by (i) the level of thermo-mechanical coupling (full vs weak), (ii) the method for evaluating the temperature rise (via the inelastic heat fraction β often assumed to be constant) and (iii) the value of the failure strain. Two cases of thermo-mechanical coupled analyses are explored – strong coupling (with heat conduction) and weak coupling (adiabatic condition). At low cutting velocities, the strongly coupled analysis renders accurate outcome and at very high cutting velocities it is possible that the weakly coupled analysis is more accurate although it needs to be backed by experimental evidence. The alternative constitutive model i.e. the present ASB+MV model accounting for dynamic plasticity, anisotropic yielding induced by strain localization and micro-voiding is proposed in which the inelastic heat fraction is varying consistently with the material state. The numerical implementation of the ASB+MV model on HSM application is in progress.

4.2 FUTURE WORK

There are still certain challenges that remain which are stated below and some propositions are made for the future works in terms of experiments, modelling and simulations.

4.2.1 Experiments

The challenge still remains in terms of identifying the instant of MV incipience from experiments and hence to distinguish ASB and MV related material constants. The entire duration of the tests in the Hopkinson pressure bar set-up is of the order of tens of μs and therefore it would be challenging to carry out interrupted tests. One of the suggested ways to carry out interrupted tests on the HSS is by using stopper rings behind the specimen as done by Xing et al. [5] shown in Fig. 4.1

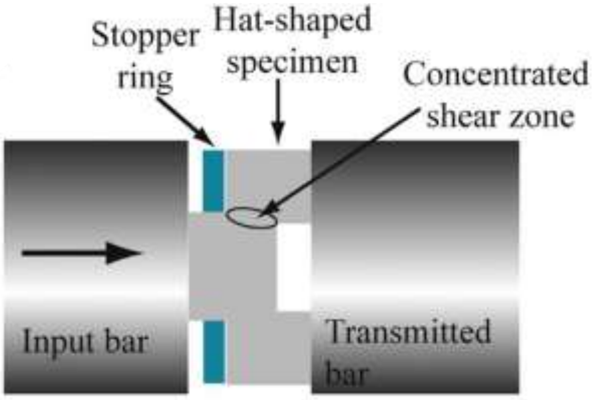

Fig. 4.1 Stopper rings used behind a HSS to carry out interrupted tests in a Hopkinson bar setup. After [5]

The post mortems of the specimens from the tests interrupted at various instants could be examined for micro-voids in the ASB wake and the instant of MV incipience could be inferred. For the post mortem specimen observation, X-ray computed tomography (XCT) could be employed. When compared to scanning electron microscope, the XCT is a non-destructive 3D technique capable of resolving internal structure with micron resolution, and does not require tedious sample preparation, see [6]. With XCT, void shape and size distributions, and interface structures can be revealed. For example, the stages of reconstruction of the 3D images of a specimen by Zabler et al. [7] using XCT are shown in Fig. 4.2. In Fig. 4.2c, the red regions indicate porosity and a macro-crack formed after strong deformation and yellow regions indicate dense mineral particles which reveal a healed crack.

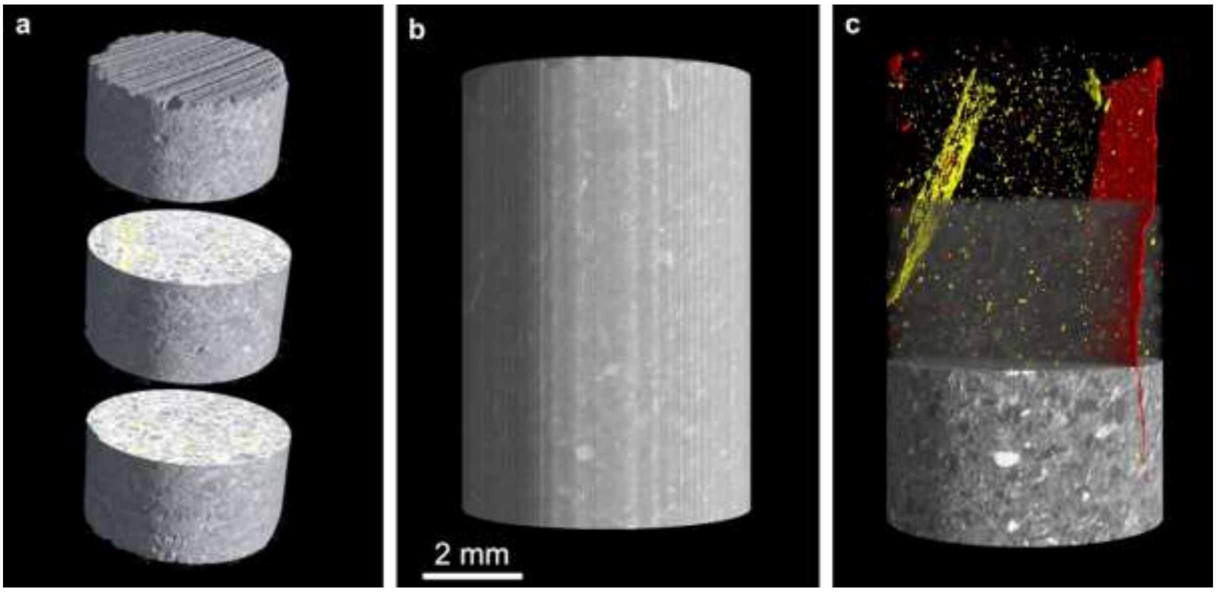

Fig. 4.2 After [7]. a) Virtual assembly of 3 tomograms to map the entire height of the sample. b) Assembled dataset c) Reconstruction of linear absorption coefficients allows grains and phases to be distinguished.

As impact tests are characterized by exceptionally short durations and very high strain rates, it is not yet possible to use in situ XCT, which is why the XCTs are generally confined to pre-test and post mortem analysis. However, modern X-ray imaging techniques have been developed for studies of dynamical phenomena , see [8], with spatial resolution ranging from a few micrometres to tens of nanometres, and temporal resolution ranging from a millisecond to hundreds of picoseconds. Using such advanced techniques, it would be possible to acquire real time images of the specimen during the dynamic test and the instant of the MV incipience could be accurately identified. Once this hurdle is overcome, the ASB and MV related deterioration constants could be distinguished.

Another experimental campaign proposed is related to high speed machining in the unexploited very high range of cutting speeds of the order of 100m/s and higher. The dynamics of the chip formation and the predominant mechanisms in Ti-6Al-4V or other metal alloys susceptible to ASB at such extreme cutting velocities could be explored. The experimental results could also be used to validate the ASB+MV model at very high cutting velocity ranges. Such high cutting speeds cannot be achieved using conventional machining tools. For that purpose, a ballistic set-up similar to the one designed by Sutter and List [9], as shown in Fig. 4.3 could be adopted. The ballistic device consists of launching the workpiece by means of a gas gun trough a launch tube onto two cutting tools. Strain gauges on the load sensor record the axial cutting forces. A high speed camera could be used to record the chip formation.

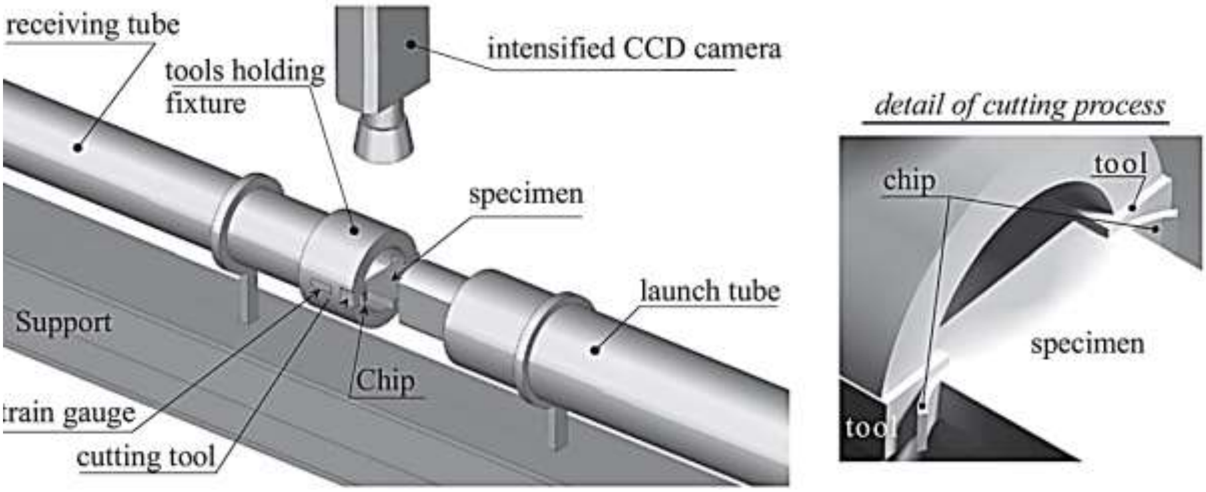

Fig. 4.3 After [9]. Ballistic cutting set-up.

4.2.2 Modelling

Certain aspects of the constitutive model could be further improved and some additional physics of the mechanisms could be taken into account.

Firstly, the orientation of the micro-voids is considered. In the present study, for the sake of simplicity, the MV is assumed to be oriented in the same direction as that of the ASB. The microscopic observation of ASB by Peirs et al. [10] in the gauge section of the impacted hat shaped specimens showed the following stages of formation of micro-cracks as shown in Fig. 4.4:

(a) The grains within the ASB are initially undeformed.
(b) The grains elongate and rotate under deformation. Micro-cracks are formed in in the same orientation as that of the elongated grains.
(c) Several micro-cracks are linked together to form cracks.

The different possible orientation of the MV with respect to that of the ASB has to be taken into account in future works by using different orientation tensors for ASB and MV which may pose other issues on objective derivatives (spin to be considered).

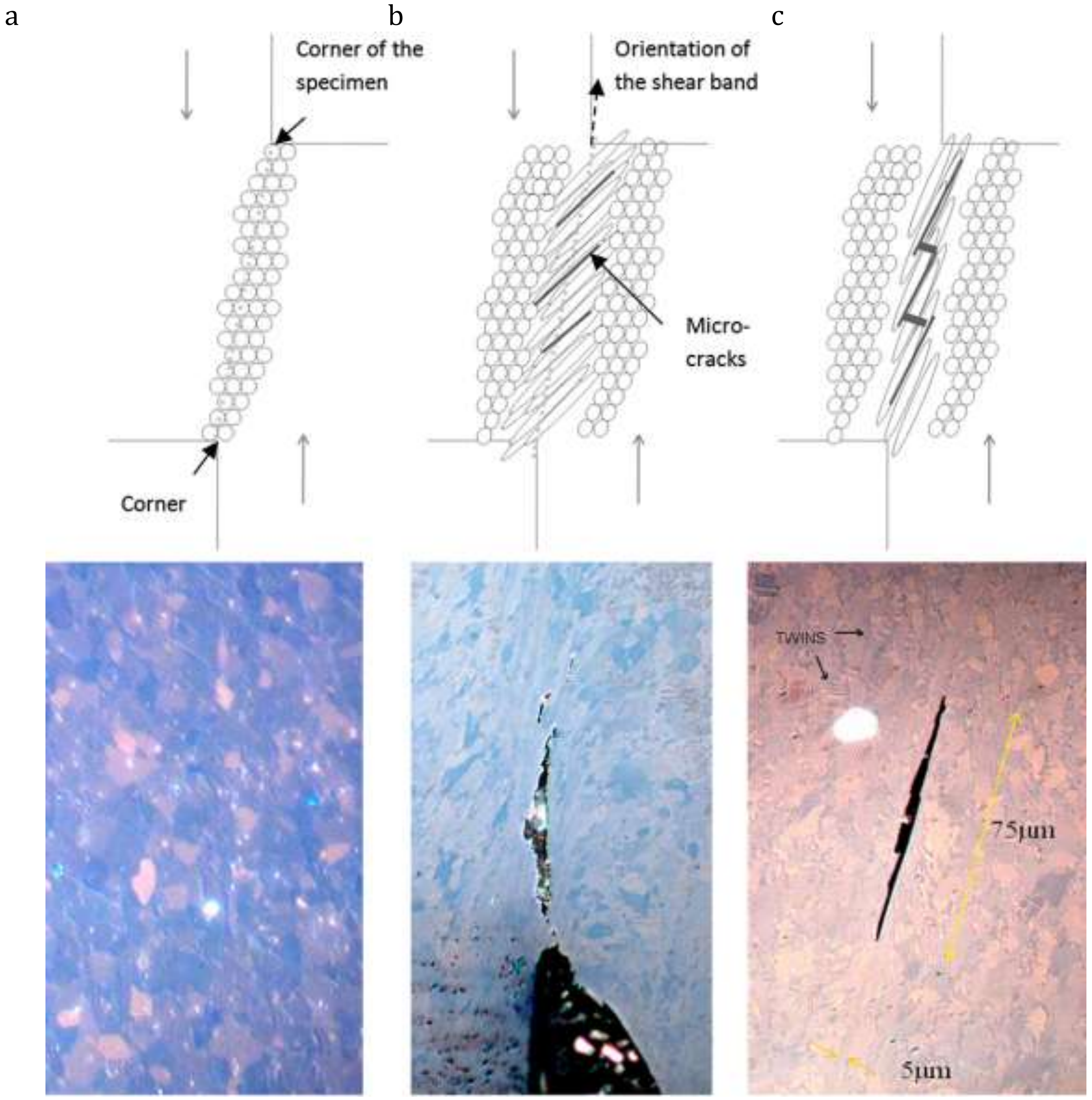

Fig. 4.4 Schematic representation and micrographic observation of micro-cracks evolution within ASB. After [10]. a) Grains are initially undeformed. b) Micro-cracks oriented as the elongated and rotated grains under deformation. c) Linked micro-cracks.

The phase transformation of the ASB is another feature which needs to be taken into account in the future works. Two types of bands are distinguished especially in steels – deformed and transformed bands. The deformed bands are often found to occur as precursor bands to the transformed bands which frequently follow when the strain rate is sufficiently high as shown in Fig. 4.5, refer [11]. The high temperature during the adiabatic shear deformation causes austenitization of the sheared zone in steels. On unloading, this zone is quenched by the surrounding metal forming martensite which has the characteristic white etched region.

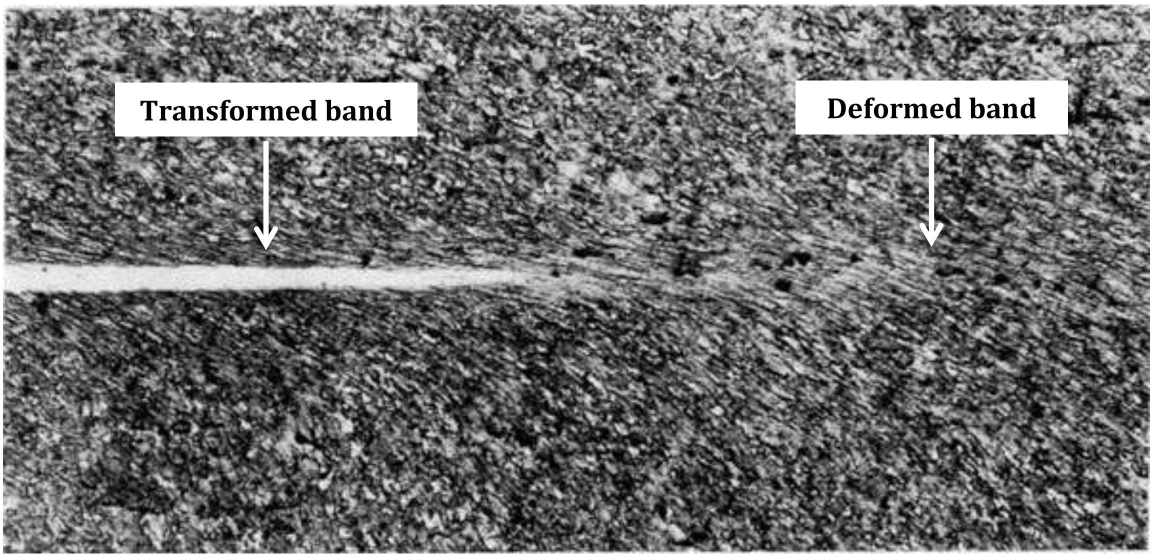

Fig. 4.5 White-etching transformed shear band preceded by deformed shear band in AISI 1040 steel. After [11].

The micro-hardness measured along the longitudinal direction of the ASB in Fig. 4.5 is shown in Fig. 4.6a. It is seen that there is maximum constant hardness along the transformed band whereas the hardness decreases in the deformed band region. In Fig. 4.6b, along the transverse direction of the transformed and deformed band in 1040 steel and purely deformed band in 304 and 1018 steels, the micro-hardness profile shows that the transformed band is much harder that the deformed band and also the surrounding matrix material.

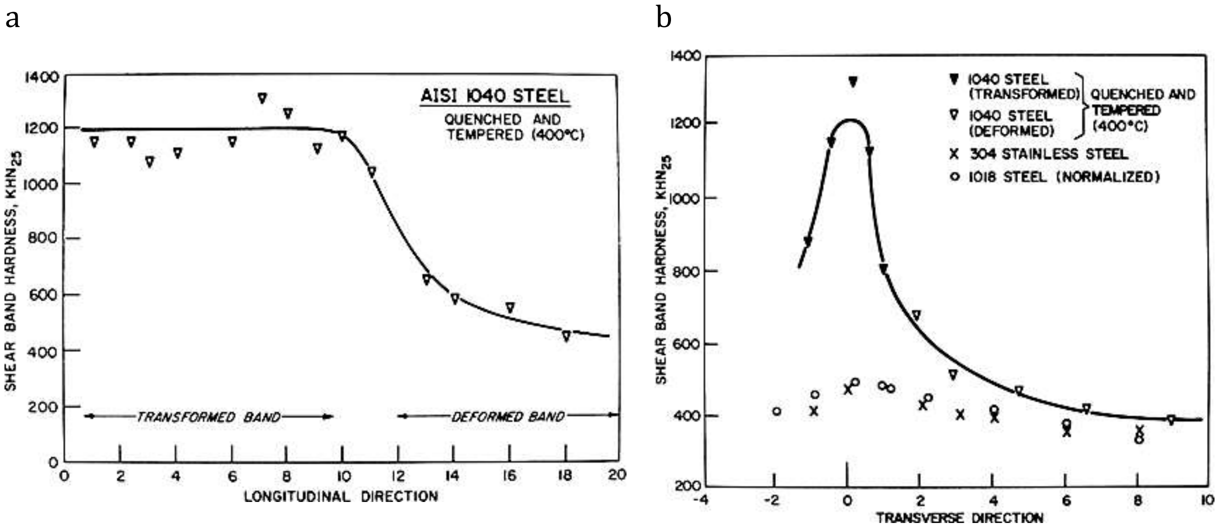

Fig. 4.6 After [11]. Micro-hardness profile of ASB along a) the longitudinal direction in 1040 steel b) the transverse direction in several steels.

This implies that the phase transformed band is considerable stronger than the surrounding zones at room temperature but also brittle and therefore it may contain micro-cracks. Thus it is essential to model the phase transformed bands and to recognize the conditions leading up to the phase transformation.

The incipience of ASB in itself need not be considered as a failure criterion from an engineering point of view as it would prove to be extremely conservative. This is because, the material still has the load bearing ability after the ASB onset and furthermore, after an impact load, the material within the band may be phase transformed and regain its original strength.

4.2.3 Numerical Simulations

Once the experimental challenge is overcome and the material constants relative to ASB and MV are identified, it is imperative to carry the ASB+MV model through the actual V&V procedure in order to prove that the model is predictive and reliable.

As the feasibility of the enlarged model has been demonstrated in the present study on an RVE scale and a relatively simple IBVP namely the HSS, it is now required to implement the model on the complex IBVP of HSM. This is ongoing work with challenges involving transferring an available HSM model from Abaqus/CAE to LS-DYNA and making it operational.

A upper bound of $\mathcal{D}$ which depends on the material properties exists, but would be an exaggerated value of failure criterion for a structural design and would also render extreme element distortions in numerical simulations. In the present work an upper limit for $Tr\mathbf{D}$ is imposed in the simulations as a criterion for element deletion. The model could be improved with actual simulations of crack propagation by using enriched FEM, e.g. X-FEM or E-FEM, see [12] and [13] respectively.

4.3 REFERENCES

[1] P. Longère, A. Dragon, H. Trumel, T. De Resseguier, X. Deprince, and E. Petitpas, “Modelling adiabatic shear banding via damage mechanics approach,” *Arch. Mech.*, vol. 55, no. 1, pp. 3–38, 2003.

[2] P. Longère, A. Dragon, and X. Deprince, “Numerical Study of Impact Penetration Shearing Employing Finite Strain Viscoplasticity Model Incorporating Adiabatic Shear Banding,” *ASME, J. Eng. Mater. Technol.*, vol. 131, no. 1, p. 011105.1-011105.14, 2009.

[3] P. Longère, A. Dragon, H. Trumel, and X. Deprince, “Adiabatic shear banding-induced degradation in a thermo-elastic / viscoplastic material under dynamic

loading," *Int. J. Impact Eng.*, vol. 32, pp. 285–320, 2005.

[4] P. Longere and A. Dragon, "Enlarged finite strain modelling incorporating adiabatic shear banding and post-localization microvoiding as shear failure mechanisms," *Int. J. Damage Mech.*, pp. 1–28, 2016.

[5] J. Xing, F. Yuan, and X. Wu, "Enhanced quasi-static and dynamic shear properties by heterogeneous gradient and lamella structures in 301 stainless steels," *Mater. Sci. Eng. A*, vol. 680, pp. 305–316, Jan. 2017.

[6] T. Li, D. Fan, L. Lu, J. Y. Huang, J. C. E, F. Zhao, M. L. Qi, T. Sun, K. Fezzaa, X. H. Xiao, X. M. Zhou, T. Suo, W. Chen, Y. L. Li, M. H. Zhu, S. N. Luo, "Dynamic fracture of C/SiC composites under high strain-rate loading: Microstructures and mechanisms," *Carbon N. Y.*, vol. 91, pp. 468–478, 2015.

[7] S. Zabler, A. Rack, I. Manke, K. Thermann, J. Tiedemann, N. Harthill, H. Riesemeier, "High-resolution tomography of cracks, voids and micro-structure in greywacke and limestone," *J. Struct. Geol.*, vol. 30, no. 7, pp. 876–887, 2008.

[8] "Advanced Photon Source - Imaging," Argonne National Laboratory,." [Online]. Available: https://www.aps.anl.gov/Imaging.

[9] G. Sutter and G. List, "Very high speed cutting of Ti-6Al-4V titanium alloy - Change in morphology and mechanism of chip formation," *Int. J. Mach. Tools Manuf.*, vol. 66, pp. 37–43, 2013.

[10] J. Peirs, P. Verleysen, J. Degrieck, and F. Coghe, "The use of hat-shaped specimens to study the high strain rate shear behaviour of Ti – 6Al – 4V," *Int. J. Impact Eng.*, vol. 37, no. 6, pp. 703–714, 2010.

[11] H. C. Rogers and C. V. Shastry, "Material Factors in Adiabatic Shearing in Steels," in *Shock Waves and High-Strain -Rate Phenomena in Metals - Concepts and Applications*, Plenum Pre., M. A. Meyers and L. E. Murr, Eds. 1981, pp. 285–298.

[12] P. M. A. Areias and T. Belytschko, "Two-scale method for shear bands: Thermal effects and variable bandwidth," *Int. J. Numer. Methods Eng.*, vol. 72, pp. 658–696, 2007.

[13] H. M. Mourad, C. A. Bronkhorst, V. Livescu, J. N. Plohr, and E. K. Cerreta, "Modeling and simulation framework for dynamic strain localization in elasto-viscoplastic metallic materials subject to large deformations," *Int. J. Plast.*, vol. 88, pp. 1–26, 2017.

Bibliography

Advanced Photon Source - Imaging, Argonne National Laboratory, [WWW Document], n.d. URL https://www.aps.anl.gov/Imaging

Anand, L., Kim, K.H., Shawk, T.G., 1987. Onset of shear localization in viscoplastic solids. J. Mech. Phys. Solids 35, 407–429.

Andrews, W.S., 2003. Depleted Uranium on the battlefield. Can. Mil. J. 41–46.

Areias, P.M.A., Belytschko, T., 2007. Two-scale method for shear bands: Thermal effects and variable bandwidth. Int. J. Numer. Methods Eng. 72, 658–696. https://doi.org/10.1002/nme

Bai, Y.L., Dodd, B., 1992. Adiabatic shear localization. Pergamon Press, Oxford.

Bao, Y., Wierzbicki, T., 2004. On fracture locus in the equivalent strain and stress triaxiality space. Int. J. Mech. Sci. 46, 81–98. https://doi.org/10.1016/j.ijmecsci.2004.02.006

Becker, R., Needleman, A., Richmond, O., Tvergaard, V., 1988. Void Growth and Failure in Notched bars. J. Mech. Phys. Solids 36, 317–351.

Bonnet-Lebouvier, A., Molinari, A., Lipinski, P., 2002. Analysis of the dynamic propagation of adiabatic shear bands. Int. J. Solids Struct. 39, 4249–4269.

Cai, S.L., Dai, L.H., 2014. Suppression of repeated adiabatic shear banding by dynamic large strain extrusion machining. J. Mech. Phys. Solids 73, 84–102. https://doi.org/10.1016/j.jmps.2014.09.004

Calamaz, M., Coupard, D., Girot, F., 2008. A new material model for 2D numerical simulation of serrated chip formation when machining titanium alloy Ti – 6Al – 4V. Int. J. Mach. Tools Manuf. 48, 275–288. https://doi.org/10.1016/j.ijmachtools.2007.10.014

Cho, K., Lee, S., Nutt, S.R., Duffy, J., 1993. Adiabatic Shear Band Formation during Dynamic Torsional Deformation of an HY-100 Steel. Acta Metall. Mater. 41, 923–932.

Chu, C.C., Needleman, A., 1980. Void Nucleation Effects in Biaxially Stretched Sheets. J. Eng. Mater. Technol. 102, 249–256. https://doi.org/10.1115/1.3224807

Couque, H., 2003. A Hydrodynamic Hat Specimen to Investigate Pressure and Strain Rate Dependence on Adiabatic Shear Band Formation. J. Phys. IV. Fr. 110, 423–428.

Dolinski, M., Rittel, D., Dorogoy, A., 2010. Modeling adiabatic shear failure from energy considerations. J. Mech. Phys. Solids 58, 1759–1775. https://doi.org/10.1016/j.jmps.2010.08.007

Dorothy, H.L., Longère, P., Dragon, A., 2017a. Coupled ASB-and-microvoiding-assisted dynamic ductile failure. Procedia Eng. 197, 60–68. https://doi.org/10.1016/j.proeng.2017.08.082

Dorothy, H.L., Longère, P., Dragon, A., 2017b. Modelling of high strain rate failure under ASB and microvoiding. Procedia Eng. 173, 593–600. https://doi.org/10.1016/j.proeng.2016.12.107

Duan, C.Z., Zhang, L.C., 2012. Adiabatic shear banding in AISI 1045 steel during high speed machining: Mechanisms of microstructural evolution. Mater. Sci. Eng. A 532, 111–119. https://doi.org/10.1016/j.msea.2011.10.071

Geffroy, A.-G., 2010. Modélisation numérique de la rupture de structures navales sous l ’effet d ’explosions au contact. Université de Bretagne-Sud.

Gooch, W.A., 2010. The Design and Application of Titanium Alloys to U . S . Army Platforms -2010. Titan. 2010 nternational Titan. Assoc.

Goods, S.H., Brown, L.M., 1979. The Nucleation of Cavities by Plastic Deformation. Acta Metall. 27, 1–15.

Halm, D., Dragon, A., 1996. A Model of Anisotropic Damage by Mesocrack Growth; Unilateral Effect. Int. J. Damage Mech. 5, 384–402.

Hancock, J.W., Mackenzie, A.C., 1976. HIGH-STRENGTH STEELS SUBJECTED TO MULTI-AXIAL mean stress. j. Mech. Phys. Solids 24, 147–169.

Hartley, K.A., Duffy, J., Hawley, R.H., 1987. Measurement of the Temperature Profile During Shear Band Formation in Steels Deforming At High-Strain Rates. J. Mech. Phys. Solids 35, 283–301. https://doi.org/10.1016/0022-5096(87)90009-3

Jacques, N., Mercier, S., Molinari, A., 2012. Effects of microscale inertia on dynamic ductile crack growth. J. Mech. Phys. Solids 60, 665–690. https://doi.org/10.1016/j.jmps.2011.12.010

Kachanov, L.M., 1958. On the Time to Rupture under Creep Conditions. Izv. Acad. Nauk SSSR, OTN 8, 26–31.

Kalthoff, J.F., Winkler, S., 1987. Failure mode transition at high rates of shear loading., in:

Chiem, C.Y., Kunze, H.-D., Meyer, L.W. (Eds.), Impact Loading and Dynamic Behaviour of Materials. pp. 185–195.

Kulkarni, M., Belytschko, T., Bayliss, A., 1995. Stability and error analysis for time integrators applied to strain-softening materials. Comput. Methods Appl. Mech. Eng. 124, 335–363. https://doi.org/https://doi.org/10.1016/0045-7825(95)00786-Z

Landau, P., Osovski, S., Venkert, A., Gärtnerová, V., Rittel, D., 2016. The genesis of adiabatic shear bands. Nature, Sci. Reports 6: 37266. https://doi.org/10.1038/srep37226

Lee, D.-G., Lee, Y.H., Lee, S., Lee, C.S., Hur, S.-M., 2004. Dynamic deformation behavior and ballistic impact properties of Ti6Al4V alloy having equiaxed and bimodal microstructures. Met. Mater. Trans. A 35 A, 3103–3112.

Leech, P.W., 1985. Observations of Adiabatic Shear Band Formation in 7039 Aluminum Alloy. October 16A, 1900–1903. https://doi.org/10.1007/BF02670378

Lemaitre, J., 1985. A Continuous Damage Mechanics Model for Ductile Fracture. J. Eng. Mater. Technol. 107, 83–89.

Li, G.A., Zhen, L., Lin, C., Gao, R.S., Tan, X., Xu, C.Y., 2005. Deformation localization and recrystallization in TC4 alloy under impact condition. Mater. Sci. Eng. A 395, 98–101. https://doi.org/10.1016/j.msea.2004.12.020

Li, T., Fan, D., Lu, L., Huang, J.Y., E, J.C., Zhao, F., Qi, M.L., Sun, T., Fezzaa, K., Xiao, X.H., Zhou, X.M., Suo, T., Chen, W., Li, Y.L., Zhu, M.H., Luo, S.N., 2015. Dynamic fracture of C/SiC composites under high strain-rate loading: Microstructures and mechanisms. Carbon N. Y. 91, 468–478. https://doi.org/10.1016/j.carbon.2015.05.015

Liu, J., Shukui, L., Xiaoqing, Z., Zhaohui, Z., Haiyun, Z., Yingchun, W., 2008. Adiabatic shear banding in a tungsten heavy alloy processed by hot-hydrostatic extrusion and hot torsion. Scr. Mater. 59, 1271–1274. https://doi.org/10.1016/j.scriptamat.2008.08.036

Liu, X., Tan, C., Zhang, J., Hu, Y., Ma, H., Wang, F., Cai, H., 2009. Influence of microstructure and strain rate on adiabatic shearing behavior in Ti-6Al-4V alloys. Mater. Sci. Eng. A 501, 30–36. https://doi.org/10.1016/j.msea.2008.09.076

Longère, P., 2018. Adiabatic shear banding assisted dynamic failure: Some modeling issues. Mech. Mater. 116, 49–66. https://doi.org/10.1016/j.mechmat.2017.03.021

Longère, P., 2018. Respective/combined roles of thermal softening and dynamic recrystallization in adiabatic shear banding initiation. Mech. Mater. 117, 81–90. https://doi.org/10.1016/j.mechmat.2017.10.003

Longère, P., Some issues related to the modeling of dynamic shear localization- assisted failure, in: Cazacu, O., Buzuard, E. (Eds.), Dynamic Damage and Fragmentation. ISTE-WILEY, to be published.

Longère, P., Bhogaraju, S., Craciun, D., 2015. Void collapse/growth in solid materials under overall shear loading. Mech. Res. Commun. 69, 1–7. https://doi.org/10.1016/j.mechrescom.2015.05.009

Longere, P., Dragon, A., 2016. Enlarged finite strain modelling incorporating adiabatic shear banding and post-localization microvoiding as shear failure mechanisms. Int. J. Damage Mech. 1–28. https://doi.org/10.1177/1056789516645644

Longère, P., Dragon, A., 2015. Dynamic vs . quasi-static shear failure of high strength metallic alloys : Experimental issues. Mech. Mater. 80, 203–218. https://doi.org/10.1016/j.mechmat.2014.05.001

Longère, P., Dragon, A., 2009. Inelastic heat fraction evaluation for engineering problems involving dynamic plastic localization phenomena. J. Mech. Mater. Struct. 4, 319–349.

Longère, P., Dragon, A., 2008a. Evaluation of the inelastic heat fraction in the context of microstructure-supported dynamic plasticity modelling. Int. J. Impact Eng. 35, 992–999. https://doi.org/10.1016/j.ijimpeng.2007.06.006

Longère, P., Dragon, A., 2008b. Plastic work induced heating evaluation under dynamic conditions: Critical assessment. Mech. Res. Commun. 35, 135–141. https://doi.org/10.1016/j.mechrescom.2007.11.001

Longère, P., Dragon, A., 2007. Adiabatic Heat Evaluation For Dynamic Plastic Localization. J. Theor. Appl. Mech. 45, 203–223.

Longère, P., Dragon, A., Deprince, X., 2009. Numerical Study of Impact Penetration Shearing Employing Finite Strain Viscoplasticity Model Incorporating Adiabatic Shear Banding. ASME, J. Eng. Mater. Technol. 131, 011105.1-011105.14. https://doi.org/dx.doi.org/10.1115/1.3030880

Longère, P., Dragon, A., Trumel, H., De Resseguier, T., Deprince, X., Petitpas, E., 2003. Modelling adiabatic shear banding via damage mechanics approach. Arch. Mech. 55, 3–38.

Longère, P., Dragon, A., Trumel, H., Deprince, X., 2005. Adiabatic shear banding-induced degradation in a thermo-elastic / viscoplastic material under dynamic loading. Int. J. Impact Eng. 32, 285–320. https://doi.org/10.1016/j.ijimpeng.2005.03.002

Longere, P., Geffroy, A.G., Leble, B., Dragon, A., 2012. Modeling the Transition between Dense Metal and Damaged (Microporous) Metal Viscoplasticity. Int. J. Damage Mech.

21, 1020–1063. https://doi.org/10.1177/1056789511427472

Magness Jr., L.S., 1994. High strain rate deformation behaviors of kinetic energy penetrator materials during ballistic impact. Mech. Mater. 17, 147–156.

Marchand, A., Duffy, J., 1988. An experimental study of the formation process of adiabatic shear bands in a structural steel. J. Mech. Phys. Solids 36, 251–283.

Mason, J.J., Rosakis, A.J., Ravichandran, G., 1994. On the strain and strain rate dependence of the fraction of plastic work converted to heat: an experimental study using high speed infrared detectors and the Kolsky bar. Mech. Mater. 17, 135–145.

Mazeau, C., Beylat, L., Longere, P., Louvigne, P.F., 1997. On the quantitative evaluation of adiabatic shear banding sensitivity of various titanium alloys. J. Phys. IV JP 07 (C3), C3-429-C3-434. https://doi.org/10.1051/jp4:1997374

McVeigh, C., Vernerey, F., Liu, W.K., Moran, B., Olson, G., 2007. An interactive micro-void shear localization mechanism in high strength steels. J. Mech. Phys. Solids 55, 225–244. https://doi.org/10.1016/j.jmps.2006.08.002

Meyers, M., Nesterenko, V., LaSalvia, J., Xue, Q., 2001. Shear localization in dynamic deformation of materials: microstructural evolution and self-organization. Mater. Sci. Eng. A 317, 204–225.

Miguélez, M.H., Soldani, X., Molinari, A., 2013. Analysis of adiabatic shear banding in orthogonal cutting of Ti alloy. Int. J. Mech. Sci. 75, 212–222. https://doi.org/10.1016/j.ijmecsci.2013.06.011

Mohamed, G., Bacroix, B., 2000. Role of Stored Energy in Static Recrystallization of Cold Rolled Copper Single and Multicrystals 48, 3295–3302. https://doi.org/doi.org/10.1016/S1359-6454(00)00155-5

Molinari, A., 1985. Instabilité thermoviscoplastique en cisaillement simple. J. mécanique théorique appliquée 4, 659–684.

Molinari, A., Musquar, C., Sutter, G., 2002. Adiabatic shear banding in high speed machining of Ti – 6Al – 4V : experiments and modeling. Int. J. Plast. 18, 443–459.

Molinari, A., Soldani, X., Miguélez, M.H., 2013. Adiabatic shear banding and scaling laws in chip formation with application to cutting of Ti-6Al-4V. J. Mech. Phys. Solids 61. https://doi.org/10.1016/j.jmps.2013.05.006

Mourad, H.M., Bronkhorst, C.A., Livescu, V., Plohr, J.N., Cerreta, E.K., 2017. Modeling and simulation framework for dynamic strain localization in elasto-viscoplastic metallic materials subject to large deformations. Int. J. Plast. 88, 1–26. https://doi.org/10.1016/j.ijplas.2016.09.009

Needleman, A., Tvergaard, V., 1995. Analysis of a brittle-ductile transition under dynamic shear loading. Int. J. Solids Struct. 32, 2571–2590. https://doi.org/10.1016/0020-7683(94)00283-3

Odeshi, A.G., Al-ameeri, S., Mirfakhraei, S., Yazdani, F., Bassim, M.N., 2006. Deformation and failure mechanism in AISI 4340 steel under ballistic impact. Theor. Appl. Fract. Mech. 45, 18–24. https://doi.org/10.1016/j.tafmec.2005.11.005

Osovski, S., Rittel, D., Venkert, A., 2013. The respective influence of microstructural and thermal softening on adiabatic shear localization. Mech. Mater. 56, 11–22. https://doi.org/10.1016/j.mechmat.2012.09.008

Oussouaddi, O., Klepaczko, J.R., 1991. Analyse de la transition entre des déformations isothermes et adiabatiques dans le cas de la torsion d'un tube. J. Phys. IV Colloq. 01, C3-323-C3-330.

Peirs, J., Tirry, W., Amin-Ahmadi, B., Coghe, F., Verleysen, P., Rabet, L., Schryvers, D., Degrieck, J., 2013. Microstructure of adiabatic shear bands in Ti6Al4V. Mater. Charact. https://doi.org/10.1016/j.matchar.2012.10.009

Peirs, J., Verleysen, P., Degrieck, J., Coghe, F., 2010. The use of hat-shaped specimens to study the high strain rate shear behaviour of Ti – 6Al – 4V. Int. J. Impact Eng. 37, 703–714. https://doi.org/10.1016/j.ijimpeng.2009.08.002

Rice, J.R., Tracey, D.M., 1969. On the ductile enlargement of voids in triaxial stress fields. J. Mech. Phys. Solids 17, 201–217.

Rittel, D., Landau, P., Venkert, A., 2008. Dynamic Recrystallization as a potential cause for adiabatic shear failure. Phys. Rev. Lett. 101.

Rogers, H.C., Shastry, C.V., 1981. Material Factors in Adiabatic Shearing in Steels, in: Meyers, M.A., Murr, L.E. (Eds.), Shock Waves and High-Strain -Rate Phenomena in Metals - Concepts and Applications. pp. 285–298.

Rousselier, G., 1987. Ductile fracture models and their potential in local approach of fracture. Nucl. Eng. Des. 105, 97–111.

Roux, E., Longère, P., Cherrier, O., Millot, T., Capdeville, D., Petit, J., 2015. Analysis of ASB assisted failure in a high strength steel under high loading rate. Mater. Des. 75, 149–159. https://doi.org/10.1016/j.matdes.2015.03.025

Rusinek, A., Gadaj, S.P., Nowacki, W.K., Klepaczko, J.R., 2002. Simulation of heat exchange during simple shear of sheet steel. J. Theor. Appl. Mech. 40, 317–337.

Schuster, B.E., Ligda, J.P., Pan, Z.L., Wei, Q., 2011. Nanocrystalline refractory metals for extreme condition applications. JOM 63, 27–31. https://doi.org/10.1007/s11837-

011-0202-3

Seo, S., Min, O., Yang, H., 2005. Constitutive equation for Ti – 6Al – 4V at high temperatures measured using the SHPB technique. Int. J. Impact Eng. 31, 735–754. https://doi.org/10.1016/j.ijimpeng.2004.04.010

Stainier, L., Ortiz, M., 2010. Study and validation of a variational theory of thermo-mechanical coupling in finite visco-plasticity. Int. J. Solids Struct. 47, 705–715. https://doi.org/10.1016/j.ijsolstr.2009.11.012

Su, S., Stainier, L., Mercier, S., 2014. Eergy-based variational modeling of fully formed adiabatic shear bands. Eur. J. Mech. / A Solids 47, 1–13. https://doi.org/10.1016/j.euromechsol.2014.02.010

Sutter, G., List, G., 2013. Very high speed cutting of Ti-6Al-4V titanium alloy - Change in morphology and mechanism of chip formation. Int. J. Mach. Tools Manuf. 66, 37–43. https://doi.org/10.1016/j.ijmachtools.2012.11.004

Taylor, G.I., Quinney, H., 1934. The latent energy remaining in a metal after cold working. Proc. R. Soc. London. Ser. A 143: 849, 307–326.

Teng, X., Wierzbicki, T., Couque, H., 2007. On the transition from adiabatic shear banding to fracture. Mech. Mater. 39, 107–125. https://doi.org/10.1016/j.mechmat.2006.03.001

Timothy, S.P., 1987. The structure of adiabatic shear bands in metals: A critical review. Acta Metall. 35, 301–306. https://doi.org/doi.org/10.1016/0001-6160(87)90238-0

Tungsten Alloy Military [WWW Document], n.d. URL http://directory-tungsten.blogspot.com/2012/08/tungsten-kinetic-energy-penetrator.html

Tvergaard, V., Needleman, A., 1984. Analysis of the Cup-Cone Fracture in a Round Tensile bar. Acta Metall. 32, 157–169. https://doi.org/10.1016/0001-6160(84)90213-X

Umbrello, D., 2008. Finite element simulation of conventional and high speed machining of Ti6Al4V alloy 196, 79–87. https://doi.org/10.1016/j.jmatprotec.2007.05.007

Wang, B., Li, J., Sun, J., Wang, X., Liu, Z., 2014. Shear localization and its related microstructural evolution in the ultrafine grained titanium processed by multi-axial compression. Mater. Sci. Eng. A 612, 227–235. https://doi.org/10.1016/j.msea.2014.06.042

Wolf, J., Longère, P., Cadou, J.M., Crété, J.P., 2018. Numerical modeling of strain localization in engineering ductile materials combining cohesive models and X-FEM. Int. J. Mech. Mater. Des. 14, 177–193. https://doi.org/10.1007/s10999-017-9370-9

Xing, J., Yuan, F., Wu, X., 2017. Enhanced quasi-static and dynamic shear properties by heterogeneous gradient and lamella structures in 301 stainless steels. Mater. Sci. Eng. A 680, 305–316. https://doi.org/10.1016/J.MSEA.2016.10.111

Xue, Q., Meyers, M.A., Nesterenko, V.F., 2002. Self-organization of shear bands in titanium and Ti-6Al-4V alloy. Acta Mater. 50, 575–596. https://doi.org/10.1016/S1359-6454(01)00356-1

Ye, G.G., Xue, S.F., Jiang, M.Q., Tong, X.H., Dai, L.H., 2013. Modeling periodic adiabatic shear band evolution during high speed machining Ti-6Al-4V alloy. Int. J. Plast. 40, 39–55. https://doi.org/10.1016/j.ijplas.2012.07.001

Zabler, S., Rack, A., Manke, I., Thermann, K., Tiedemann, J., Harthill, N., Riesemeier, H., 2008. High-resolution tomography of cracks, voids and micro-structure in greywacke and limestone. J. Struct. Geol. 30, 876–887. https://doi.org/10.1016/j.jsg.2008.03.002

Zener, C., Hollomon, J.H., 1944. Effect of Strain Rate Upon Plastic Flow of Steel. J. Appl. Phys. 22–32.

Zhou, M., Ravichandran, G., Rosakis, A.J., 1996a. Dynamically Propagating Shear Bands in Impact-Loaded Plates-II. Numerical Simulations. J. Mech. Phys. Solids 44.

Zhou, M., Rosakis, A.J., Ravichandran, G., 1996b. Dynamically propagating shear bands in impact-loaded prenotched plates-I. Experimental investigations of temperature signatures and propagation speed. 44, 981–1006.